2012

# Self-assembly Behaviors of Macroions in Dilute Solution

Dong Li
*Lehigh University*

# Self-assembly Behaviors of Macroions in Dilute Solution

By

Dong Li

A Dissertation

Presented to the Graduate and Research Committee

of Lehigh University

in Candidacy for the Degree of

Doctor of Philosophy

in

Chemistry

Lehigh University

September, 2012

# Certificate of Approval

Approved and recommended for acceptance as a dissertation in partial fulfillment of the requirements for the degree of Doctor of Philosophy

Name: Dong Li

Dissertation Title: Self-assembly Behaviors of Macroions in Dilute Solution

___07-24-2012_____
Defense Date

_____
Tianbo Liu

_____
Approved Date

Committee Members:

_____
Jebrell Glover

_____
Kai Landskron

_____
David Moore

_____
Daniel OuYang

# Acknowledgements

I wish to express my deep gratitude to my parents, for giving me their love, understanding, and the spirit of curiousness. Without their understanding and support, I could not come so far to achieve my dreams. Special thanks to my wife, Jie Fu, who did the editing and the proof reading work. Her love is always the source of my courage and my strength.

I would like to thank my advisor, Dr. Tianbo Liu, for his guidance and support during my Ph.D. studies. His knowledge influents the way I observe the world; his enthusiasm for science and his support encourage me to explore the fascinating realm of macroions; and his great personality makes the pursue of knowledge an enjoyable journey. It is my great honor to work with this man, as my mentor and my friend.

I would like to thank my committee, Dr. Jebrell Glover, Dr. Kai Landskron, Dr. David Moore, and Dr. Daniel OuYang, for your guidance, patience, and valuable advice. Your help, from different perspectives, has opened my mind and expanded my vision. I must also acknowledge Dr. James Roberts and Dr. Norm Zheng for their guidance in NMR studies. I really appreciate the help from Monica Reith, who did the DNA insertion and quantification for us. Dr. Tao Li and Dr. Soenke Seifert from Argonne National Laboratory gave us enormous help during our visit to APS.

For all my friends at Lehigh, please accept my appreciation. Especially, to my colleagues: Dr. Jie Zhang, Dr. Padmaja P. Mishra, Dr. Celine Pichon, Dr. Joe Pigga, Dr. Mauricio F. Misdrahi, Dr. Melissa L. Kistler, Panchao Yin, Fadi Haso, Jill Sledziewski, Baofang Zhang, Jinwoo Lee, Kyle Roots, and my undergraduate students.

# Table of Contents

# List of Tables

# List of Figures

# Abstract

Macroions (2 - 10 nm in size) behave quite differently from simple ionic salts or colloidal systems in solution. In this size range and with moderate charge, they tend to slowly self-assemble into a single-layered, spherical, hollow, “blackberry” type structure. Both macroanions and macrocations form the similar blackberry structures which indicate it is a universal phenomenon. The driving forces for the blackberry structure formation are believed to be the counterion mediated attraction and hydrogen bonding, but not through chemical bonds or van der Waals attractions. Interestingly, counterion mediated attraction has been proposed and tested in biological systems with limited examples. The current research on the counterion distribution of Hepatitis B viral capsids has shown the importance of charge effect during their self-assembly process. Furthermore, by functionalizing giant inorganic polyoxometalate macroions with organic groups, a new family of hybrid surfactants are achieved which provide great potentials toward developing new materials for catalysis, polymerization, drug delivery, and medicines.

# Chapter 1: Introduction to Macroions

## 1.1 Introduction

The solution behaviors of polyelectrolyte are complicated. The primary reason is the long range Coulomb interaction between charged particles. Historically, the most famous method to describe a simple diluted ionic solution is Debye-Hückel theory which was first formulated by Peter Debye and Erich Hückel in 1923.[1] However, in general, the Debye-Hückel theory is only valid for very diluted ionic solutions in which ions can be treated as point-like charges. On the other hand, charged colloids with size dimension ranging from ~ 100 nm to several microns are fundamentally different from simple ions. To explain and interpret solution behaviors of these large charged colloidal particles, a theoretical framework of Derjaguin-Landau-Verwey-Overbeek (DLVO) theory developed in the 1940s is widely applied.[2,3] The DLVO potential consists two major parts, one is the attractive van der Waals interaction and the other is the purely repulsive Coulomb interaction. Small counter-ions are believed to take a distribution of thermal equilibrium in a stationary configuration around colloidal particles. The effective interaction $U = U_R + U_A$ controls the dynamical behavior of colloidal particles. In other words, the stability of colloids in solution stems from the competition between these two interactions. Although these two theories have been successfully applied to various polyelectrolyte systems, they failed to explain or predict the solution behavior of macroions with size between 2 to 10 nm. In this range, the size disparity between macroions and counterions (~ 10 to 1) is much smaller compared with that of colloids and counterions (~ 1000 to 1); at the same time, the macroions are large enough that they

could not be treated as point-like charges. Therefore, it is interesting and important to study macroions within this size range.

## 1.2 Polyoxometalates type macro-anions and functionalized hybrid POMs

### 1.2.1 Polyoxometalates (POMs)

Polyoxometalates (POMs) represent a large group of structurally well-defined, giant macro-anions assembled from multiple transition metal oxides, which are linked through shared oxygen atoms.[4] Owing to the tunable valence and coordination geometry of the central metal ions, various POMs with different sizes, shapes and charges have been synthesized. The field of polyoxometalates has been rapidly expanding from isopolyoxometalates to heteropolyoxometalates, from early transition metal POMs (Mo, V, Cr, Fe, W, Mn, etc.) to late transition metal POMs (U, Nb, Au, Pd, etc.), and from pure inorganic molecular clusters to hybrid clusters.[5-7] Fig. 1.1 gives several examples of well-characterized POM molecular clusters. Most of the POMs are negatively charged because of their oxo ligands. The surface charge density of POMs can be readily tuned by substituting the central transition metals, changing the oxidation state of the metal ions, or simply changing the solution pH. Because of their rigid molecular structure and well-defined geometry, POMs are perfect model systems to study the solution behaviors of polyelectrolytes. The detailed solution study of POMs type macro-anions will be covered in Chapter 2.

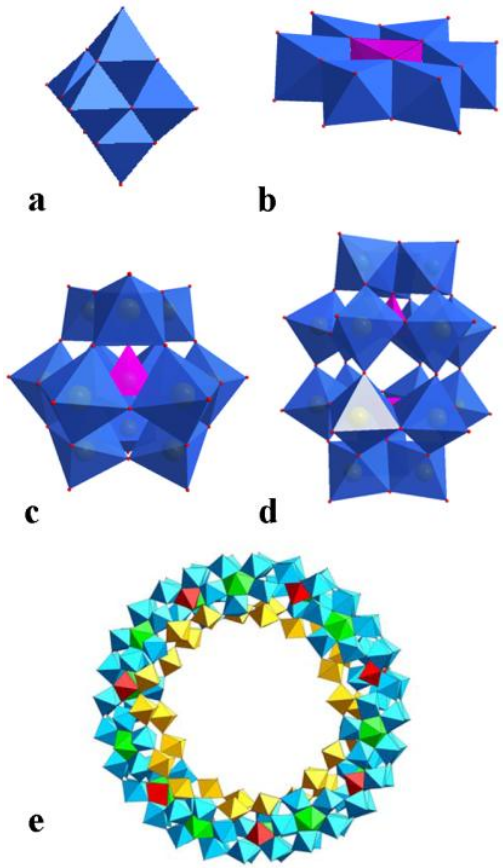


**Figure 1.1** Several well-characterized polyoxometalate clusters (a) Lindqvist; (b) Anderson; (c) Keggin; (d) Dawson; and (e) $\{Mo_{154}\}$.

### 1.2.2 Inorganic-organic hybrid POMs

The POM family can be further extended by grafting organic functional motifs onto purely inorganic POM clusters to create a novel group of hybrid macroions. Such inorganic-organic molecular hybrids are expected to render amphiphilic properties to the POMs and consequently improve their applications by expanding their compatibility in organic media. Furthermore, these organic ligands can also be applied to adjust some important features of POMs, including electronic and luminescent properties.[8] Exploring

the amphiphilic nature of such hybrids and understanding their self-assembly behavior in solution and at interface would be important initial steps for scientists. The majority of inorganic-organic hybrid POMs can be classified into two groups, the hybrids with weak interactions (e.g. electrostatic interactions, hydrogen bonding, or van der Waals interactions etc.) and the hybrids with strong interactions (e.g. covalent bonds) between the inorganic and organic components. The study of their unique solution behaviors will be discussed in Chapter 4.

## 1.3 Nanocage type macro-cations

Transition metal mediated organic-inorganic supramolecular nanostructures have drawn great attention ever since the last two decades. These novel macromolecules are self-assembled from small organic ligands and metal ions. Their shape, size, charge, and composition can be rationally designed by choice of the transition metals and the organic ligands.[9] The successful self-assembly process takes advantage of the coordination bonds formed between metal centers and organic ligands. Unlike natural bio-macromolecules (DNA, RNA and proteins) or most organic compounds, these coordination bonds are of intermediate strength compared to the weak interactions (hydrogen bonding, van der Waals forces and electrostatic interactions) and the strong covalent carbon-carbon bonds. By carefully choosing reaction conditions, one can select either a thermodynamic or kinetic product. Moreover, owing to the kinetic liability of the heteroatom-metal bonds, defect structures can often be healed through the self-assembly process.

According to Stang and co-workers, two design principles of metal mediated organic-inorganic macromolecules have been developed: The 'symmetry interaction model'[10,11]

and the 'molecular library model'[12]. Using these models in principle the preparation of cages of any symmetry and size is possible.

Among various defined structures (bowls, boxes, tubes, and spheres), three dimensional nanocages and polyhedral are particularly interesting because of their highly symmetric structure, large central void and the ability of encapsulating guest molecules.

### 1.3.1 Self-assembled prisms and cylinders.

#### Triangular prisms.

In 1995, Fujita *et al.* reported a one-port direct synthesis procedure for constructing a triangular nanoprism, which is the simplest and smallest three-dimensional complex in the nanocage family.[13] Specifically, a tridentate ligand 1, 3, 5-tris(4-pyridylmethyl)-benzene (**B1**) was reacted with ethylenediamine palladium dinitrate (**A1**) in the presence of a guest molecule of sodium 4-methoxyphenylacetate at room temperature in water. The three-dimensional, prism-like complex (**C1**) was formed exclusively as the thermodynamically stable product, as shown in Fig. 1.2.

#### Cylindrical complex.

A more complicated multi-component nanocylinder complex was synthesized by Lehn and coworkers (Fig. 1.2). By slowly adding a solution of $[Cu(CH_3CN)_4]BF_4$ (**B2**) to a 2:3 mixture of hexaphenylhexaazatriphenylene (**A2**) and the tetraphridine (**C2**), the cylindrical complex (**D2**) as a dark-purple, air-stable solid was assembled after 20 h.[14]

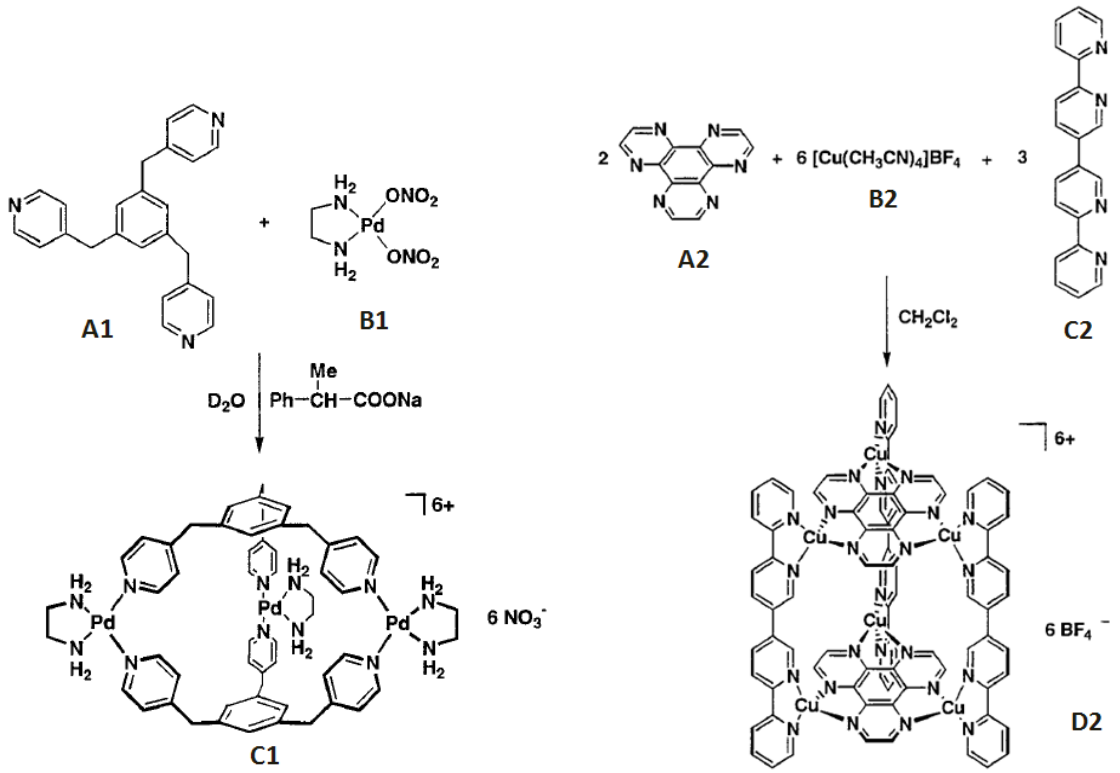


**Figure 1.2** The self-assembly processes of one nano-sized trianglar priasm and one nano-sized cylindrical complex. (Copyright: American Chemical Sociaty 2000)

### 1.3.2 Self-assembled truncated tetrahedra (Octahedra).

The nanosized octahedral 3D cage was first constructed by Fujita's group through the metal-directed self-assembly. Specifically, ethylenediamine Pd (II) dinitrate and the tritopic aromatic ligands were employed as building blocks, and under mild reaction conditions, those starting molecules were self-assembled into a highly symmetric $M_6L_4$ type adamantanoid structure in a quantitative yield. The final cage structure has remarkable thermodynamic stability. Even if the starting stoichiometry of Pd dinitrate

and aromatic ligands was not in the correct 3:2, the final cage with a 3:2 ratio was still formed quantitatively and excess starting molecules remained unreacted. [15]

Although structurally quite similar to complex **C6**, the Pt complex **D7** is formed only under harsh conditions with the help of a templating guest.[16] The synthesis reaction was carried out by mixing the platinum dinitrate, **A6**, and the organic linker **B7** in boiling water in the presence of sodium adamantyl carboxylate **C7**. After 24 h stirring, a high-yield formation of **D7** was achieved. Once formed, the cage compound **D7** demonstrates remarkable kinetic stability as the result of the stronger Pt-pyridine bond. In contrast to the palladium analogous **C6**, this Pt induced complex is stable under highly acidic and basic conditions (it can survive from pH 1 to pH 11). Consequently, a pH-responsive molecular capture-release system can be realized based upon the cage **D7**. For instance, 4 small guest molecules (N,N-dimethylaniline) can be encapsulated in the hydrophobic cavity in a 1:4 (host: guest) mode under basic conditions, whereas under acidic conditions, the guest molecules are instantly released due to the decreased hydrophobic interaction as well as the cationic repulsion between the cage and the protonated N,N-dimethylaniline.

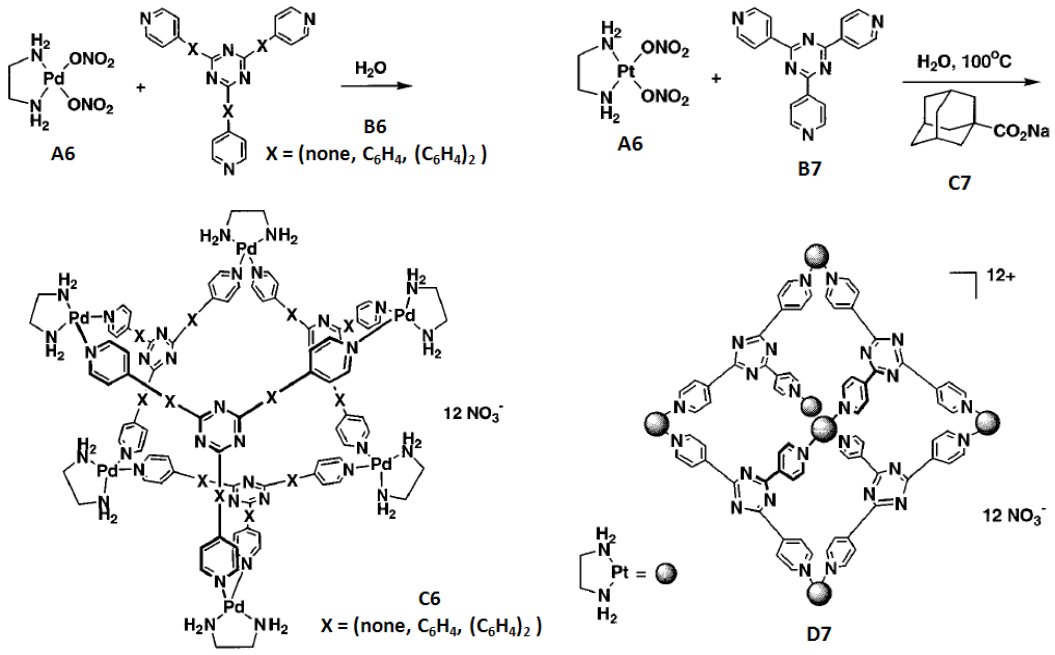


**Figure 1.3** The self-assembly processes of two turncated nano-sized tetrahedra. (Copyright: American Chemical Sociaty 2000)

### 1.3.3 Self-assembled truncated cuboctahedra.

Although in nature highly symmetrical structures have been observed, like the protein shell structure of human Rhinovirus, the similar artificial structures are difficult to make by ordinary organic synthesis. However, recently, Stang and coworkers have demonstrated the one-step construction of a cuboctahedral supramolecular structure via coordination-driven self-assembly.[17] Specifically, by combining 8 equivalent planar tritopic ligands (platinum tris(triflate), **A8**) and 12 equivalent ditopic angular subunits (bispyridyl acetal **B8**) together in the solvent of dichloromethane, a single highly symmetrical complex **C8** was quantitatively formed. The formation of a second cuboctahedron (**C9**) was also achieved by using different building blocks (**A9, B9**),

which in turn, reveals the facility of the method of coordination-driven self-assembly to construct highly symmetric supramolecular structures. The solution behaviors of two nanocages are summarized in Chapter 3.

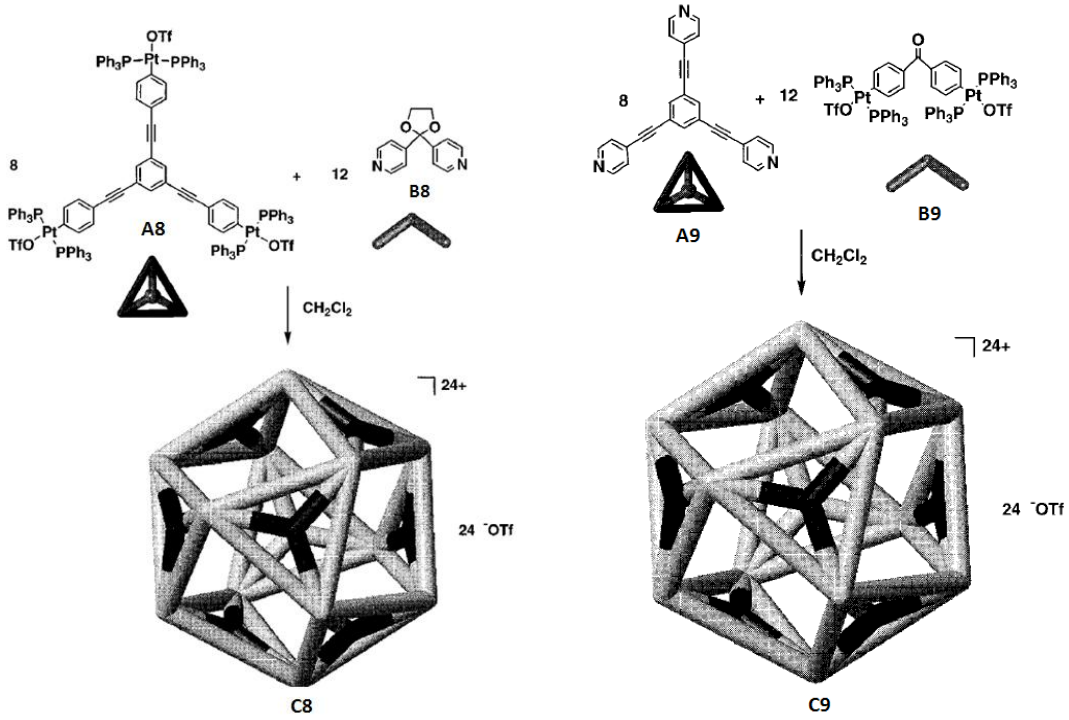


**Figure 1.4** The self-assembly processes of two turncated nano-sized cuboctahedra. (Copyright: American Chemical Sociaty 2000)

## 1.4 Introduction to bio-macroions

Highly charged bio-macromolecules with size in nanometer scale can also be treated as macroions, for instance, DNA, RNA, F-actin, and microtubules. In these bio-macroionic systems, electrostatic interactions are fundamental to various phenomena, especially in regulating nucleic acids (DNA and RNA) condensation and folding, maintaining protein ternary structure and directing the assembly of viral capsids. For example, recent studies

of one short DNA (25 base pairs, about 8 nm) in solution have shown a short ranged attraction between like-charged DNAs, and the magnitude is quite sensitive to the valence and the concentration of small counterions. In this case, DLVO theory fails to predict the biologically important attraction of like-charged bio-macroions. Counterion condensation around DNA macroions is not the only example that demonstrates the complex nature of electrostatic interactions in biological systems. Viral capsids formation, an important however, poorly understood process in the life cycle of viruses, deserves a closer look. Counterion mediated attraction during the viral capsids formation will be discussed in Chapter 6.

## References:


(1) Debye, P. J.; Hückel, E. *Phys. Z.* **1923**, *24*, 185.

(2) Derjaguin, B. V.; Landau, L. *Acta Physicochim* **1941**, *89*, 555.

(3) Verwey, E. J.; Overbeek, J. T. G. *Theory of the Stability of Lyophobic Colloids*; Elsevier: Amsterdam, 1948.

(4) In *Chem. Rev.*; Hill, C. L., Ed. 1998; Vol. 98.

(5) Long, D. L.; Burkholder, E.; Cronin, L. *Chem. Soc. Rev.* **2007**, *36*, 105.

(6) Long, D.-L.; Tsunashima, R.; Cronin, L. *Angew. Chem. Int. Ed.* **2010**, *49*, 1736.

(7) Dolbecq, A.; Dumas, E.; Mayer, C. d. R.; Mialane, P. *Chem. Rev.* **2010**, *110*, 6009.

(8) Yamase, T. *Mol. Eng.* **1993**, *3*, 241.

(9) Stang, P. J.; Olenyuk, B. *Accounts of Chemical Research* **1997**, *30*, 502.

(10) Caulder, D. L.; Raymond, K. N. *J. Chem. Soc., Dalton Trans.* **1999**, 1185.

(11) Baxter, P. N. W.; Lehn, J. M.; Kneisel, B. O.; Baum, G.; Fenske, D. *Chem. Eur. J* **1999**, *5*, 113.

(12) Fujita, M. *Chem. Soc. Rev.* **1998**, *27*, 417.

(13) Fujita, M.; Nagao, S.; Ogura, K. *J. Am. Chem. Soc.* **1995**, *117*, 1649.

(14) Baxter, P.; Lehn, J.-M.; DeCian, A.; Fischer, J. *Angew. Chem. Int. Ed.* **1993**, *32*, 69.

(15) Fujita, M.; Oguro, D.; Miyazawa, M.; Oka, H.; Yamaguchi, K.; Ogura, K. *Nature* **1995**, *378*, 469.

(16) Ibukuro, F.; Kusukawa, T.; Fujita, M. *J. Am. Chem. Soc.* **1998**, *120*, 8561.

(17) Olenyuk, B.; Whiteford, J. A.; Fechtenkötter, A.; Stang, P. J. *Nature* **1999**, *398*, 796.

# Chapter 2: Solution Behaviors of POM Type Macro-anions: Theories and Experimental Observations

## 2.1 Introduction

POM type macro-anions with size between 2 to 6 nm demonstrated quite unique solution behaviors: Instead of distributing in aqueous solutions to form stable, homogeneous real solutions, those fully hydrophilic clusters slowly self-assemble into spherical, hollow, single-layered vesicular structures, which are named as "blackberry" type structures. It seems quite contradictive to the common sense that macroions with the same type of charge should repel each other. In order to understand this unique phenomenon, it is necessary to exam two classic theories that commonly used to describe polyelectrolyte solutions.

## 2.2 Derivation of the Debye-Hückel's limiting theory

The fundamental and central idea of the D-H theory is the concept of ionic atmosphere. It states that because there is an electrostatic attraction between opposite charged ions and an electrostatic repulsion between the same charged ions, for any given ion in the solution, there is an excess of its counter ions, and those counter ions have a net opposite charge equal to that on the central ion. This time-averaged, spherical cloud is called the ionic atmosphere, as illustrated in Fig. 2.1. Since the electrostatic interactions between ions are responsible for the non-ideal behaviors of an electrolyte solution, we can express the chemical potential of an $i^{th}$ ion as

$$\mu_i = \mu_i^{\text{ideal}} + \Delta\mu_i^{el} \tag{1}$$

For an ideal solution

$$\mu_i^{\text{ideal}} = \mu_i^{\circ} + RTlnx_i \tag{2}$$

For an electrolyte solution

$$\mu_i = \mu_i^{\circ} + RTlnx_i + RTln\gamma_i \tag{3}$$

where $\gamma_i$ is the activity coefficient of the $i^{\text{th}}$ ion. Compare equation 1 to 3, it is clear that the contribution from electrostatic interaction is

$$\Delta\mu_i^{el} = RTln\gamma_i \tag{4}$$

So now the problem becomes how we can calculate $\gamma_i$.

Assume that in the electrolyte solution there is 1, 2 … *i* kinds of ions with bulk concentration being $n_1$, $n_2$ … $n_i$ per unit volume and their charge number is $z_1e$, $z_2e$ … $z_ie$ (z is the valence and e is the unit charge). If we choose one cation as our target (as shown in Fig. 2.1), then in a small volume *dV* which is separated from the central cation by a distance *r*, the local concentration for the $i^{\text{th}}$ ion $n_i'$ can be written as

$$n_i' = n_i \exp\left(-\frac{z_i e\varphi}{kT}\right) \tag{5}$$

according to the Boltzmann distribution equation, in which $\varphi$ is the central cation mean electrical potential averaged by time, and *k* is the Boltzmann constant. Since the mean charge density $\rho$ in *dV* is actually a sum of charge density all ions $\Sigma\, n_i' z_i e$, we have

$$\rho = \sum_i n_i e z_i exp\left(-\frac{z_i e\varphi}{kT}\right) \tag{6}$$

Also, according to Poisson's equation,

$$\nabla^2\varphi = -\frac{\rho}{\varepsilon} \tag{7}$$

Where $\nabla^2 = (\frac{\partial^2}{\partial x^2} + \frac{\partial^2}{\partial y^2} + \frac{\partial^2}{\partial z^2})$ and $\varepsilon$ is the dielectric constant of the solution. Since the solution is homogeneous and isotropic at thermal equilibrium, the counter-ion distribution in the ionic atmosphere is highly symmetric; a simpler form of this equation can be derived

$$\frac{1}{r}\frac{d^2(r\varphi)}{dr^2} = -\frac{\rho}{\varepsilon} \tag{8}$$

Combine equation 6 and 8,

$$\frac{1}{r}\frac{d^2(r\varphi)}{dr^2} = -\frac{1}{\varepsilon}\sum_i n_i e z_i exp\left(-\frac{z_i e\varphi}{kT}\right) \tag{9}$$

This equation does not have an explicit general solution because there is a fundamental inconsistency and it can be solved only for certain limiting cases. Therefore, if we assume that this electrolyte solution is so dilute that the electrostatic energy between ions is much smaller that the thermal energy, $z_i e\varphi << kT$, equation 6 can be simplified as

$$\rho = -\sum_i \frac{n_i z_i^2 \mathrm{e}^2}{kT}\varphi \tag{10}$$

And now equation 9 becomes

$$\frac{1}{r}\frac{d^2(r\varphi)}{dr^2} = \frac{e^2}{\varepsilon kT}\sum_i n_i z_i^2\,\varphi \tag{11}$$

If we define

$$r_d^2 = \frac{e^2}{\varepsilon kT}\sum_i n_i z_i^2 \tag{12}$$

Then equation 11 becomes

$$\frac{1}{r}\frac{d^2(r\varphi)}{dr^2} = r_d^2\varphi \tag{13}$$

where $r_d^{-1}$ is called the Debye length. By applying two boundary conditions: a) when $r \rightarrow \infty$, $\varphi \rightarrow 0$, and b) $r \rightarrow 0$, $\varphi \rightarrow \varphi_0$ when no counter-ions present around the central ion; we can solve this Poisson-Boltzmann equation as

$$\varphi = \frac{z_i e}{4\pi\varepsilon r} \mathrm{e}^{(-r_d r)} \tag{14}$$

This electrostatic potential also can be viewed as a sum of two potentials: one is introduced by the central ion alone and the other is generated by its ionic atmosphere, as shown below

$$\varphi = \frac{z_i e}{4\pi\varepsilon r} - \frac{z_i e r_d}{4\pi\varepsilon} \tag{15}$$

In which we applied the assumption that for extremely diluted solution $r_d$ is very small, thus $\mathrm{e}^{(-r_d r)}$ becomes $(1 - r_d r)$. By using the charge-up strategy, the total work of charging the $i^{\text{th}}$ ion can be calculated as

$$w_i = \frac{z_i^2 e^2}{8\pi\varepsilon r} - \frac{z_i^2 e^2 r_d}{12\pi\varepsilon} \tag{16}$$

If the total number of the $i^{\text{th}}$ ion is $N_i$, then the total work of charging all ions is

$$w_A = \sum_i \frac{N_i z_i^2 e^2}{8\pi\varepsilon r} - \sum_i \frac{N_i z_i^2 e^2 r_d}{12\pi\varepsilon} \tag{17}$$

When the solute is extremely diluted, $r_d \rightarrow 0$, the solution can be treated as ideal, then

$$w_0 = \sum_i \frac{N_i z_i^2 e^2}{8\pi\varepsilon r}$$

Therefore, in an electrolyte solution, the work done by the electrostatic interactions between ions is equal to

$$w_{el} = w_A - w_0 = \Delta G_{el} = -\sum_i \frac{N_i z_i^2 e^2 r_d}{12\pi\varepsilon} \tag{18}$$

where $\Delta G_{el}$ is the Gibbs free energy change raised by the electrostatic interactions. Since

$$\Delta\mu_i^{el} = \frac{\partial \Delta G_{el}}{\partial N_i} = RTln\gamma_i$$

We have

$$ln\gamma_i = -\frac{z_i^2 e^2 N_A}{8\pi\varepsilon RT}\left(\frac{2e^2 N_A \rho_{slu}}{\varepsilon kT}\right)^{1/2}\sqrt{I} \tag{19}$$

or

$$ln\gamma_i = -Az_i^2\sqrt{I} \tag{20}$$

where $I$ is the ionic strength of the solution. From the derivation of the D-H theory we can notice that several important assumptions are used and we should keep in mind that without these limiting conditions, the D-H theory will not hold.

1. The ion distribution follows the Boltzmann distribution form and Poisson equation holds.

2. Ions are point-like charges with no polarizability.

3. The Coulomb interaction is the only interaction that dominants the ion behaviors. The attraction between ions is relatively small, which is lower than 1 $k_B T$.

4. The solvent is treated as a continuous dielectric medium.

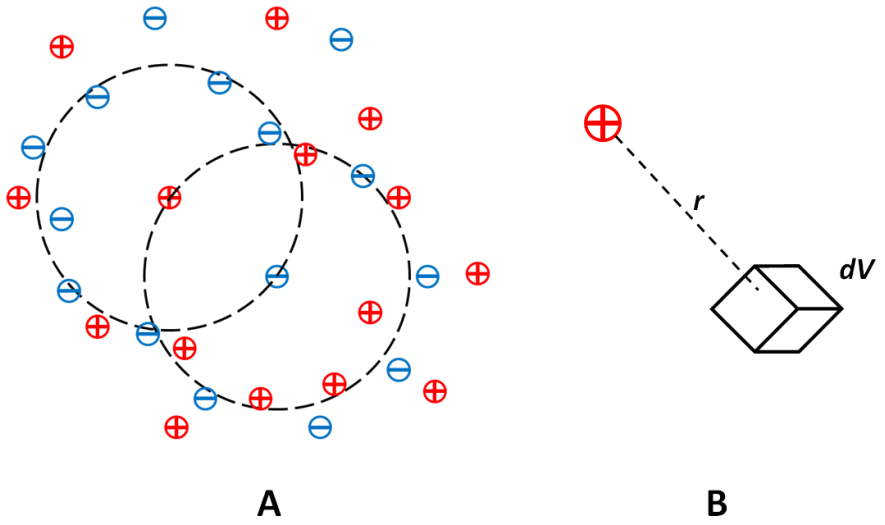


**Figure 2.1** Illustration of (A) the ionic atmosphere and (B) electrostatic interactions between a central cation and its counterions in the volume of *dV*.

## 2.3 General features of the DLVO theory[1]

Colloids are heterogeneous and thermodynamically unstable systems compared to simple ionic solutions. The colloidal particle (diameter larger than 100 nm) has a well defined surface and volume. Common methods to increase the system stability are either modifying the surface to include stereo interaction or modifying the surface to have charge. There are two possible ways to charge up colloidal particles. An initially uncharged surface may preferentially adsorb ions from the solution. The other way is the ionization of functional groups on the colloid's surface. Counterions tend to accumulate close to the surface of colloids to form an electrical double layer. To describe the electrical potential of this double layer, Helmholtz first came up with a capacitor model, which simplify the situation of the interface of charged colloidal particle surface and the

accumulated counterions in solvent as a parallel plate capacitor. These two charged surfaces are separated by a dielectric solvent medium. The potential difference between these two plates is $\Delta\varphi$, which decays in a linear fashion inside the double layer. This model is oversimplified in a sense that it totally ignored the thermal motion of the small counterions which tends to diffuse in solution. Gouy (1910) and Chapman (1913) improved this parallel capacitor model by replacing the static counterion layer into a diffuse layer. This diffuse layer contains two parts: one part is closely associated with the colloidal particle's surface while the other part is loosely interact with the colloidal particle's surface and graduate diffuse into the bulk solutions. In this case, the counter-ion distribution can be described by Boltzmann distribution. Recall that in D-H theory the ionic atmosphere around a central ion is also in Boltzmann distribution, therefore, the approximation that applied in D-H theory to describe the electrical potential of a point charge may also be applied here. The only difference is that in the colloidal systems, the size of the colloidal particles needs to be taken into consideration since they are no longer point-like charges. By solving the linearized Poisson-Boltzmann equation for spherical electrical double layer under the D-H approximation, the mean electrical potential can be written as

$$\varphi = \varphi_0 \frac{R_s}{r} \mathrm{e}^{[-\kappa(r-R_s)]} \tag{21}$$

where $\kappa^{-1}$ is the Debye screening length, $r$ is the distance from the particle center to any point in the double layer and $R_s$ is the radius of the spherical particle. Since this relationship between φ and r is derived based upon the D-H approximation, equation (21) is only valid at low surface potential. The parameter $\kappa$ is similar to $r_d$ in the deviation of

the D-H theory for simple ionic solutions, and $\kappa^{-1}$ represents the thickness of the diffuse double layer.

### 2.3.1 Gouy-Chapman approximation

Consider that we have a positively charged plate immersed into a solvent with a dielectric constant of $\varepsilon$, and a diffuse layer of counter-ions is adsorbed onto the plate surface. We define the direction perpendicular to the plate as the x direction and the plate extends to infinity in the y and z directions. Now, equation (7) is written

$$\left(\frac{d\varphi^2}{dx^2}\right) = -\frac{\rho}{\varepsilon} \tag{22}$$

Combine equation (6) with (22) and multiply $2d\varphi/dx$ to both sizes, we have

$$(d\varphi/dx)^2 = \frac{2kT}{\varepsilon}\sum_i n_i \left[exp\left(-\frac{z_i e\varphi}{kT}\right) - 1\right] \tag{23}$$

If the electrolyte in solution is the symmetrical *z*:*z* type, equation (23) can be further integrated as

$$(d\varphi/dx)^2 = \frac{2kTn_\infty}{\varepsilon}\left[exp\left(-\frac{ze\varphi}{2kT}\right) - exp\left(\frac{ze\varphi}{2kT}\right)\right]^2 \tag{24}$$

Integrate equation (24) to give us the Gouy-Chapman expression for the relationship between potential $\varphi$ and distance $x$ within the double layer, which is without the D-H assumption of low surface potentials.

$$\Upsilon = \Upsilon_0 \exp(-\kappa x) \tag{25}$$

Where $\Upsilon$ is defined as

$$\Upsilon = \left[\exp\left(\frac{ze\varphi}{2kT}\right) - 1\right] / \left[\exp\left(\frac{ze\varphi}{2kT}\right) + 1\right] \tag{26}$$

In the case of large $x$ (outside the double layer), the above equation can be simplified as

$$\varphi = \left(\frac{4kT}{ze}\right)\Upsilon_0 \exp(-\kappa x) \tag{27}$$

From equation (25) and (27), we can notice that instead of $\varphi$ that varies exponentially with $x$ in the D-H theory, it is the ratio $\Upsilon$ that changes with $x$ in the Gouy-Chapman theory. However, when the surface potential is low ($z_i e\varphi << kT$), equation (25) can still return to equation (14).

### 2.3.2 Repulsion between two parallel charged plates in electrolytes

The next step in developing the DLVO theory is to consider the interactions between two parallel plates with the same charges immersed in an electrolyte, as shown in Fig. 2.2. In this case, as the distance between the two plates decreases, the potential of each of the plates starts to overlap and the counter-ion concentration in the middle of the plates starts to increase. At equilibrium, the electrostatic forces and the osmotic pressure operate on any volume element between the two plates must balance with each other. Therefore, we can write an expression for one volume element between the two plates at equilibrium as

$$F_x + F_{el} = \left(\frac{dp}{dx}\right) + \rho\left(\frac{d\varphi}{dx}\right) = 0 \tag{28}$$

Combine equation (7), we have

$$\left(\frac{dp}{dx}\right) - \frac{\varepsilon}{2}\left(\frac{d^2\varphi}{dx^2}\right)\left(\frac{d\varphi}{dx}\right) = 0 \tag{29}$$

which can be further written as

$$\left(\frac{d}{dx}\right)\left[p - \frac{\varepsilon}{2}\left(\frac{d\varphi}{dx}\right)^2\right] = 0 \tag{30}$$

This result indicates that to achieve equilibrium between osmotic pressure and electric field, it is requires that

$$\left[p - \frac{\varepsilon}{2}\left(\frac{d\varphi}{dx}\right)^2\right] = \text{const.} \tag{31}$$

Since $\varphi$ goes through a minimum at the midpoint position, where $^{d\varphi}/_{dx} = 0$ at x = $\ell/2$, the constant in equation (31) equals to the pressure at the midpoint $P_{\ell/2}$. We can rewrite equation (28) as

$$dp = -\rho d\varphi \tag{32}$$

Substituting equation (6) for $\rho$ in a z:z type electrolyte, we have

$$dp = -zen_\infty \left[exp\left(-\frac{ze\varphi}{kT}\right) - exp\left(\frac{ze\varphi}{kT}\right)\right] d\varphi \tag{33}$$

Since $e^x - e^{-x} = 2\,sinh\,x$, equation (33) can be written as

$$dp = 2zen_\infty \sinh\left(\frac{ze\varphi}{kT}\right) d\varphi \tag{34}$$

Take the limiting conditions under consideration in which $P = P_0$ at $\varphi = 0$ and $P = P_{\ell/2}$ at $\varphi = \varphi_{\ell/2}$; equation (34) is integrated as

$$F_R = P_{l/2} - P_0 = 2kTn_\infty \left[cosh\,\frac{ze\varphi_{l/2}}{kT} - 1\right] \tag{35}$$

where $F_R$ is the repulsive force acting on the unit area. When the distance $\ell$ between two plates is large, the potential at the midpoint can be written as

$$\varphi_{l/2} \approx \varphi_1 + \varphi_2 \approx 2\left(\frac{4kT}{ze}\right)\Upsilon_0 \exp(-\kappa x/2) \tag{36}$$

Equation (36) is only valid when the overlap of the double layer is small and consequently the potential is low. With these restrictions, equation (35) can be simplified into

$$F_R \approx 64kTn_\infty {\Upsilon_0}^2 exp(-l\kappa) \tag{37}$$

Since $d\Phi_R = -F_R dl$, we have

$$d\Phi_R = -64kTn_\infty \Upsilon_0^{\,2} exp(-l\kappa)dh \tag{38}$$

Integrate equation (38) with the boundary condition of $\Phi_R = 0$, when $\ell = \infty$, yielding

$$\Phi_R = 64kTn_\infty \Upsilon_0^{\,2} \kappa^{-1} exp(-l\kappa) \tag{39}$$

Equation (39) gives the general expression for the repulsive potential between two parallel plates with the same charges immersed in a dielectric medium, and is only valid when the distance between the two plates is relatively large and the electric potential is relatively low. To describe the repulsive interaction between two spherical particles, an easy way is to use the Derjaguin approximation. And the repulsive potential can be written as

$$\Phi_R = 64\pi R_s kTn_\infty \Upsilon_0^{\,2} \kappa^{-2} exp(-s\kappa) \tag{40}$$

Where $R_s$ is the radius of the two spherical particle and $s$ is the closest distance from the surface of the two spheres.

### 2.3.3 DLVO potential and the primary and secondary minima

In the DLVO theory, the only possible source of attraction between two colloidal particles is believed to be the van der Waals forces, which can be written as

$$\Phi_A = -\frac{1}{12} A \frac{R_s}{s} \tag{41}$$

For two spheres with $s$ is the closest distance from the surface of the two spheres, $R_s$ is the radius of the colloidal particles and $A$ is the *Hamaker* constant.

Now, with the knowledge of repulsive potential and attractive potential, the DLVO potential can be written as

$$\Phi_{net} = \Phi_R + \Phi_A = 64\pi R_s kTn_\infty \Upsilon_0^{\,2} \kappa^{-2} exp(-s\kappa) - \frac{1}{12} A \frac{R_s}{s} \qquad (42)$$

for two large spherical colloidal particles immersed in a dielectric medium. From equation (42), we can see that the repulsive potential $\Phi_R$ depends sensitively on the concentrations of small counter-ions and large particles through κ, however, for the attractive potential $\Phi_A$, it is nearly insensible to the change of salt concentrations. Therefore, it gives us a great opportunity to study the solution behaviors of colloidal particles simply by varying the salt concentration, *e.g.* ionic strength.

As shown in Fig. 2.3, we can plot the DLVO potential $\Phi_{net}$ versus the distance between two particles. And we notice that when the repulsive potential energy barrier becomes lower than the thermal energy of $k_B$T under high salt concentration, the colloidal particles fall into the primary minimum because of the strong van der Waals' attraction. This is an irreversible process called coagulation. However, under certain circumstances the superposition of $\Phi_R$ and $\Phi_A$ may produce a relatively shallow minimum called the secondary minimum. The depth of the secondary minimum is quit sensitive to the salt concentration and if it is larger than the thermal energy $k_B$T, the colloidal particles tend to flocculate and form colloidal crystallites. This flocculation is a reversible process.

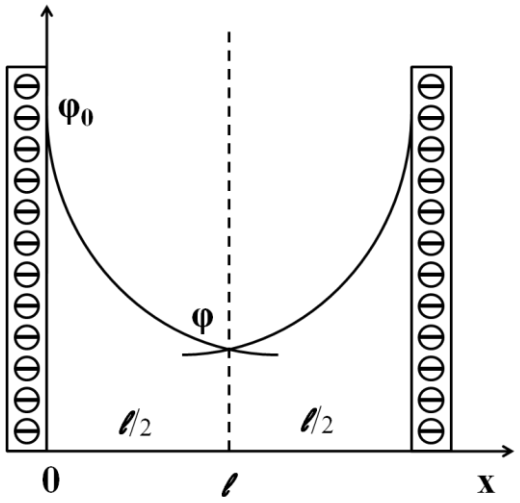


**Figure 2.2** Illustration of two parallel plates with the same charges immersed in an electrolyte.

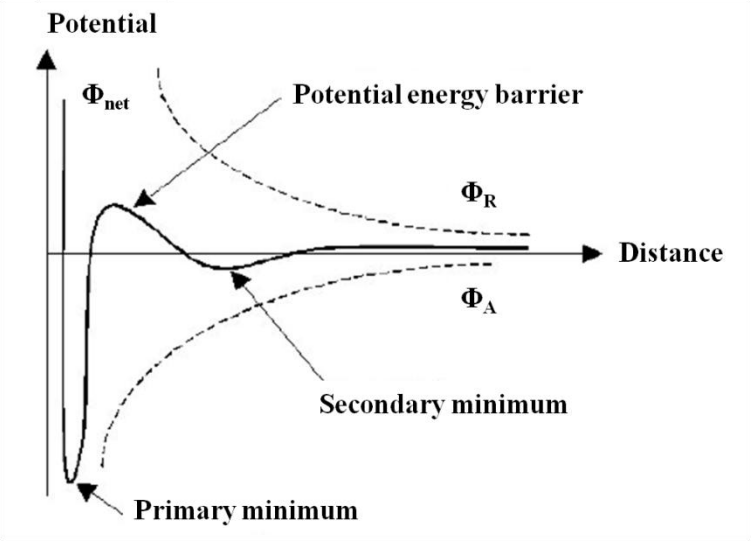


**Figure 2.3** Plot the DLVO potential $\Phi_{net}$ versus the distance between two particles.

### 2.3.4 Limitations of the DLVO theory and the like-charge attraction

As a successor to the D-H theory, for the first time, the DLVO theory gives people a general tool to explain and predict some important solution behaviors of colloidal

systems. However, in the last 40 years, people observed new experimental phenomena which could not be explained by the DLVO theory. For example, Ise and co-workers noticed large void regions in equilibrium with densely packed region for highly charged silica latex particles.[2] Hachisu in 1973 found that an increase of the salt concentration results in melting of colloidal crystals, which according to DLVO theory, the increase of salt concentration should deepen the secondary minimum therefore stabilize the colloidal crystals.[3] Moreover, Schurr and co-workers observed a strange "ordinary-extraordinary phase transition" when they study the effect of adding salt to the dynamics of poly-L-lysine $(lys)_{955}$ solutions. Over a narrow ionic strength range, they found the apparent diffusion coefficient $D_{app}$ - monitored by dynamic light scattering (DLS) - dropped 20 times; indicating there is some sort of clustering is formed in solution.[4,5] From these experimental results, it seems the cause of failures of applying DLVO theory to these systems is stem from the basic assumption that the short-ranged van der Waals is the only attraction source in the colloidal systems. In fact, to explain these experimental phenomena another long-ranged attraction source is needed, which is the counterion mediated electrostatic attraction between colloidal particles.

## 2.4 Self-assembly of POM type macro-anions in solution

### 2.4.1 Blackberry type structure formed by {$Mo_{154}$} POM

As mentioned in Chapter 1, POM type macro-anions are excellent model systems to study because of their high surface charge density, giant size, and well-defined structure. One typical example is the {$Mo_{154}$} giant wheel cluster anions. This molecular cluster, $(NH_4)_{28}[Mo_{154}(NO)_{14}O_{448}H_{14}(H_2O)_{70}]\cdot nH_2O$, was first identified by Dr. Achim Müller and his colleagues.[6] It has been shown that the {$Mo_{154}$} inorganic macro-anions do not exist as discrete ions; instead, they tend to slowly further aggregate into large spherical assemblies. The "aggregates" do not look like regular aggregates formed by less soluble species, which usually have broad size distributions and tend to continue to grow until precipitating from the solution. This self-assembly process is contradictory to our common sense that fully hydrophilic macro-anions should not be attracted to each other but homogeneously distribute through the solution to decrease the total Gibbs free energy. As shown in Fig. 2.5, the transmission electron microscopy (TEM) studies on a dilute {$Mo_{154}$} aqueous solution demonstrate that many spherical assemblies with a relatively uniform size of about 90 nm are formed.[7]

To thoroughly explore the unique self-assembly of {$Mo_{154}$} macro-anions, a combination of dynamic light scattering (DLS) and static light scattering (SLS) techniques are employed. In general, SLS gives information such as weight-average mass ($M_w$), radius of gyration ($R_g$), as well as the nature of interparticle interactions of the studied solute (the second virial coefficient $A_2$) through measuring the scattered intensity from sample solutions at different scattering angles and concentrations. On the other hand,

DLS measurements are intended to determine the hydrodynamic radius ($R_h$) and the size distribution of particles (e.g., polymers, colloids, or bio-macromolecules) in solution. DLS measures the intensity-intensity time correlation function (then converted to electric field time correlation function). Using constrained regularized (CONTIN) method, the time correlation function is analyzed to provide the apparent diffusion coefficients of the solute which can be further used to calculate the $R_h$ through the Stokes–Einstein equation. As shown in Fig. 2.5, a CONTIN analysis of the DLS measurement on a highly diluted $\{Mo_{154}\}$ aqueous solution (0.01mg/mL) at pH = 3.0 shows that large assemblies with an average $R_h$ of 45 $\pm$ 1 nm present in the solution which has a narrow size distribution. SLS study show that the average $R_g$ of the large assemblies is 45.2 $\pm$ 1.4 nm, which simply reflect that $R_g = R_h$. indicating the aggregates are hollow in nature. Recall that the large assemblies are spheres as shown previously in the TEM images; we can conclude that $\{Mo_{154}\}$ macro-anions form spherical, vesicle-like hollow structures in solution. Meanwhile, the apparent molecular weight ($M_w$) of the large assemblies can be estimated from the Zimm plot, which has a value of (2.54 $\pm$ 0.3)$\times 10^7$ g/mol. This $M_w$ value equivalent to ~ 1165 single $\{Mo_{154}\}$ macro-anions also suggests a hollow interior of the aggregates, because a solid $\{Mo_{154}\}$ nanocrystal of 45-nm radius would contain a much bigger number of individual $\{Mo_{154}\}$ macro-anions, greater than 14,000, and would be much heavier. Therefore, we believe that all these giant wheels are homogeneously distributed to form a single layer on the surface of the assemblies. The accurate intermolecular distance is estimated to be ~ 1 nm. The above experimental results inspired us to construct a model system as shown in Fig. 2.5, and we give the vesicles the nickname “blackberry structure” due to the similarities between these two species. One

thing needs to be mentioned is that the current blackberry structure is fundamentally different from the bilayer hollow spherical assemblies such as micelles or biolipids, because on the surface of one blackberry structure, individual $\{Mo_{154}\}$ macro-anions have no obvious hydrophobic regions and they are not in touch with each other.

Not only limited in the $\{Mo_{154}\}$ system, similar giant blackberry structures are also observed in many other POM macro-ionic polar solutions (e.g. $\{Mo_{132}\}$, $\{Mo_{72}V_{30}\}$ and $\{Mo_{368}\}$ in various polar solvents),[8-10] indicating that this type of self-assembly is quite a general process for hydrophilic macro-anions in solution, as long as the macro-ions are large in size (from 2 nm to 6 nm) and carry a moderate number of charges. Currently, the smallest POM cluster shows this self-assembly behavior is $\{W_{48}P_8Cu_{20}\}$.[11]

**Table 2.1** Some general features of giant, hydrophilic POM macro-anions covered in this chapter.

| POM abbreviation[a] | Counterion number | Total charge number | Size (nm) | Charge density ($C/m^2$) |
|---|---|---|---|---|
| $\{Mo_{154}\}$ [12] | 15 | -15 | 3.6 | 0.08 |
| $\{Mo_{132}\}$[13] | 42 | -42 | 2.9 | 0.25 |
| $\{Mo_{72}V_{30}\}$[14] | 34 | -34 | 2.5 | 0.28 |
| $\{Mo_{72}Fe_{30}\}$[15] | 0[b] | -4 ~ -8 | 2.5 | 0.04 ~ 0.07 |
| $\{Mo_{72}Cr_{30}\}$[16] | 0[b] | -4 ~ -8 | 2.5 | 0.04 ~ 0.07 |
| $\{W_{48}P_8Cu_{20}\}$[17] | 25 | -25 | 2.0 | 0.21 |
| $\{Mo_{368}\}$[18] | 48 | -48 | 6.0×4.0 | 0.38 |
| $\{P_4Y_8W_{43}\}$[19] | 21 | -21 ~ -30[c] | 2.0×4.0 | 0.11 ~ 0.16 |

**a**: Detailed formulas can be found in references listed next to each of the POM abbreviation. **b**: For these two molecular clusters, they are neutral in the crystal state but undergo deprotonation when dissolved in aqueous solutions. Therefore, their total surface charge number depends on the degree of deprotonation. **c**: For this cluster, besides 15 $K^+$ and 6 $Na^+$ counter-ions, it also contains 9 $H_3O^+$ counter-ions. Therefore its surface charge density is also affected by solution pH.

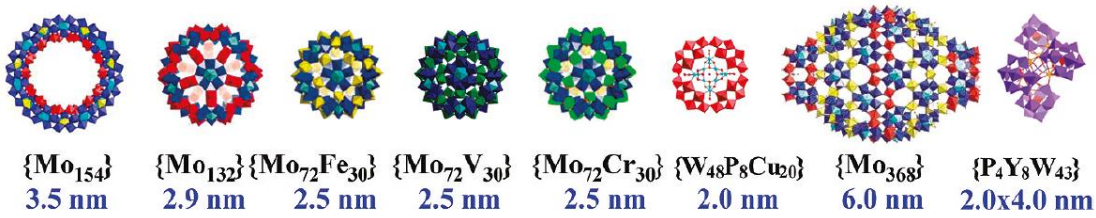


**Figure 2.4.** Some typical giant polyoxometalate molecular clusters (and their sizes) described in the chapter. Their surface charge densities are listed in Table 1.

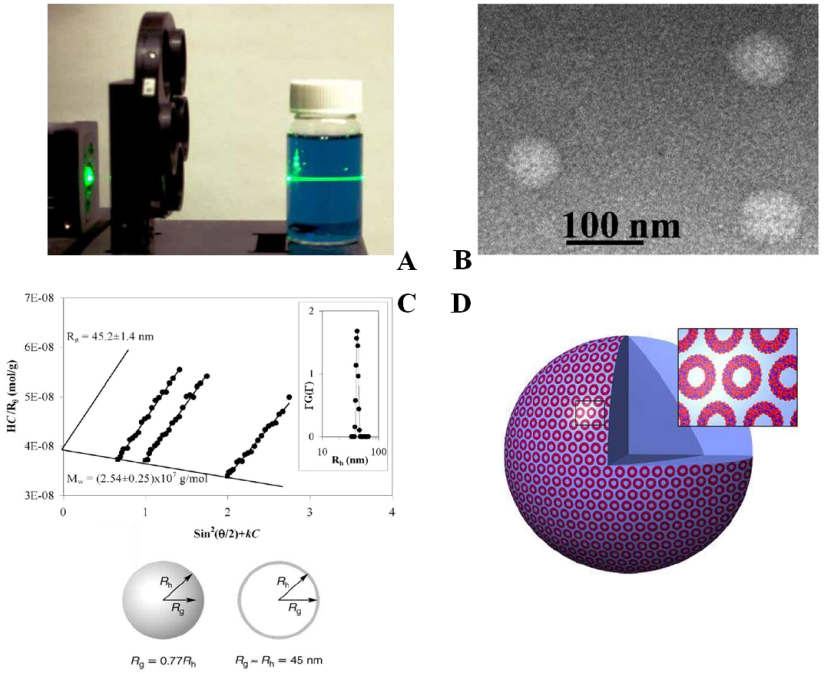


**Figure 2.5** (A) Tyndall effect of a {$Mo_{154}$} aqueous solution when a green laser passes through the solution. (B) TEM image of the blackberry structure formed by {$Mo_{154}$} macro-anions. (C) Zimm plot of a series of {$Mo_{154}$} aqueous solutions reveals the radius of gyration $R_g$ and weight averaged molecular weight ($M_w$) of the large blackberry structure. (D) A cartoon illustrates the blackberry structure. (Copyright: Nature publishing group 2003)

### 2.4.2 The driving forces that responsible for the self-assembly of POMs

In order to uncover this extraordinary self-assembly process in highly charged, fully hydrophilic macro-anionic systems, we need to recognize the forces that surpass the electrostatic repulsion and can bring these macro-anions together. In general, van der Waals forces and hydrogen bonding are two important attractive interactions that are widely observed in different systems.

#### 2.4.2.1 Van der Waals attractions

Van der Waals forces, which are generally attractive in nature, are short ranged and decay rapidly to zero away from a surface. The origin of the van der Waals forces lies in the instantaneous dipole generated by the fluctuation of electron cloud surrounding the nucleus of electrically neutral atoms. In colloidal systems sometimes the van der Waals forces are significant because of the relatively large size of colloidal particles that the contribution from all the atoms are added up, as indicated in equation (41). Therefore, we would expect weaker van der Waals attractive forces because POM macro-anions have relatively small sizes. We can use equation (42) to estimate the effective distance *S* at which the van der Waals attractive potential will have the same magnitude as the repulsive potential. For instance, in a 0.01mg/mL $\{Mo_{154}\}$ aqueous solution at pH = 3.0, this effective distance can be easily calculated as ~ 0.2 nm. Compared with the inter-particle distance estimated from our SLS results (~ 1 nm between two adjacent $\{Mo_{154}\}$ macro-anions), this value indicates the van der Waals forces cannot be the primary or dominant attractions in the blackberry formation process. A more systematic study on a "Keplerate" $\{Mo_{132}\}$ cluster in water/acetone mixed solvents reveals further evidence that van der Waals cannot be the major attraction force.[20]

### 2.4.2.2. Hydrogen bonding.

Recent experimental results from our group and other groups indicate that the hydrogen bonds formed between adjacent POMs on the blackberry surface may be one of the important driving forces for the stability of blackberries. For example, by using dielectric relaxation measurements, Oleinikova *et al*. noticed that, during the self-assembly of $\{Mo_{154}\}$ wheel-shaped macro-ions in aqueous solution, "the strength of the hydration extends as cluster aggregation takes place with more water molecules being more strongly bound between the wheels and the presence of relatively fewer less strongly bound water molecules"; that is, the water stays between $\{Mo_{154}\}$ macro-ions and shows higher viscosity (i.e. more hydrogen bonds formed).[21] In other words, the additional hydrogen bonds help to "glue" the hydrophilic surface of POMs together. The special hydrogen bonding formed between macro-ions on the blackberry surface is reflected by the softness of the blackberry wall. Moreover, Schmitz provides an interesting hypothesis of hydrogen bonded water molecule "fingers" to explain the spherical geometry of blackberries.[22] Fig. 2.6 illustrates the general picture of how the hydrogen bonds may glue $\{Mo_{154}\}$ macro-ions together on the blackberry surface. However, this middle-ranged attraction still could not explain why highly charged macro-anions tend to pull towards to each other especially when the electric double layer of the macro-anions is large ($\kappa^{-1}$ ~ 10 nm for 0.01mg/mL $\{Mo_{154}\}$ solutions at pH = 3.0). There must be some long-ranged attractive interactions which responsible for the blackberry formation.

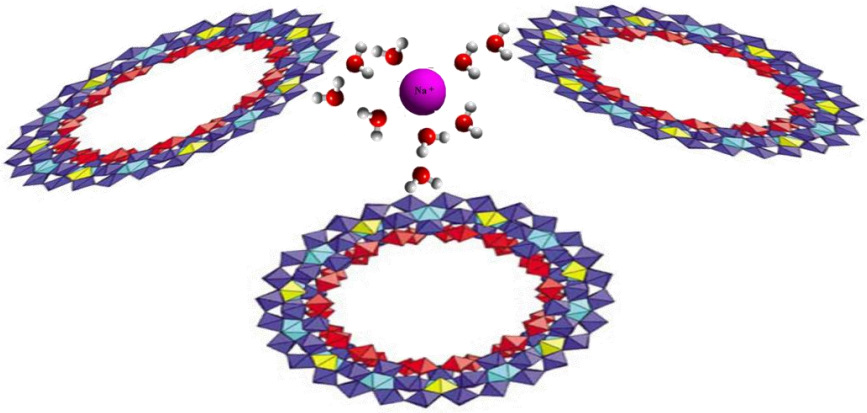


**Figure 2.6** Illustration of how the hydrogen bonded water molecules and small counter-ions arrange them on the surface of the blackberry structure to create a curved spherical shape.

### 2.4.2.3 Counter-ions mediated attractions

The high surface charge density and much larger size of macro-ions make the macro-ions behave fundamentally different from simple electrolyte solutions. In other words, the D-H approximation is no longer suitable to describe the macro-ion solutions. Actually, the electrostatic interactions between macro-ions-macro-ions, macro-ions-counterions and counterions-counterions are much more complex than the simple electrolyte solutions. For example, in bio-macroionic systems, the self-association of cylinder shaped DNA macro-ions induced by divalent or multi-valence counterions was observed under many solution conditions.[23-25] In these systems, counterions with high valence are strongly adsorbed on to the surface of DNA macro-ions and may eventually reverse the sign of DNA surface charge, which is known as over-charging. The reversed DNA macro-ions then attract other DNA macro-ions with a layer of counterions in between. This

counterion mediated attraction is named counterion condensation, a concept developed by Manning and Oosawa in the late 1960s.[26,27] However, the counterion condensation is normally seen in cylinder macro-ions with high valence counterions, for spherical macro-ions with monovalent counterions, this effect is believed to be very small. In the POMs case, the size of POMs is much smaller than colloidal particles or bio-macroions but large enough to display the size disparity (The size ratio between the Keplerates and cations is approximately 10:1, which is noticeable but not as significant as in colloidal suspensions with a size ratio on the order of 1000:1. In this latter case, the counterions can be effectively treated as point charges.); and most of the POMs have spherical or disk shapes. More importantly, during the blackberry formation, no extra or high valence counterions are required. All these conditions indicate that the blackberry structure formation is indeed quite unique.

### 2.4.3 Interactions between discrete macro-ions and counter-ions

For very large POMs such as the Keplerate clusters, the counterion-macroion interaction is expected to be more significant compared with small POMs, such as Keggin POMs. One way to evaluate the macroion-counterion interaction is done by comparing the directly measured conductivity values of two POM macro-anionic solutions with their theoretic values.[28] The measurements indicated the change of counter-ion states with $\{W_{148}\}$ and $\{Mo_{132}\}$ concentration. At very low POM concentrations ($< 1\times10^{-5}$ mol/L), nearly all the counter-ions are free in solution. However, some cations (mainly $NH_4^+$ and $Na^+$) are found to closely associate with $\{W_{148}\}$ or $\{Mo_{132}\}$ macro-anions at higher macro-ionic concentrations, and thus do not contribute to solution conductivity. The degree of counter-ion association shows obvious concentration

dependence before and after dialysis, with large fraction of counter-ions associated with macro-ions at higher concentrations. The disparity on ionic size and charge density between small cations and large macro-anions is the major reason for the counter-ion association.

Another way to directly mapping the counterion distribution around the central macro-ions is to use small-angle X-ray scattering (SAXS), a powerful technique to explore the counterion-macro-ion interactions in many systems. Considering the small size (1 ~ 3 Å) and low concentration (0.4 mM ~ 20 mM) of counterions, it is critique to choose a suitable model system, in order to see the correlation between macro-ions and counterions. $\{Mo_{72}V_{30}\}$ (a 2.5 nm size Keplerate cluster carrying 31 charges with the counterions being 14 $K^+$, 8 $Na^+$, 2 $VO^{2+}$, and 5 $H^+$) was used as the primary probe. This POM macro-ion is a uniform molecular cluster which is stable in dilute solutions. Owing to its simple and highly symmetrical structure, the SAXS scattering curve can be calculated based on their form factors and can be compared with experimental result. $\{Mo_{72}V_{30}\}$ carries a practically large number of charges to ensure the prospect of counterion interactions; and it has a sensible amount of metal counterions to generate a detectable X-ray scattering contrast. Moreover, it does not have co-ions and/or excess salts so that the true physical picture of counterions can be revealed. At the mean time, a powerful synchrotron X-ray source is employed to make sure we can get sufficient X-ray scattering intensity from dilute solutions. As demonstrated in Fig. 2.7, in a diluted 0.26 mM aqueous solution of $\{Mo_{72}V_{30}\}$, the overall SAXS curve can be nicely fit by the form factor of $\{Mo_{72}V_{30}\}$ cluster with a spherical shell model. When the $\{Mo_{72}V_{30}\}$

concentration is less than 0.052mM, the $R_g$ value obtained from the Guinier plot (10.8 ± 0.5 Å) suggests that there is no counterion association around the macro-ions.

Not only does the counterion association show concentration dependency, it is also influenced by the solvent dielectric constant. As shown in Fig. 2.8, the Guinier plot for a series of $\{Mo_{72}V_{30}\}$ solutions with different amount of acetone reflects that the average $R_g$ increases with the acetone content, which means the counterion association becomes stronger when more acetone is introduced. Meanwhile, a more physically meaningful description of the particle morphology, the distance pair distribution p(r), which is the probability of finding the vector length r in a molecule that will become zero at the maximum vector length, can be generated from the Moore analysis. For $\{Mo_{72}V_{30}\}$ in dilute aqueous solutions, the p(r) curves shown in Fig. 2.8 (top) correspond to discrete $\{Mo_{72}V_{30}\}$ clusters (a core shell spherical particle with a maximum linear dimension of ~ 26 Å) with no counterion association. When certain amount of acetone is introduced into the solution, another relatively small and isolated peak appears which is centered at ~ 30 Å and extends the effective distribution to ~ 34 Å (Fig. 2.8, bottom). The peak distribution from 0 to 26 Å remains unchanged, indicating that the $\{Mo_{72}V_{30}\}$ macro-anions are still existing as discrete ions without self-assembling into blackberries (blackberry formation is a very slow process). This additional peak which responsible for additional electron density found outside the $\{Mo_{72}V_{30}\}$ macro-anions, suggests that some counterions are closely associated with the macro-ions and distribute in the range of 2-9 Å to the surface of macro-ions. The appearance of the peak due to associated counterions is consistent with the appearance of the blackberry structures, indicating the direct connection between these two issues.[29]

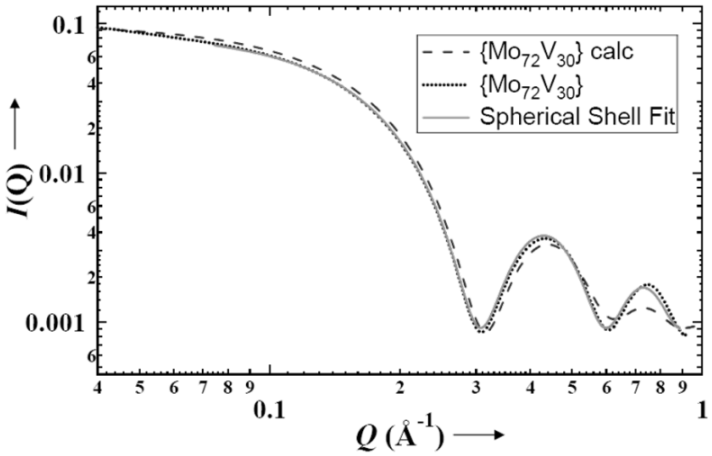


**Figure 2.7** Calculated SAXS patterns for {$Mo_{72}V_{30}$} generated by using *CRYSOL* from the atomic coordinates from the single crystal data (dashed line), calculated form factor of a 2.5-nm-diameter spherical shell (solid line), and experimental scattering data for 0.26 mM {$Mo_{72}V_{30}$} aqueous solution (dotted line).

**Table 2.2** Table of $R_g$ values measured at different {$Mo_{72}V_{30}$} concentrations in aqueous solutions.

| **{$Mo_{72}V_{30}$} g/L** | **$R_g$ (Å)** |
|---|---|
| 0.25 (0.013 mM) | 10.8 ± 0.5 |
| 0.5 (0.026 mM) | 10.8 ± 0.5 |
| 1 (0.052mM) | 10.9 ± 0.5 |
| 5 (0.26 mM) | 11.2 ± 0.6 |

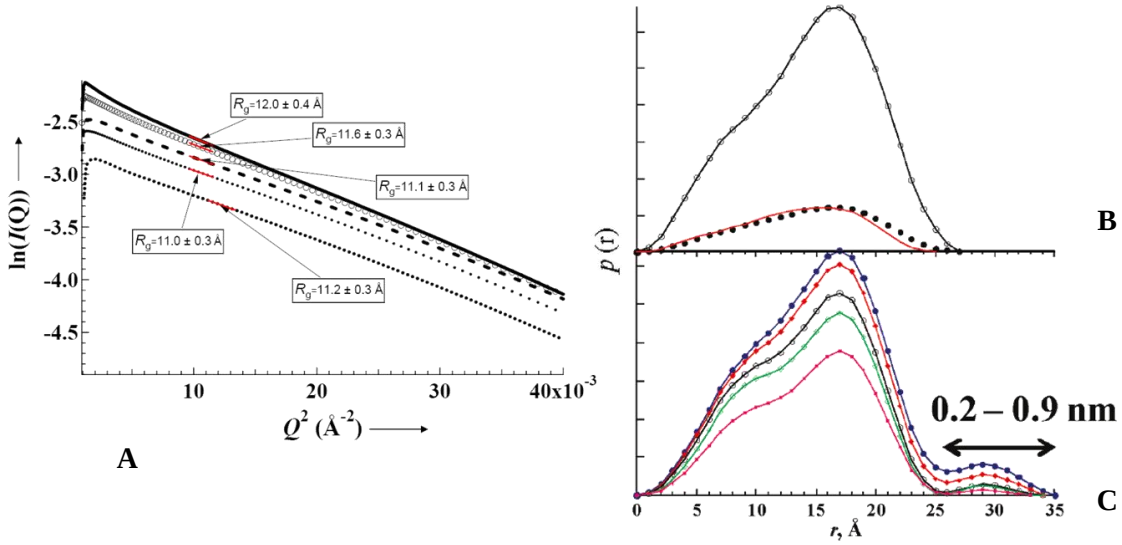


**Figure 2.8** (A) *R*g of 0.26 mM $\{Mo_{72}V_{30}\}$ macro-ions in water and water/acetone mixed solvents containing various amount of acetone (in vol %) (solid line: 75%, open circles: 65%, dashed line: 45%, dotted line: 10 %, open squares: pure water). (B) Pair-distance distribution function plots based on calculated and experimental scattering curves for $\{Mo_{72}V_{30}\}$. (closed circles: 0.013 mM, open circles: 0.052 mM, red line: calculated). (C) Experimental distance distributions for 0.26 mM $\{Mo_{72}V_{30}\}$ in water and acetone/water mixed solvents. (green: 75%, blue: 65%, red: 45%, light blue: 10%, magenta: pure water).

### 2.4.4 Effect of surface charge density

Previous studies indicate that the number of charge on the POMs cluster surface also plays an important role during the blackberry formation. The blackberry size can be accurately tuned by changing the surface charge density. A typical example is $\{Mo_{72}V_{30}\}$, which does not show self-assembly behavior in dilute aqueous solutions due to its high surface charge density. To decrease this electrostatic hindrance, a small amount of water-soluble surfactants, such as cetyltrimethylammonium bromide (CTAB), trimethyltetradecylammonium chloride (CTAT), dodecyltrimethylammonium bromide (DTAB), and octyltrimethylammonium bromide (OTAB) is introduced into the $\{Mo_{72}V_{30}\}$ solutions, such that the charge density on $\{Mo_{72}V_{30}\}$ macro-ions is expected to decrease and enter the blackberry-formation regime. We found that the long-chain CTAB and CTAT surfactants can interact with $\{Mo_{72}V_{30}\}$ stoichiometrically. As a result, $\{Mo_{72}V_{30}\}$ blackberries can be observed at the $\{Mo_{72}V_{30}\}$ to surfactant molar ratio of 1:1.2, and the average $R_h$ of the blackberries continues to increase with increasing surfactant concentration, as shown in Fig. 2.9. The hydrophobic interaction from the surfactant tails might also contribute to the self-assembly, but the effect should be very minor as there are only a few alkyl chains on the relatively large surface area of each macro-ion.[30]

For weak electrolytes of $\{Mo_{72}Fe_{30}\}$, its surface charge comes from the partial deprotonation of water ligands attached to its 30 $Fe^{III}$ centers, so that its surface charge density can be easily tuned by changing the solution pH. By adding a small amount of NaOH or HCl solution, the deprotonation degree of $\{Mo_{72}Fe_{30}\}$ and its charge density can be adjusted. Fig. 2.10 shows the blackberry formation in $\{Mo_{72}Fe_{30}\}$ aqueous solution. At pH < 2.9, $\{Mo_{72}Fe_{30}\}$ clusters are almost uncharged and stay as soluble

molecules in solution. At pH > 2.9, $\{Mo_{72}Fe_{30}\}$ clusters are more charged. Self-assembly occurs with the blackberry size decreasing with increasing pH, from $R_h$ ~ 50 nm at pH = 3.0 to $R_h$ ~ 15 nm at pH = 6.0. The transition from single clusters to blackberries with the change in pH again confirms that van der Waals attractions are not the major attractive forces for the self-assembly.[31]

Not only the Debye screening length ($\kappa^{-1}$) can be influenced by the ionic strength, it is also proportional to the dielectric constant $\varepsilon_r$ of the solvent. In other words, when the polarity of a solvent decreases, the Debye length also decreases and the electric double layer is compressed. Therefore, counter-ions should be more closely associated with macro-ions. In reality, we observed that the average blackberry size increases linearly with increasing $1/\varepsilon_r$ for $\{Mo_{132}\}$, $\{Mo_{72}V_{30}\}$ and $\{W_{72}Mo_{60}\}$ in water/acetone mixed solutions.[32-34] Similar trends have also been identified in other POM solutions.

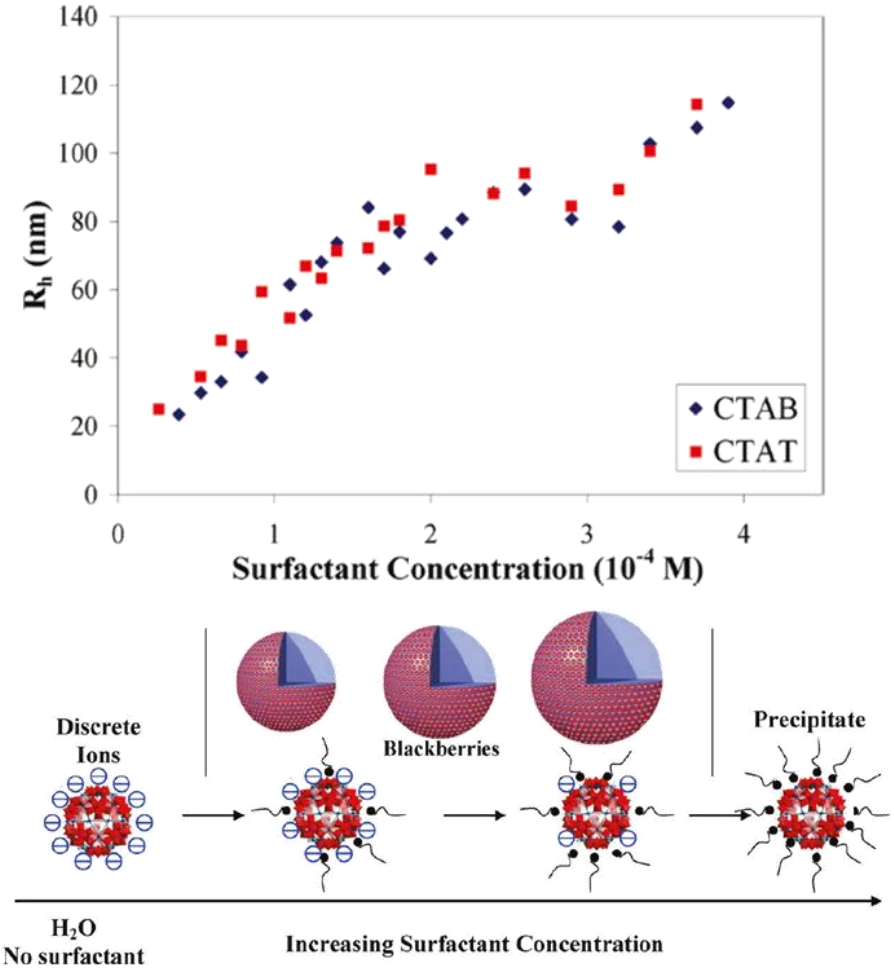


**Figure 2.9** Top: Average hydrodynamic radius ($R_h$) of the $\{Mo_{72}V_{30}\}$ blackberries in aqueous solution increases with surfactant (CTAB or CTAT) concentration. The concentration of $\{Mo_{72}V_{30}\}$ is 0.026 mM. Bottom: Charge density on $\{Mo_{72}V_{30}\}$ decreases with the increment of surfactant concentration, which leads to the increment of blackberries size. (Copyright: American Chemical Society 2009)

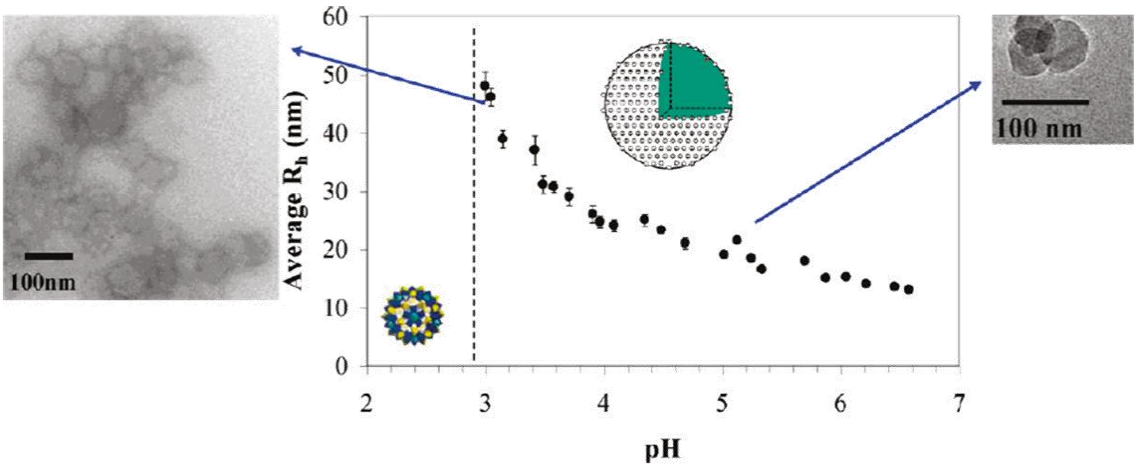


**Figure 2.10** Average $R_h$ of blackberries changes with the solution pH in 0.5 mg/mL $\{Mo_{72}Fe_{30}\}$ aqueous solutions. Left: TEM images of blackberries at pH ~ 3.0. Right: pH ~ 4.6. (Copyright: American Chemical Society 2006)

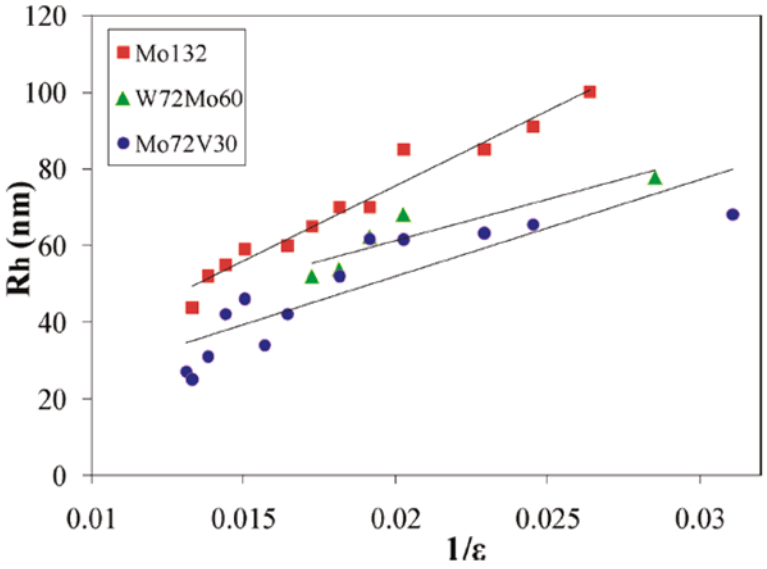


**Figure 2.11** Plot of the average blackberry radius versus the inversed dielectric constant ($1/\varepsilon$) of the solvent for different POMs in water/acetone mixed solvents, demonstrating a linear relationship for these systems. (Copyright: American Chemical Society 2009)

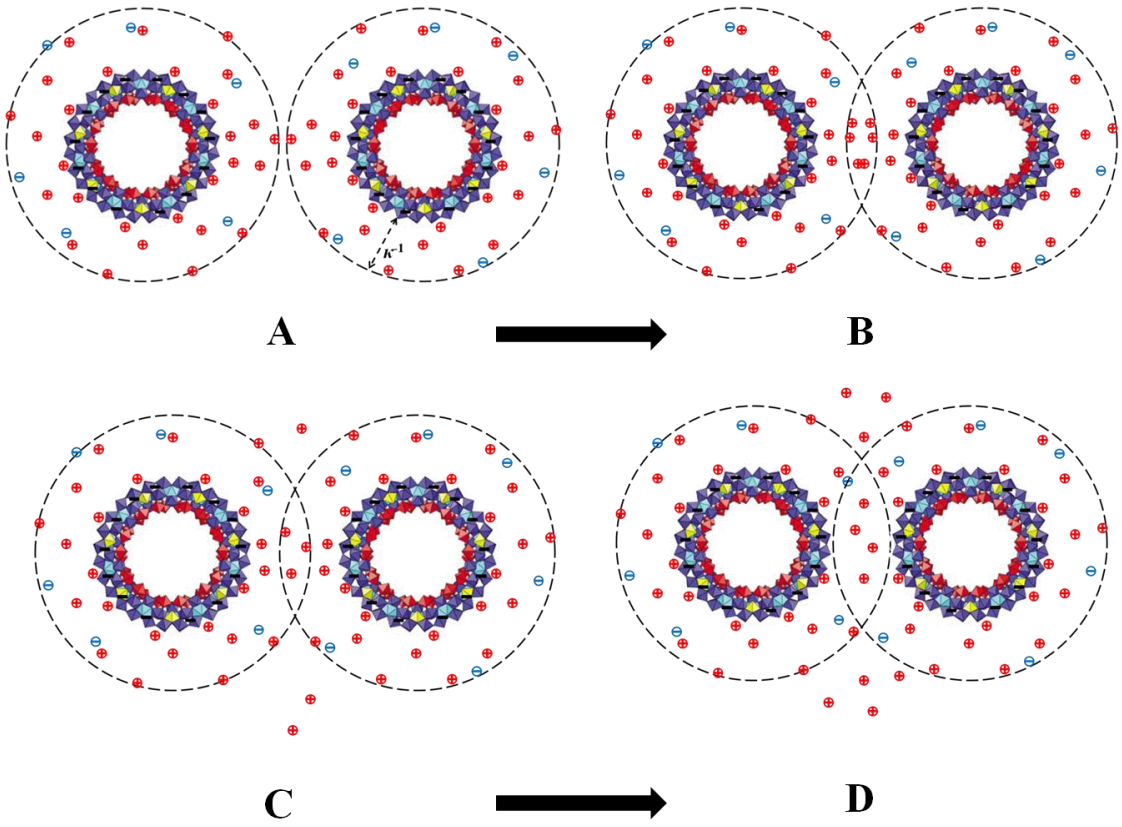


**Figure 2.12** A possible scenario of macro-anion association mediated by counterion effect.

The counterion valence state, their hydration size, and the total ionic strength of the solution are all critical parameters that will affect the counterion mediated attractions between POMs, which will lead to the change of blackberry structure. The ITC studies provide direct confirmation that the binding strength between $\{Mo_{72}Fe_{30}\}$ and monovalent cations follows the order of ($Li^+$, $Na^+$) < $H_3O^+$ < $K^+$ < $Rb^+$ < $Cs^+$, which is completely consistent with the observed corresponding blackberry formation processes.

This is also compelling evidence that the counterions cannot be treated as dimensionless point charges in the macro-ionic solutions.

## 2.5 Conclusions

From the above discussions, we can identify that the dominant driving forces for the blackberry formation are the counterion mediated attraction plus hydrogen bonding. The properties of the attraction can be summarized as follows: The attraction is intensified with decreasing dielectric constant ε when the charge number is practically fixed. The attraction exists with monovalent counterions. When the salt concentration and/or the charge number are very low, the attraction is not strong enough to be detected. When the two parameters become larger, the attraction is intensified. With further increase, the attraction becomes weaker again. Even when two macro-ions are far apart, a large part of their charge is already compensated by their counterions. Consequently, the enthalpy change that accompanies macro-ion association is modest. However, when the macro-ions do associate, a number of opposite charges on the two macro-ions are brought in close proximity and a proportional number of counterions are no longer needed and can be freed. It is the entropy gain of these released counterions that is largely responsible for the binding process (Fig. 2.12). The release of water molecules, associated with changes in solvent structure is also important. To account for the spherical geometry of blackberry structure, first form dimer or oligomers, then form a sheet, then to decrease edge energy, the sheet collapses into a vesicle. This also clearly distinguishes soluble macro-ions with large colloidal suspensions. In the blackberry region, the blackberry size decreases monotonically with increasing water content, suggesting that the blackberry size can be

accurately controlled. By simply adjusting the solvent content with mild heating, the transitions between the blackberries and discrete macro-ions, and between the blackberries with different sizes, can be achieved. It confirms that the blackberry formation is a physical process which does not involve major chemical reactions.

## References


(1) Hiemenz, P. C.; Rajagopalan, R. *Principles of Colloid and Surface Chemistry*; 3rd ed.; CRC Press: New York, 1997.

(2) Ise, N.; Sogami, I. S. *Structure Formation in Solution: Ionic Polymers and Colloidal Particles*; Springer: Heidelberg, 2005.

(3) Kose, A.; Ozaki, M.; Takano, K.; Kobayashi, Y.; Hachisu, S. *Journal of Colloid and Interface Science* **1973**, *44*, 330.

(4) Lee, W. I.; Schurr, J. M. *Biopolymers* **1974**, *13*, 903.

(5) Schmitz, K. S.; Lu, M.; Singh, N.; Ramsay, D. J. *Biopolymers* **1984**, *23*, 1637.

(6) Müller, A.; Krickemeyer, E.; Meyer, J.; Bögge, H.; Peters, F.; Plass, W.; Diemann, E.; Dillinger, S.; Nonnenbruch, F.; Randerath, M.; Menke, C. *Angew. Chem. Int. Ed.* **1995**, *34*, 2122.

(7) Liu, T.; Diemann, E.; Li, H.; Dress, A. W. M.; Muller, A. *Nature* **2003**, *426*, 59.

(8) Muller, A.; Diemann, E.; Kuhlmann, C.; Eimer, W.; Serain, C.; Tak, T.; Knochel, A.; Pranzas, P. K. *Chem. Commun.* **2001**, 1928.

(9) Zhang, J.; Keita, B.; Nadjo, L.; Mbomekalle, I. M.; Liu, T. *Langmuir* **2008**, *24*, 5277.

(10) Chen, B.; Jiang, H.; Zhu, Y.; Cammers, A.; Selegue, J. P. *J. Am. Chem. Soc.* **2005**, *127*, 4166.

(11) Liu, G.; Liu, T. B.; Mal, S. S.; Kortz, U. *J. Am. Chem. Soc.* **2006**, *128*, 10103.

(12) Müller, A.; Das, S. K.; Fedin, V. P.; Krickemeyer, E.; Beugholt, C.; Bögge, H.; Schmidtmann, M.; Hauptfleisch, B. *Zeitschrift für anorganische und allgemeine Chemie* **1999**, *625*, 1187.

(13) Müller, A.; Krickemeyer, E.; Bögge, H.; Schmidtmann, M.; Peters, F. *Angew. Chem. Int. Ed.* **1998**, *37*, 3359.

(14) Botar, B.; Kogerler, P.; Hill, C. L. *Chem. Commun.* **2005**, 3138.

(15) Müller, A.; Sarkar, S.; Shah, S. Q. N.; Bögge, H.; Schmidtmann, M.; Sarkar, S.; Kögerler, P.; Hauptfleisch, B.; Trautwein, A. X.; Schünemann, V. *Angew. Chem. Int. Ed.* **1999**, *38*, 3238.

(16) Todea, A. M.; Merca, A.; Bögge, H.; van Slageren, J.; Dressel, M.; Engelhardt, L.; Luban, M.; Glaser, T.; Henry, M.; Müller, A. *Angew. Chem. Int. Ed.* **2007**, *46*, 6106.

(17) Mal, S. S.; Kortz, U. *Angew. Chem. Int. Ed.* **2005**, *44*, 3777.

(18) Müller, A.; Beckmann, E.; Bögge, H.; Schmidtmann, M.; Dress, A. *Angew. Chem. Int. Ed.* **2002**, *41*, 1162.

(19) Howell, R. C.; Perez, F. G.; Jain, S.; DeW. Horrocks, J. W.; Rheingold, A. L.; Francesconi, L. C. *Angew. Chem. Int. Ed.* **2001**, *40*, 4031.

(20) Kistler, M. L.; Bhatt, A.; Liu, G.; Casa, D.; Liu, T. *J. Am. Chem. Soc.* **2007**, *129*, 6453.

(21) Oleinikova, A.; Weingärtner, H.; Chaplin, M.; Diemann, E.; Bögge, H.; Müller, A. *ChemPhysChem* **2007**, *8*, 646.

(22) Schmitz, K. S. *J. Phys. Chem. B* **2009**, *113*, 2624.

(23) Qiu, X.; Andresen, K.; Kwok, L. W.; Lamb, J. S.; Park, H. Y.; Pollack, L. *Phys. Rev. Lett.* **2007**, *99*, 038104.

(24) Das, R.; Mills, T. T.; Kwok, L. W.; Maskel, G. S.; Millett, I. S.; Doniach, S.; Finkelstein, K. D.; Herschlag, D.; Pollack, L. *Phys. Rev. Lett.* **2003**, *90*, 188103.

(25) Qiu, X.; Andresen, K.; Lamb, J. S.; Kwok, L. W.; Pollack, L. *Phys. Rev. Lett.* **2008**, *101*, 228101.

(26) Oosawa, F. *Biopolymers* **1968**, *6*, 1633.

(27) Manning, G. S. *J. Chem. Phys.* **1969**, *51*, 924.

(28) Liu, G.; Kistler, M. L.; Li, T.; Bhatt, A.; Liu, T. *J. Cluster Sci.* **2006**, *17*, 427.

(29) Pigga, J. M.; Kistler, M. L.; Shew, C. Y.; Antonio, M. R.; Liu, T. B. *Angew. Chem. Int. Ed.* **2009**, *48*, 6538.

(30) Kistler, M. L.; Patel, K. G.; Liu, T. *Langmuir* **2009**, *25*, 7328.

(31) Liu, T.; Imber, B.; Diemann, E.; Liu, G.; Cokleski, K.; Li, H.; Chen, Z.; Müller, A. *J. Am. Chem. Soc.* **2006**, *128*, 15914.

(32) Verhoeff, A. A.; Kistler, M. L.; Bhatt, A.; Pigga, J.; Groenewold, J.; Klokkenburg, M.; Veen, S.; Roy, S.; Liu, T.; Kegel, W. K. *Phys. Rev. Lett.* **2007**, *99*, 066104.

(33) Kistler, M. L.; Liu, T.; Gouzerh, P.; Todea, A. M.; Muller, A. *Dalton Transactions* **2009**, 5094.

(34) Schäffer, C.; Merca, A.; Bögge, H.; Todea, A. M.; Kistler, M. L.; Liu, T.; Thouvenot, R.; Gouzerh, P.; Müller, A. *Angew. Chem. Int. Ed.* **2009**, *48*, 149.

# Chapter 3: Self-assembly of Nanocage Type Macro-cations in Solution

## 3.1 Introduction

All the POMs we have mentioned in the previous chapters are macro-anions in nature, and their unique self-assembly behaviors in aqueous solutions indicate counterion induced like-charge attractions play a dominant role. Naturally, we want to ask the following questions: Does this unique self-assembly only hold true for macroanions or it is a universal phenomenon? Will macrocations also self-assembly into large structures in solution? To answer these interesting and important questions, in this chapter, we will focus our attention to nanocage type macrocations.

## 3.2 Materials and instrumentations

### 3.2.1 Materials

Two metal-organic hybrid nanocages were chosen as model systems. The first one $Pd_6L_4(NO_3)_{12}$ {Pd = ethylenediamine palladium(II), L = 2,4,6-tris(4-pyridyl)-triazine} metal-organic nanocage is commercially available (Wako), which has an octahedral shape and a diameter of ~ 2 nm.[1]

The second $M_{12}L_{24}$ nanocages were synthesized based on a procedure in literature and characterized by $^1$H NMR.[2] For a typical experiment, 37 mg (160 mmol) of $Pd(NO_3)_2$ was dissolved in 10 mL of dimethyl sulfoxide DMSO-*d*6 in a 30-mL round bottom flask. The mixture was heated at 70 ℃ for four hours. The resulting mixture was then filtered using a membrane filter with 0.20 μm pore size. A quantitative analysis of the palladium

content was performed by atomic absorption analysis, and typically the resulting Pd concentration was ~10 mM. Next, in a 10-mL test tube, 5.9 mg (20 μmol) of ligand (2,6-bis(4-pyridylethynyl)toluene) was dissolved in 1.0 mL (10 μmol) of the $Pd(NO_3)_2$ solution. The mixture was heated at 70 ℃ for 2 – 5 hours. The resulted nanocage concentration was ~ 835 μmol/L. After cooling down the test tube, the solution was transferred into a 5-mm standard NMR tube and sealed; then followed by $^1$H NMR studies. The diluted nanocage samples were prepared by transferring 10 ~ 100 μL solutions from the original solution into a clean light scattering sample cell containing 4 – 5 mL dust-freed DMSO. The dilution of stock solutions was executed before the slow self-assembly process in solution.

### 3.2.2 DLS and SLS

Both Dynamic Light Scattering (DLS) and Static Light Scatting (SLS) were used to characterize the dilute nanocage solutions. A Brookhaven Instruments *Inc*. light scattering spectrometer, equipped with a diode-pumped solid-state (DPSS) laser operating at 532 nm and a BI-9000AT multi-channel digital correlator were used for this purpose.

The SLS was performed over a broad range of scattering angles from 30 °to 130 °, with a 2 ° interval. The raw data was analyzed to give the radius of gyration ($R_g$) and the weight-average molecular mass ($M_w$) of the large assemblies, using the Rayleigh-Gans-Debye equation:

$$Hc/R_{90}=1/M_w+2A_2*c \quad (43)$$

where H is an optical parameter; $M_w$ is the weight-average molecular mass of the solutes; $A_2$ is the second virial coefficient and $c$ is the solute concentration. The nanocage solutions examined in this study had very low concentrations; therefore, the $2A_2c$ term can be neglected during calculations.

For DLS measurements, the intensity-intensity time correlation functions were analyzed by the constrained regularized (CONTIN) method in order to ascertain the average hydrodynamic radius ($R_h$) of the large assemblies. Specifically, an average apparent translational diffusion coefficient, $D_{app}$ was determined from the normalized distribution function of the characteristic line width, Γ(G); and the hydrodynamic radius $R_h$ is related to $D$ through the Stokes–Einstein equation:

$$R_h = k_B T/6\pi\eta D \tag{44}$$

where $k_B$ is the Boltzmann constant and $\eta$ the viscosity of the solvent at temperature T. The particle size distribution in solution can be obtained by plotting ΓG (Γ) versus $R_h$, with $\Gamma_i G_i$ ($\Gamma_i$) being proportional to the angular-dependent scattered intensity of particle $i$ having an apparent hydrodynamic radius $R_{h,i}$. The temperature in the sample chamber was controlled to within ±0.1 ℃.

### 3.2.3 Electron microscopy

Samples for electron microscopy characterization were prepared by pipeting 5 μL of diluted nanocage solution onto a carbon-coated TEM grid. The TEM samples were left under ambient conditions for several hours while the solvent evaporated. Bright-field (BF) TEM imaging was performed on a JEOL 2000FX transmission electron microscope having an accelerating voltage of 200 kV. High-angle annular dark field (HAADF)

imaging in a scanning transmission electron microscope (STEM) was used to provide Z-contrast information of the sample. The atomic-resolution STEM-HAADF imaging experiments were performed on a JEOL-2200FS (S)TEM equipped with a CEOS spherical aberration corrector. The samples were illuminated by a strong and broad electron beam for a few seconds (also known as 'beam shower') before the high resolution STEM-HAADF imaging in order to fix the mobilized hydrocarbon molecules on the sample surface. The HAADF images presented have been low-pass filtered in order to reduce the background noise.

### 3.2.4 Nuclear magnetic resonance (NMR)

Two dimensional Diffusion-Ordered Spectroscopy (DOSY) $^{1}$H NMR was performed on a Bruker 500 MHz spectrometer with the magnetic field gradient ($g$) varying from 0 to 32 G/cm in 32 ~ 128 steps. The length of the gradient ($\delta$) was from 6000 μs to 8000 μs, and the time interval between two pulsed-gradients ($\Delta$) was from 0.1 s to 0.15 s. All spectra were taken at room temperature. After the data collection, FIDs were processed and analyzed with the NMR software TopSpin 2.0 provided by Bruker. Both T1/T2 relaxation and CONTIN methods were used to fit the raw data. The observed proton signal $I$ in a standard DOSY spectrum is expressed through equation:

$$I = I_0 \exp\left[-(2\pi\gamma\delta)^2\left(\Delta - \delta/3\right)D\mathrm{g}^2\right] \tag{45}$$

where $I_0$ is the reference intensity, $\gamma$ is the gyromagnetic ratio of the proton. If only one diffusive component exists in the solution, a straight line will occur in a plot of $\ln(I/I_0)$ versus $g^2$, and the apparent diffusion coefficient $D$ can be calculated from the slope using linear regression analysis.

## 3.3 Solution behaviors of $M_6L_4$ type nanocages

### 3.3.1 Self-assembly process in water/acetone mixed solvent

The $Pd_6L_4(NO_3)_{12}$ {Pd = ethylenediamine palladium(II), L = 2,4,6-tris(4-pyridyl)-triazine} metal-organic nanocage (Fig. 3.1) carries 12 positive charges attributed to 6 $Pd^{2+}$ ions, after releasing 12 $NO^{3-}$ counterions into solution. The $Pd_6L_4(NO_3)_{12}$ solutions were studied by dynamic and static light scattering (DLS and SLS) techniques. In a pure aqueous solution, very low scattered intensity was collected by SLS after several weeks, indicating that there was no large structure forming in solution; *i.e.*, the cages existed as discrete macrocations. This is due to the high charge density of the nanocages and not a surprise for highly soluble ions. However, when different amounts of acetone were added into the aqueous solutions of nanocages, a significant and continuous increase of the total scattered intensity from SLS was observed, suggesting the formation of much larger structures. The nanocages are still quite soluble in such water/acetone mixtures (up to 75 v% acetone at 0.20 mg/mL) and form clear, stable, homogeneous solutions. Therefore, the growth of the scattered intensity is not due to the aggregation of insoluble species but a slow self-association process of individual cages. As revealed in Fig. 3.2, the peaks obtained by Constrained Regularization (CONTIN) analysis[3] from DLS studies of a 0.20 mg/mL nanocage solution with 22 v% acetone are attributed to supramolecular structures which are dominant in solution and have narrow size distributions. The average hydrodynamic radius ($R_h$) of the large structures does not change with time, indicating that such supramolecular structures have preferred curvatures in solution. Besides, in a 0.06 mg/mL nanocage solution containing 40 v% acetone, the average $R_h$ is 38 $\pm$ 1.0 nm

measured at a 90° scattering angle. Extrapolating the $R_h$ values to a 0° scattering angle results in an $R_{h,0}$ of 40.5 nm. SLS measurements performed on the same solutions indicate that the average radius of gyration ($R_g$) of the supramolecular structures is 40.8 ± 0.8 nm. Therefore, the ratio $R_g/R_h$ is very close to 1. It serves as strong evidence that the assemblies formed by $Pd_6L_4$ cationic nanocages observed at this circumstance have a hollow, vesicle-like structure. TEM studies also clearly show the presence of uniform, hollow, vesicle-like structures formed by $Pd_6L_4$ cationic nanocages, with the average radius of 40 nm in 40 v% acetone solutions, which is consistent to the DLS and SLS studies. It is known that the amphiphilic surfactants and phospholipids form bilayer vesicle structures due to the hydrophobic interactions. In contrast, fully hydrophilic inorganic polyoxometalate (POMs) macroanions can form single layer, vesicle-like "blackberry" structures due to the counterion-mediated attraction and hydrogen bonds.

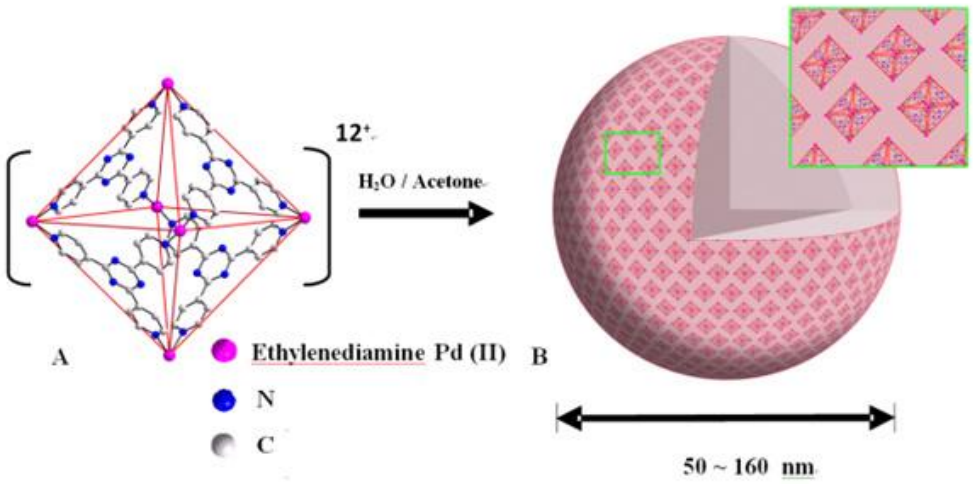


**Figure 3.1** (A) Three-dimensional structure of a single metal-organic nanocage molecule. (B) The supramolecular blackberry type structure determined by laser light scattering measurements and TEM.

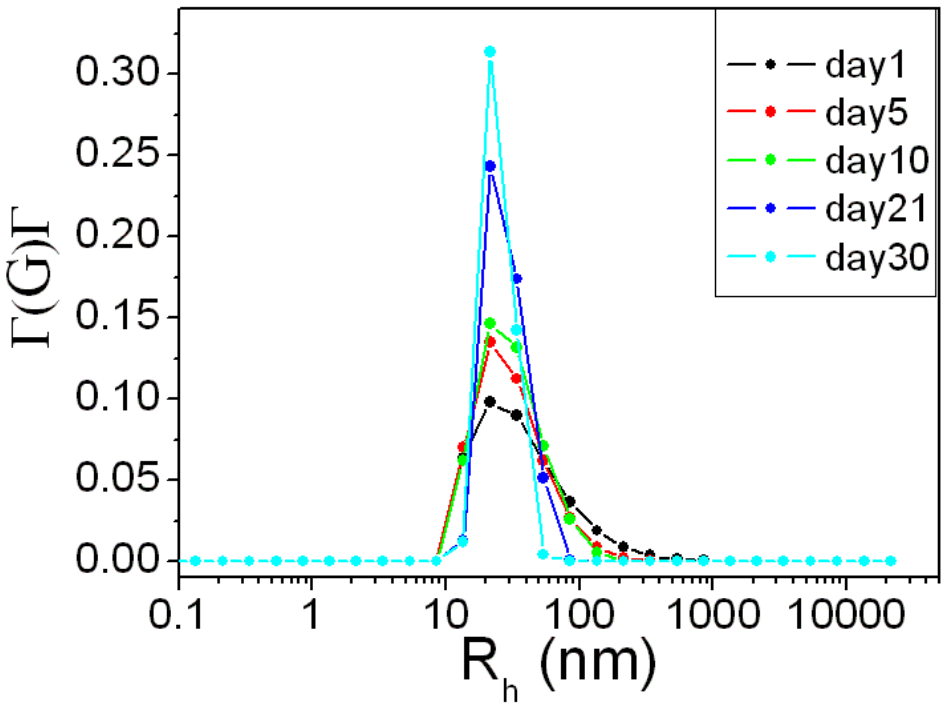


**Figure 3.2** Hydrodynamic radius ($R_h$) distributions of 0.20 mg/mL $Pd_6L_4$ cationic nanocage aqueous solution with 22 v% acetone after 1, 5, 10, 21, and 30 days. The scattering angle is set at 90 °.

### 3.3.2 Driving forces for the self-assembly of $Pd_6L_4$ nanocages

The current $Pd_6L_4$ nanocages are macrocations, which certainly show similarities to POM macro-anions. A major difference between nanocages and POMs is that the POMs are fully hydrophilic while the nanocages contain both hydrophilic ($Pd^{II}$ ions) and hydrophobic parts (tritopic aromatic ligands). On the other hand, the nanocages also differ from amphiphilic surfactants, which usually have a hydrophilic polar head and a hydrophobic "end". The nanocages lack such "ends" because of their highly isotropic

symmetry. Therefore, both electrostatic and hydrophobic interactions could contribute to their vesicle formation.

To clarify the driving force for the self-assembly of nanocages, we first investigated the effect of solvent polarity (in the form of dielectric constant $\mathcal{E}_R$) on the vesicle size. At a concentration of 0.20 mg/mL, the $R_h$ of nanocage vesicles increases monotonically from 25 to 80 nm with increasing acetone content, as shown in Fig. 3.3. By plotting the $R_h$ of the vesicles versus 1/ $\mathcal{E}_R$ of the solvent, a linear relationship is demonstrated, indicating that the cage vesicles with preferred curvatures are stabilized by the charge regulation mechanism. It suggests that the nanocage macrocations can spontaneously and reversibly form vesicle-like structures in polar solvents as long as they possess appropriate charge density. The hydrophobic interaction raised from the aromatic ligands does not play a major role in the self-assembly. If the hydrophobic interaction is the dominant driving force, then it would be much easier and probably faster for the nanocage vesicle formation in pure water than in water/acetone mixtures, because a stronger hydrophobic interaction is expected to be present in the former solution (the hydrophobic ligands become better solvated when acetone is introduced). However, no supramolecular structures formed in pure water, which is a clear argument against the possibility of hydrophobic interaction being the major attractive force. Similar results were obtained in other mixed solvent systems such as water/EtOH. Therefore, we conclude that the nanocage macrocations behave similarly to macro-anionic POMs in solution, *i.e.*, form "blackberry"-type structures with the help of counterion mediated attractions. Additional evidence comes from the very slow vesicle formation process (takes days to weeks, revealed by the very slow increment of the scattered intensity), which is very similar to

the process of the POM blackberry formation but certainly different from the formation of bilayer vesicles.

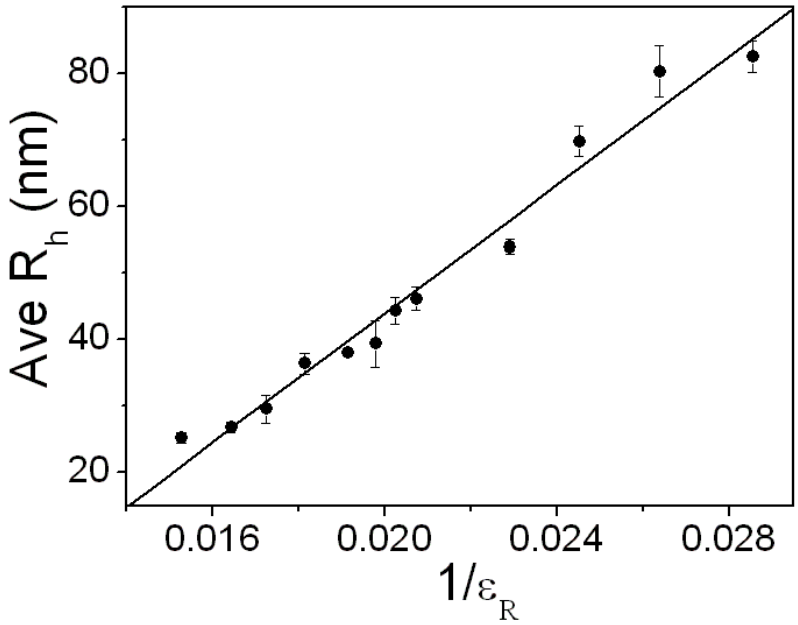


**Figure 3.3** Average $R_h$ of vesicle-like structures in 0.20 mg/mL nanocage aqueous solutions containing different volume of acetone is plotted over the inverse dielectric constant of the solvent.

## 3.4 Solution behaviors of $M_{12}L_{24}$ type nanocages

### 3.4.1 Self-assembly process in DMSO

Unlike our previously studied $M_6L_4$ type nanocages which have an octahedral geometry with 4 open faces, the $M_{12}L_{24}$ type nanocages {M = Pd, L = 2,6-bis(4-pyridylethynyl)toluene} type nanocage possess a cuboctahedral structure with 12 $Pd^{II}$ metal cations (hydrophilic centers) evenly distributed on the almost spherical cage surface (Fig. 3.4) and linked by hydrophobic linkers. We previously reported the vesicle

formation but did not have direct evidence to prove our single-layer model of the large assemblies. Herein, we explore the possible self-assembly process of the $M_{12}L_{24}$ macrocations and compare it with other systems. In particular, we use $M_{12}L_{24}$ as a model system to test a new approach of studying the equilibrium between discrete and aggregated nanocages by NMR. This information is crucial for interpreting laser light scattering results in order to obtain the average inter-cage distance in the assemblies, an important value for understanding the nature of the interactions between the macroions.

$M_{12}L_{24}$ nanocages can be readily synthesized in DMSO, acetonitrile and other polar solvents, and each nanocage cluster carries 24 positive charges, balanced by 24 nitrates. They are thermodynamically stable and our $^{1}H$ NMR results also confirm that once being synthesized in DMSO-*d*6, these nanocages can stay in solution for months without any decomposition or precipitation (Fig. 3.5), which enables us to explore their solution behavior.

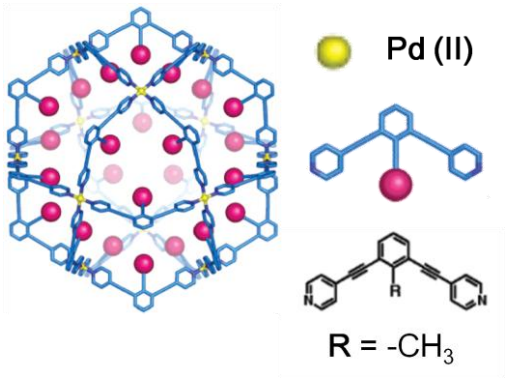


**Figure 3.4** The molecular structures of the $M_{12}L_{24}$ type nanocage.

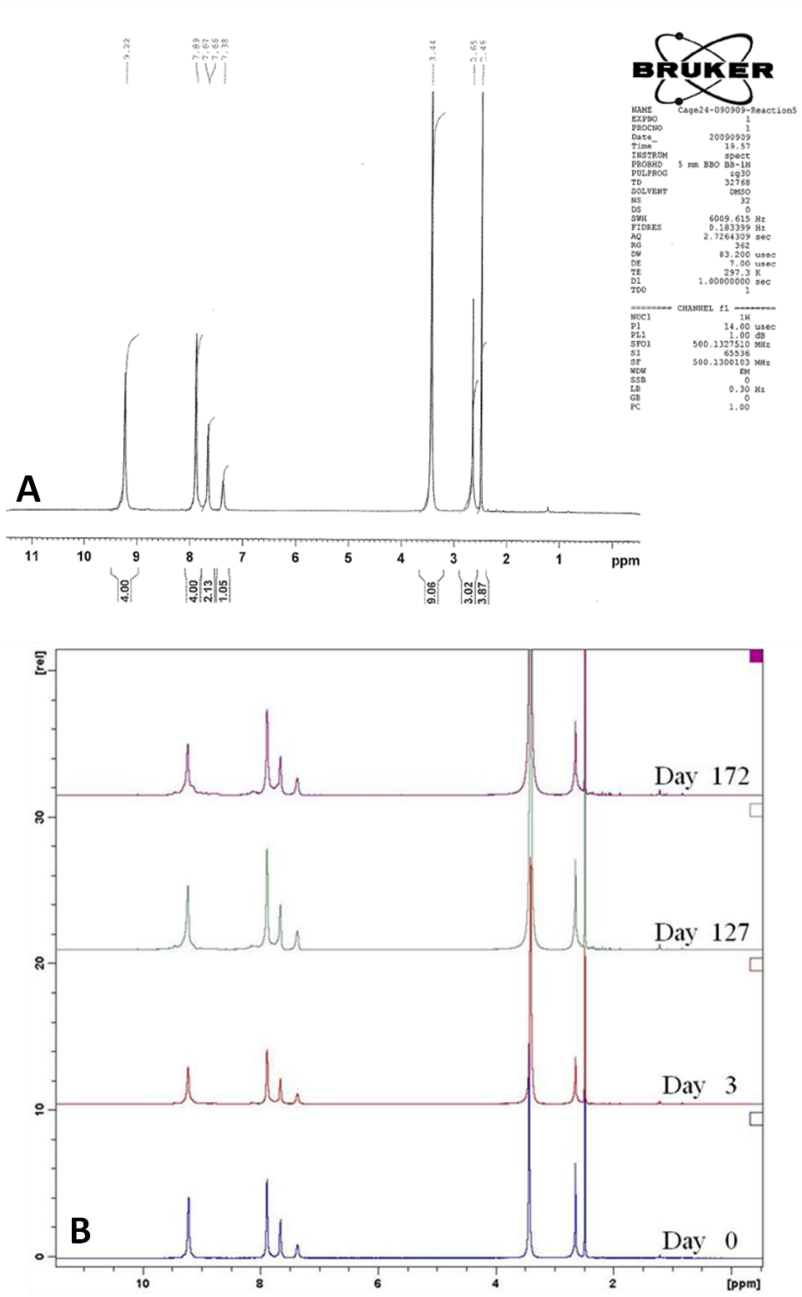


**Figure 3.5** $^{1}$H NMR spectra of $M_{12}L_{24}$ nanocages synthesized in DMSO-*d*6 with no additional $NO_3^-$ counter-ions at initial day 0 (A) and subsequent days (B).

The cationic cages are found to self-assemble into larger structures in DMSO-*d*6, as confirmed by the continuous increase of the total scattered intensity of the solution from SLS studies and a mode corresponding to large structures from DLS studies. DLS data presented in Fig. 3.6 indicate that the large assemblies have narrow size distributions and their average sizes (in $R_h$) do not show an obvious angular dependence (Fig. 3.7), which suggests a spherical shape for the assemblies. Meanwhile, the apparent average $R_g$ values of the large assemblies obtained from SLS studies reveal how the mass of the large assembles is distributed. As shown in Fig. 3.8D, a series of $M_{12}L_{24}$ solutions were prepared by diluting a concentrated $M_{12}L_{24}$ solution in DMSO (for this sample, the molar ratio of nanocage/$NO_3^-$ is 1/36). By extrapolating the $R_g$ values to zero nanocage concentration, a final $R_{g,0}$ value of 38.0 ± 2.0 nm was obtained, very similar to the average $R_{h,0}$ value of 37.8 ± 1.8 nm obtained from DLS measurements. Generally, the ratio of $R_{g,0}/R_{h,0}$ reflects the shape and morphology of the particles in solution, whereby a solid sphere normally has a value of 0.77, while a hollow sphere has a value close to 1. Therefore, the relation of $R_{g,0} \sim R_{h,0}$ in this case indicates that the self-assembled large structures are hollow spheres.

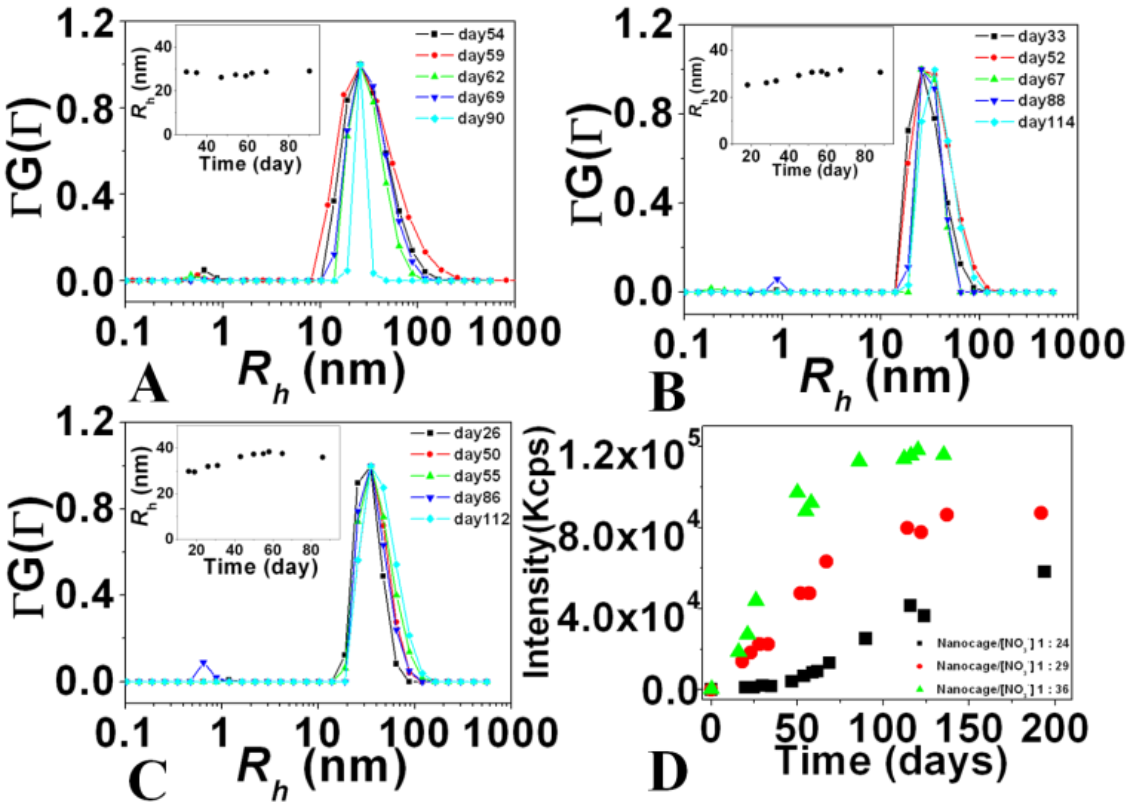


**Figure 3.6** The self-assembly process of three $M_{12}L_{24}$ nanocages samples with different $NO_3^-$ concentrations in DMSO-*d*6 as monitored by SLS and DLS. The size distributions of the aggregates formed in solution, as calculated using CONTIN, when the molar ratio of nanocage/($NO_3^-$) is 1/24 for (A); 1/29 for (B) and 1/36 for (C). (Inset is the average $R_h$ value versus time.) (D) The total scattered intensity changes with time for the three samples.

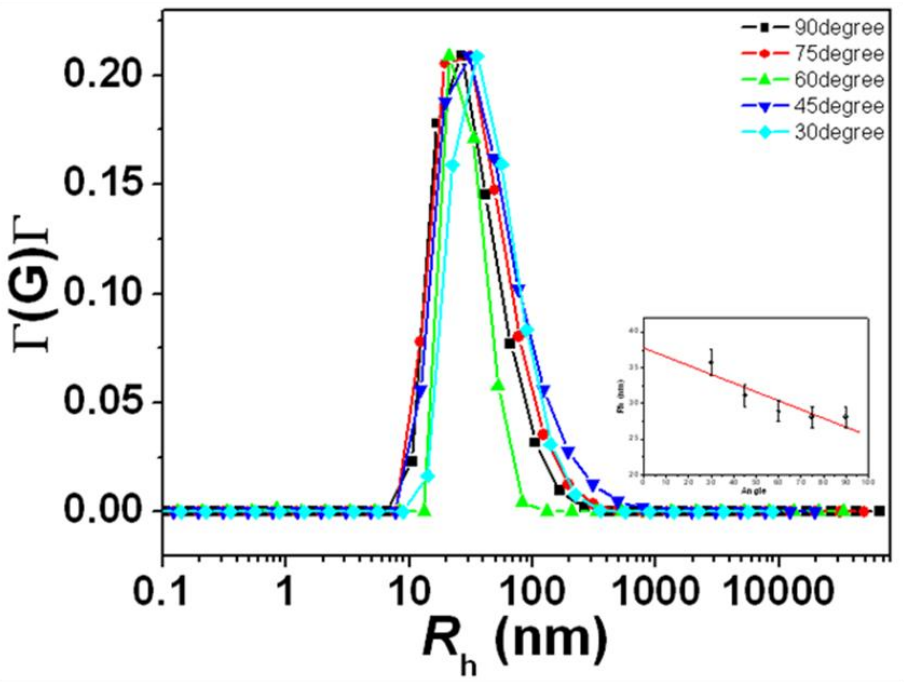


**Figure 3.7** Hydrodynamic radius ($R_h$) recorded at different scattering angles for the large vesicle-like structures self-assembled from $M_{12}L_{24}$ nanocages in diluted DMSO solutions. Inset: $R_{h,0}$ calculated from extrapolating the $R_h$ values obtained at different angles.

### 3.4.2 Estimation of inter-nanocage distance

One piece of crucial information in exploring the unique blackberry structure formation and understanding the macro-ion-counterion interaction is the inter-particle distance between monomers on the surface of the blackberry, which can be used for judging the nature of the attractive interactions between cationic cages. Our previous studies on POMs type blackberries show the interparticle distance is in the range of ~ 1 nm, which is based on the assumption that all single monomers form blackberries.[4] However, to accurately measure this distance is a major difficulty in reality because the blackberry structure is always in dynamic equilibrium with monomers in solution.

Therefore, normal separation methods like filtration, centrifugation or running columns may disrupt and shift this equilibrium. Without knowing the exact population of monomers and blackberries, it is hard to estimate the real number of monomers on each blackberry surface.

This problem is solved by using of NMR and SLS. Time-resolved SLS studies reveal more information about the slow self-assembly of nanocages into supramolecular structures. As shown in Fig. 3.6D, in the freshly prepared nanocage solution (the molar ratio of nanocage/$NO_3^-$ is 1/24), very weak scattered intensity was recorded, indicating that initially the $M_{12}L_{24}$ nanocages exist as single cations in solution, which is also confirmed by NMR-DOSY (diffusion-ordered spectroscopy) analysis (Fig. 3.8A). The total scattered intensities recorded at 90 ° scattering angle from this nanocage solution increases slowly with time. Moreover, as shown in the inset in Fig. 3.6A, the size of the large structures (in $R_h$) stays nearly constant during the whole self-assembly process, indicating that the structures are quite stable. This observation is also consistent to our previous studies on the self-assembly of POM macroanions. Therefore, the increment of the scattered intensity with time is most likely due to an increase in the number of the assemblies in solution. Since single $M_{12}L_{24}$ nanocages are remarkably stable in DMSO and other polar solvents, the larger structures formed in the current case must be built-up from these single nanocage entities. It is also important to note that single free nanocages are always in equilibrium with the large self-assembled structures in solution, which is demonstrated by the bimodal size distribution shown in Fig. 3.6A.

Two-dimensional DOSY $^1$H NMR is a powerful technique for determining molecular size and measuring the molecular interactions via the self-diffusion coefficient.[5] In a

standard DOSY spectrum, as shown in Fig. 3.8A, the F2 domain represents the $^{1}H$ chemical shift, and the F1 domain is the diffusion coefficient corresponding to different protons. The spectrum clearly shows that immediately after synthesis, the $M_{12}L_{24}$ nanocages stay as monomers, and no large structures are observed. From the slope of the linear regression shown in Fig. 3.8B, the self-diffusion coefficient for a single nanocage is determined to be $5.45 \times 10^{-11}$ $m^2/s$, which corresponds to an average $R_h$ value of 1.8 ± 0.3 nm. As the single nanocages progressively self-assemble into larger structures in solution, as demonstrated by LLS, the proton signals originating from the nanocage species decreased with elapsing time. This can be explained by the fact that as the single nanocages start to interact with each other to form larger structures, the strong spin-spin interactions of two or more neighbouring nanocages make the transverse relaxation process so fast, that the proton peaks from those nanocages in assemblies become too broad to be detected. It is worthy to note that similar phenomenon of the proton signal decay has been reported during the vesicle formation process.[6] However, in our current system, the proton signal decay is rather slow.

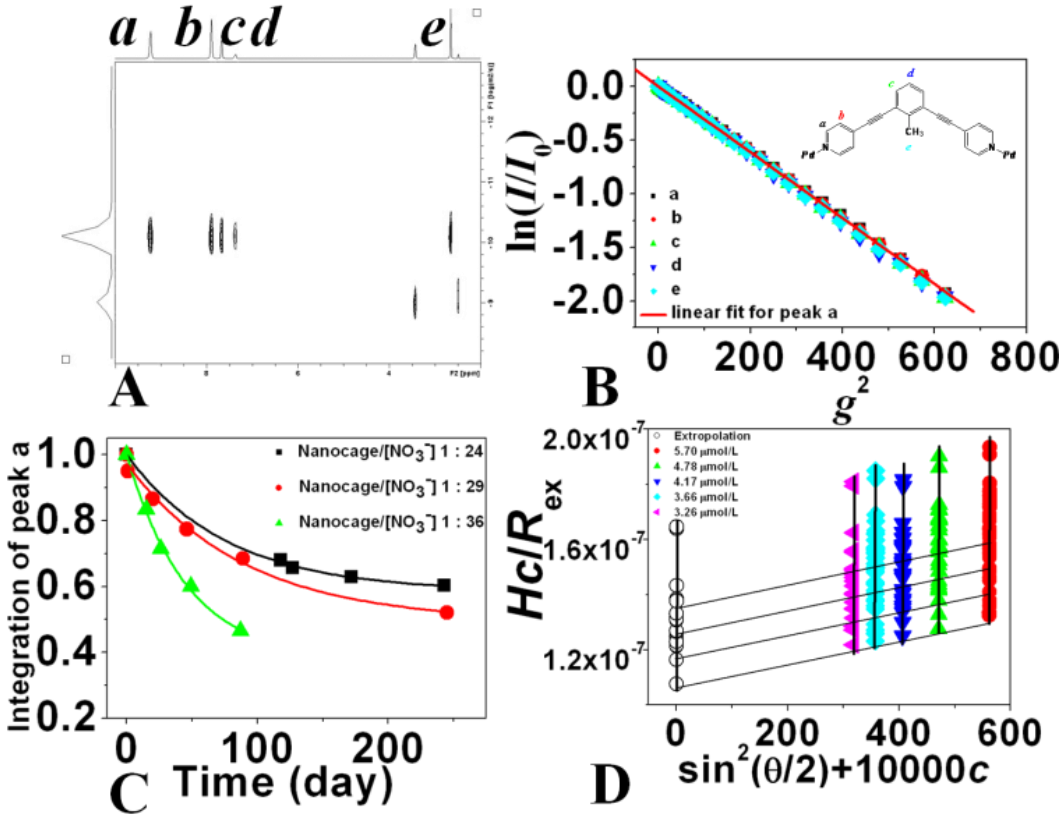


**Figure 3.8** (A) Two dimensional DOSY $^{1}$H NMR spectra of $M_{12}L_{24}$ nanocages in DMSO-*d*6, with the nanocage/$NO_3^-$ ratio of 1/24. (B) Normalized nanocage signal decay as a function of the gradient strength squared ($g^2$). The measurement was taken at 298 K immediately after synthesis of the nanocages. (C) The $^{1}$H NMR signal decay as a function of time for proton **a** of the nanocage. All data points are normalized against the initial intensity at t = 0. (D) Zimm plot of a series of diluted $M_{12}L_{24}$ nanocage samples in DMSO (a concentration amendment for large aggregates was made based upon NMR signal decay results).

Assuming that in solution nanocages only have two states in dilute solution: as free monomers and in the aggregates, the total proton signal intensity from $^1$H NMR spectra will only be from the free monomers. This assumption is reasonable because we have demonstrated earlier that the oligomers, an important intermediate stage for the assembly, have a very limited concentration.[7] Therefore, when the two states achieve equilibrium, the fraction of nanocages that form aggregates can be determined by measuring the decay of the proton signal intensity. As illustrated in Fig. 3.8C, by taking proton **a** as an example, the peak area associated with proton **a** (integrated from 9.00 ppm to 9.40 ppm) on day 0 was set as the reference value, and then relevant measurements under the same conditions (*i.e.* temperature, probe, receiver gain, number of scans, *etc.*) performed on subsequent days were compared to the reference. As shown in Fig. 3.8C, all three nanocage solutions studied show a slow but continuous decay of proton intensity (Similar trends can be obtained if using DMSO-*d*6 solvent peak as the internal reference). By fitting the data with a first-order exponential decay function, the concentration of nanocage assemblies under equilibrium conditions can be estimated. Our results show that 41.6% of the total nanocages will form large assemblies when no extra $NO_3^-$ counter-ions present.

The above information is especially valuable for calculating an important parameter: the inter-cage distance on the assembly surface, which can be used for judging the nature of the attractive interactions between cationic cages. From the Zimm plot shown in Fig. 3.8D, the weight averaged molecular weight ($M_w$) of the large structures can be calculated using the Rayleigh-Gans-Debye equation. The SLS technique favors large particles and the total scattered intensity in the current SLS measurement is almost

exclusively from the large particles. From the NMR results, an appropriate correction to the assembly concentration *c* was made, resulting a final $M_w$ value for the large structures of (9.4 ± 0.8) $\times 10^6$ g/mol, which corresponds to 956 ± 81 single nanocages when the molar ratio of nanocage/$NO_3^-$ is 1/36. Based upon all the experimental results presented above, we propose a model for this self-assembled structure in solution, which is a single-layered, hollow, spherical, vesicle-like entity with individual nanocages homogenously distributed on the surface, as illustrated in Fig. 3.9. If we assume all the nanocages are arranged with pseudo-hexagonal close packing, then the averaged centre-to-centre distance between two adjacent nanocages would be 4.7 ± 0.3 nm, indicating a very close, but non-touching, proximity of the two adjacent nanocages (the diameter of an individual nanocage is ~ 4 nm as determined by DOSY). We have demonstrated before that the distribution of counter-ions around macroions plays an important role in attracting like-charged macroions together and forming blackberry structures, The calculated inter-nanocage distance (0.7 ± 0.3 nm) confirms that the counter-ion-mediated attraction is indeed possible because there is enough space between the nanocages to accommodate the small counter-ions (here $NO_3^-$).

### 3.4.3 TEM reveals the single-layered nature of blackberries

More direct evidences for this novel vesicle-like structure can be obtained from (scanning) transmission electron microscopy ((S)TEM) imaging studies. As shown in Fig. 3.10A, the vesicle-like structures have a reasonably uniform size. Some of the vesicle-like structures were found to have shrunk and/or collapsed due to the evaporation of the solvent from within the hollow structure. However, these collapsed vesicles provide an

interesting opportunity to analyze the hollow sphere structure. As marked by the red square in Fig. 3.10A, a thin single layer structure having a lighter contrast can be seen at the edge of the broken sphere, whereas the other part of the sphere displays a considerably darker contrast level generated by overlap of the top and bottom layers of the vesicle-like structure. Besides the large vesicle-like structures, individual nanocages were also observed by TEM bright field (BF) imaging via mass-thickness contrast. Both the individual nanocages and vesicle-like structures can be better visualized with STEM high-angle annular dark-field (HAADF) imaging containing atomic number (z) contrast information. In Fig. 3.10B, the cluster of Pd atoms associated with each nanocage displays a higher intensity than the dark background of the carbon film due to the more effective electron scattering by Pd. It is also clear that the vesicle-like structure is formed by the assembly of large number of nanometre size "building blocks", *i.e.* the nanocages. It should be noted that the observed spatial arrangement of individual nanocages seen in Fig. 3.10B no longer reflects the real structural motif that would exist in the solution phase, because the vesicle-like structure has deflated and collapsed due to the evaporation of solvent from within the structure. However, it is still noticeable from the HAADF images that the individual nanocages in the vesicle-like structure are well separated, which is consistent with our SLS results.

In order to further investigate the validity of our proposed mono-layer hollow sphere model, through-focal STEM-HAADF imaging was performed. The correction of the spherical aberration on our STEM instrument allows the use of a larger probe forming aperture, which in turn results in a significant reduction in the depth-of-focus of the images.[8] By systematically changing the focus setting of the microscope lenses, it is now

possible to obtain a series of images that are focused at different depth levels in the sample along the incident electron beam direction. The HAADF images shown in Fig. 3.10C and 3.10D were obtained from the general same area of a broken edge of a vesicle-like structure at different focus settings. The red rectangles in Fig. 3.10C indicate the identical area of the sample. It is clear that by changing the focus value, different parts of the image go in and out of focus. In fact, all the Pd clusters from the nanocages shown in Fig. 3.10C and 3.10D can be sorted into two different focus levels as indicated by the two different color circles, which further confirms our structure model since a vesicle wall comprised of a single layer of nanocages can be expected to collapse on a flat substrate to give a bilayer of nanocages. And to our knowledge, this is the first time people can reveal the true "face" of the blackberry-type structure.

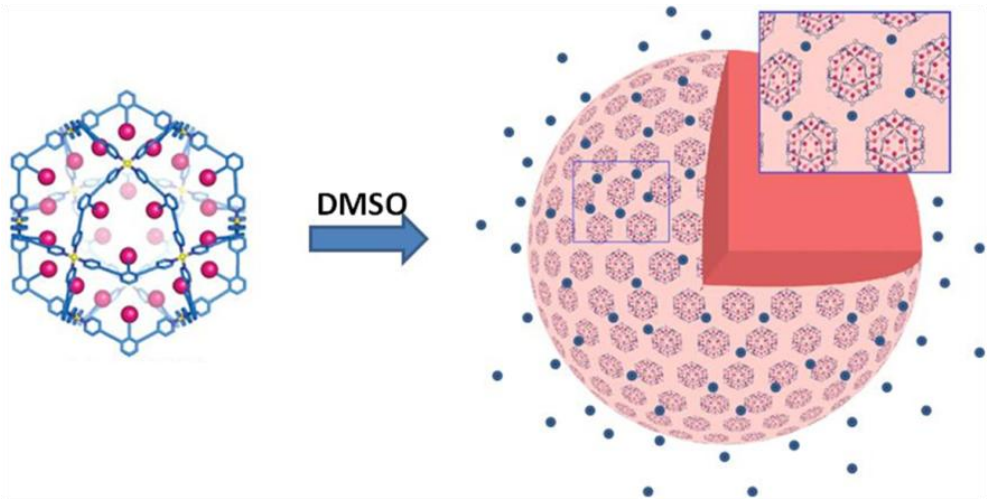


**Figure 3.9** A cartoon illustrates the self-assembly process of $M_{12}L_{24}$ nanocages in DMSO solutions (blue dots are $NO_3^-$ counter-ions).

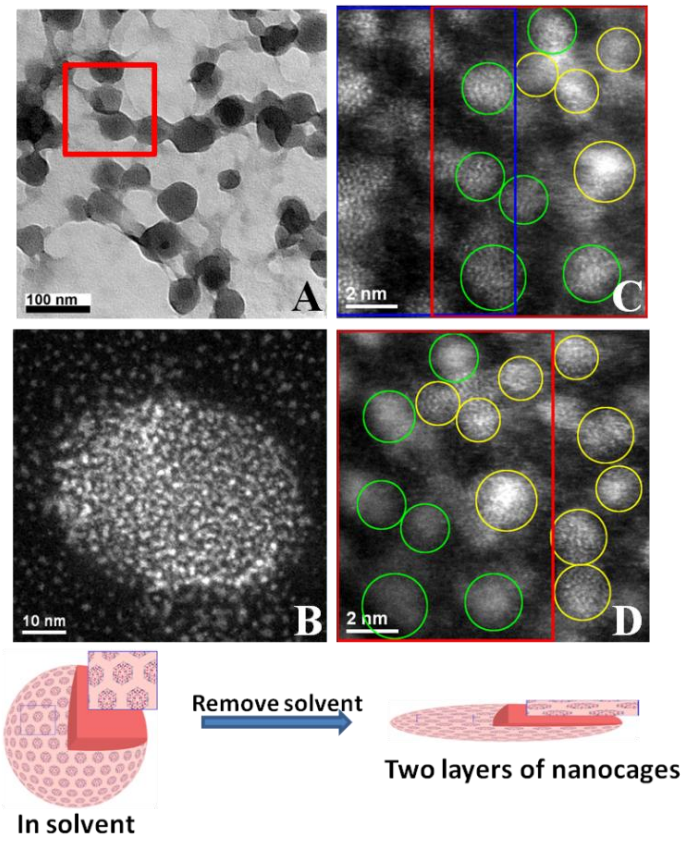


**Figure 3.10** TEM and STEM images of collapsed vesicle-like structures and individual nanocages dispersed on a carbon support film. (A), Low magnification BF images; (B) STEM-HAADF image of one typical collapsed vesicle-like structure which is surrounded by an atmosphere of individual nanocages. STEM-HAADF images obtained from a broken edge of a vesicle-like structure at two different focus settings, with (C) focussed on the bottom layer, and (D) focussed on the top layer. For comparative purposes the red rectangles in the images indicate the exact same area of the sample. The green circles highlight the Pd clusters in the bottom layer, while the yellow ones indicate the clusters in the top layer. The blue rectangle indicates the broken edge of the vesicle-like structure where the top layer is gone.

### 3.4.4 Effect of counterion concentration on blackberry size

To examine the counter-ion effect on the self-assembly of the nanocages, extra $Pd(NO_3)_2$ solutions were introduced to a couple of freshly prepared nanocage solutions to give the final molar ratios of nanocage/$NO_3^-$ as 1/29 and 1/36. When a different amount of additional $NO_3^-$ counter-ions was introduced, initially, the individual nanocage size didn't show any obvious difference based upon DOSY results. As illustrated in Fig. 3.6D, when no additional $NO_3^-$ is present in the solution (*i.e.*, no additional counter-anions, the molar ratio of nanocage/$NO_3^-$ is 1/24), the increase of the scattered light intensity with time is much slower as compared with the other two solutions, and a significant lag period (~30 days) exists before the scattered intensity starts to significantly increase. Furthermore, the kinetic curves for all three samples are sigmoidal, indicating a nucleation step followed by a rapid self-association process. As the concentration of $NO_3^-$ ions increases, the lag period for the self-assembly process to initiate becomes much shorter. Such types of kinetic curves are readily seen in many viral capsid formation processes and also some polyoxometalates solutions.[7,9] These observations, taken together with the fact that larger self-assembled structures are formed at higher $NO_3^-$ concentrations (Fig.3.6B and 3.6C), indicate that the additional counter-anions ($NO_3^-$) play an important role in the self-assembly process of nanocages, most likely by lowering the activation energy barrier between individual nanocage macrocations and the self-assembled structures. More importantly, when extra $NO_3^-$ counter-ions are added into nanocage solutions, the proton signal decays much faster (Fig. 3.8C) and the total intensity loss is also more significant (this value increases to 50.8% and 62.6%

respectively when the nanocage/$NO_3^-$ ratios are 1/29 and 1/36), indicating that the presence of additional $NO_3^-$ counter-ions favors the formation of assemblies.

### 3.4.5 Effect of solvent polarity on blackberry size

As noted above, when additional $NO_3^-$ counter-ions are present in solution, *i.e.* the ionic strength of the solvent increases, significantly more nanocages will self-assemble into vesicle-like structures and the overall size of the vesicle-like structures will also increase. Moreover, when a less polar solvent such as acetonitrile was introduced into the freshly prepared nanocage solutions (the $CH_3CN$ content varies from 20 - 80 vol%), we noticed that the self-assembly process of the nanocages accelerated. And when the self-assembly approached to equilibrium, we found that the size of the vesicle-like structures displays a linear relationship with the inverse dielectric constant of the solvent, suggesting that the their size could be determined by their renormalized charge density, as shown in Fig. 3.11.[10] These results all indicate that the counter-ions play an important role in this interesting self-assembly process, which is analogous to the case for POM macroanions. The effective surface charge density of the macroanions is significantly lowered due to the counter-ion association, which in turn reduces the repulsion force between two macroanions. In the cationic $M_{12}L_{24}$ solution, we believe that counter-ion mediated attraction is the major driving force for the self-assembly. Since each nanocage contains a large portion of aromatic organic ligands, hydrophobic interactions and/or $\pi$-$\pi$ stacking interactions of the organic-ligand entities may also provide additional stabilization to the vesicle-like blackberry structure once it forms. Comparing with purely hydrophilic POM clusters which have similar surface charge density to the $M_{12}L_{24}$

nanocages, the blackberries formed by the POM clusters have an average, roughly estimated interparticle distance of ~ 1.0 nm, but the vesicle-like structures formed by $M_{12}L_{24}$ nanocages show a smaller interparticle distance (~ 0.7 nm), indicating an additional contribution from other attractive forces, most likely from hydrophobic interactions. A possible scenario is that the existence of the hydrophobic interaction leads to some very close contacts between the nanocages, which shorten the average inter-cage distance obtained from SLS measurements. Such a distance still allows the counter-ions to get involved in the assembly process.

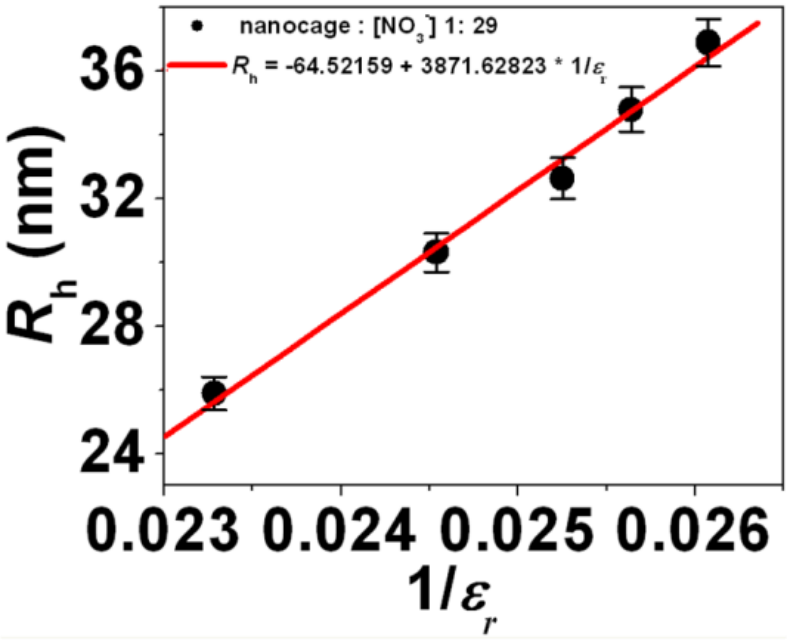


**Figure 3.11** The average $R_h$ of the vesicle-like structures in $M_{12}L_{24}$ nanocage DMSO solutions containing different volumes (40 - 80 vol%) of $CH_3CN$ is plotted against the inverse dielectric constant ($\varepsilon_r$) of the solvent.

### 3.4.6 Similarity between blackberries and viral capsids

The co-existence of the electrostatic interaction and hydrophobic interaction makes the self-assembly process of the nanocages remarkably similar that of to some biological processes, such as viral capsid formation. Similar to the viral capsids, the vesicle-like structures self-assembled from nanocages are also mono-layer spheres with individual nanocages evenly distributed in the wall of the vesicle-like structures. It has also been noticed that the viral capsid formation process can be accelerated under high salt concentration. In the case of nanocages, the presence of additional salts will also speed up the self-assembly process and induce the formation of larger vesicle-like structures. However, for single nanocages to self-assemble into blackberry structures, it normally requires days or even months to achieve equilibrium; in contrast, for viral capsid formation, the time frame for formation is of the order of hours or several days. A possible reason for this time-scale difference could be due to the specific interaction sites and geometrical restrictions of the viral capsid dimers, which are missing for our cuboctahedral nanocages. In other words, the degree of freedom of individual nanocages on the vesicle-like structure surface is larger than that for protein dimers. The different surface charge density of nanocages and protein dimers may also be an important factor. In addition, the viral capsid is a dynamic structure in the sense that its size can vary reversibly in response to different environmental stimulus (*i.e.* pH, ionic strength, temperature) by tuning the dimer-dimer distance and the capsid protein structure.[11-14] This breathing or swelling mode is quite important in the life cycle of a virus, not only for maintaining the structural integrity of the virus but also for influencing the virus-host

interaction and the release of the packaged nucleic acid. In the current case, the vesicle-like structures formed by nanocages can also "sense" the change of surrounding conditions (*i.e.* ionic strength and solvent polarity) and subsequently change their size. These interesting properties of the vesicle-like structures formed by nanocages suggest that a "charge effect" plays an important role in the macro-ion self-assembly process as well as in viral capsids formation and stability.

## 3.5 Conclusions

In summary, we demonstrate for the first time that cationic metal-organic nanocages can self-assemble into unique supramolecular blackberry type structures in solution. The vesicle size can be accurately adjusted by varying the solution polarity and/or counterion concentration. The counter-ion mediated interactions between nanocages are likely the major driving force for the assembly, while hydrophobic interactions and/or π-π stacking interactions of the organic-ligand entities may also contribute to the supramolecular structure. This vesicular structure indicates the self-assembly process is a universal phenomenon for macroions in dilute solution: they also tend to strongly attract with each other and form conserved, stable supramolecular structures with the help of counterions. More importantly, the self-assembly process of nanocages shares some remarkable similarities with viral capsid formation. Indeed it may be feasible to use them as a model system to mimic viral capsids, possibly leading to a more fundamental understanding of protein-protein interactions. Also, the self-assembled nanocages can provide blackberry structures a wide range of organic functionalities that are impossible to reach with purely inorganic systems, which may open the door to new types of biomembranes, hierarchically structured delivery systems, nanocontainers, nanoreactors, sensors, and nanocatalysts.

## References


(1) Fujita, M.; Oguro, D.; Miyazawa, M.; Oka, H.; Yamaguchi, K.; Ogura, K. *Nature* **1995**, *378*, 469.

(2) Tominaga, M.; Suzuki, K.; Murase, T.; Fujita, M. *J. Am. Chem. Soc.* **2005**, *127*, 11950.

(3) Provencher; W., S. *Comput. Phys. Commun.* **1982**, *27*, 229.

(4) Liu, T.; Diemann, E.; Li, H.; Dress, A. W. M.; Muller, A. *Nature* **2003**, *426*, 59.

(5) Cohen, Y.; Avram, L.; Frish, L. *Angew. Chem. Int. Ed.* **2005**, *44*, 520.

(6) Rodr ́guez-Hern ández, J.; Lecommandoux, S. *J. Am. Chem. Soc.* **2005**, *127*, 2026.

(7) Zhang, J.; Li, D.; Liu, G.; Glover, K. J.; Liu, T. *J. Am. Chem. Soc.* **2009**, *131*, 15152.

(8) Lupini, A. R.; Borisevich, A. Y.; Idrobo, J. C.; Christen, H. M.; Biegalski, M.; Pennycook, S. J. *Microsc. Microanal.* **2009**, *15*, 441.

(9) Ceres, P.; Zlotnick, A. *Biochemistry* **2002**, *41*, 11525.

(10) Verhoeff, A. A.; Kistler, M. L.; Bhatt, A.; Pigga, J.; Groenewold, J.; Klokkenburg, M.; Veen, S.; Roy, S.; Liu, T.; Kegel, W. K. *Phys. Rev. Lett.* **2007**, *99*, 066104.

(11) Bancroft, J. B.; Hills, G. J.; Markham., R. *Virology* **1967**, *31*, 354.

(12) Ehrlich, L. S.; Liu, T.; Scarlata, S.; Chu, B.; Carter, C. A. *Biophys. J.* **2001**, *81*, 586.

(13) Jacrot, B. *J. Mol. Biol.* **1975**, *95*, 433.

(14) Vriend, G.; Hemminga, M. A.; Verduin, B. J. M.; Schaafsma., T. J. *FEBS Lett.* **1982**, *146*, 319.

# Chapter 4: Self-assembly of Functionalized Macroions in Solution

## 4.1 Introduction

In this chapter, a novel group of functionalized macroions: inorganic-organic hybrid macroions, *i.e.* chemically grafting organic ligands to hydrophilic POMs will be discussed. Such inorganic-organic molecular hybrids are expected to render amphiphilic properties to the POMs and consequently improve their applications by expanding their compatibility in organic media, a challenging but also highly rewarding strategy. Furthermore, these organic ligands can also be applied to adjust some important features of POMs, including electronic and luminescent properties. Exploring the amphiphilic nature of such hybrids and understanding their self-assembly behaviour in solution and at interface would be important initial steps for scientists.

Amphiphilic molecules which are ubiquitous in nature normally combine hydrophilic and hydrophobic components together into one structure. Such arrangement gives them the ability to interact with two different phases and self-organize into highly ordered structures. We are interested in, from colloidal chemists' point of view, exploring the amphiphilic nature of the hybrid POMs and their nano-scaled assemblies.

## 4.2 Synthesis of amphiphilic hybrid POMs.

The majority of inorganic-organic hybrid POMs can be classified into two groups, the hybrids with weak interactions (e.g. electrostatic interactions, hydrogen bonding, or van der Waals interactions etc.) and the hybrids with strong interactions (e.g. covalent bonds) between the inorganic and organic components.[1] In this chapter, we will mostly focus on the second scenario.

### 4.2.1 Amphiphilic hybrid POMs with non-covalent bonds

For the first group, hydrophilic POM macroions interact with organic cations or cationic surfactants mainly through electrostatic interactions to construct inorganic-organic amphiphilic hybrids. One example is the surfactant encapsulated POM clusters (SECs).[2] These clusters normally consist of a core-shell structure having hydrophilic POMs in the centre surrounded by hydrophobic functional groups.[3-6] The surface properties of POMs may still be retained according to a recent study of $Li^+$ uptake and release process from SECs.[7] Similar synthetic approach can be extended to fabricate POM/polymer hybrids.[8,9] Mizuno's group has reported a group of organic macrocations/POM ionic crystals.[10-12] Owing to the hydrophilic and hydrophobic channels inside these ionic crystals, they demonstrated exceptional adsorption and catalytic properties. Cronin *et al*. showed that some protonated bulky organic amines can not only serve as counter-cations but also influence the final POM structure by limiting the reorganization rate of different POM isomers in solution.[13] More details regarding these hybrids formed by non-chemical bonds can be found in corresponding early reviews.[14,15]

### 4.2.2 Amphiphilic POMs with covalent bonds

The covalently modified amphiphilic hybrid POMs are attractive because: 1. the terminal and bridging oxygen atoms are relatively reactive and can be replaced by other atoms or form direct M-O-R bonds; 2. some POM clusters possess multiple sites available for functionalization, which can be done by linking one or more hydrophobic organic functional groups to one POM; 3. the amphiphilic nature of these hybrids extends the functionality of POM clusters in organic media; 4. amphiphilic hybrid POMs can probably be used as multifunctional oxidation or acidification catalysts with good selective recognition of substrates. Although there are many different synthetic pathways to covalently link organic functional groups with POMs, we will only focus on several facile preparation methods (some commonly used synthetic strategies are summarized in Fig. 4.1). More details regarding the synthesis of hybrid POMs can be found in another well-written review.[1]

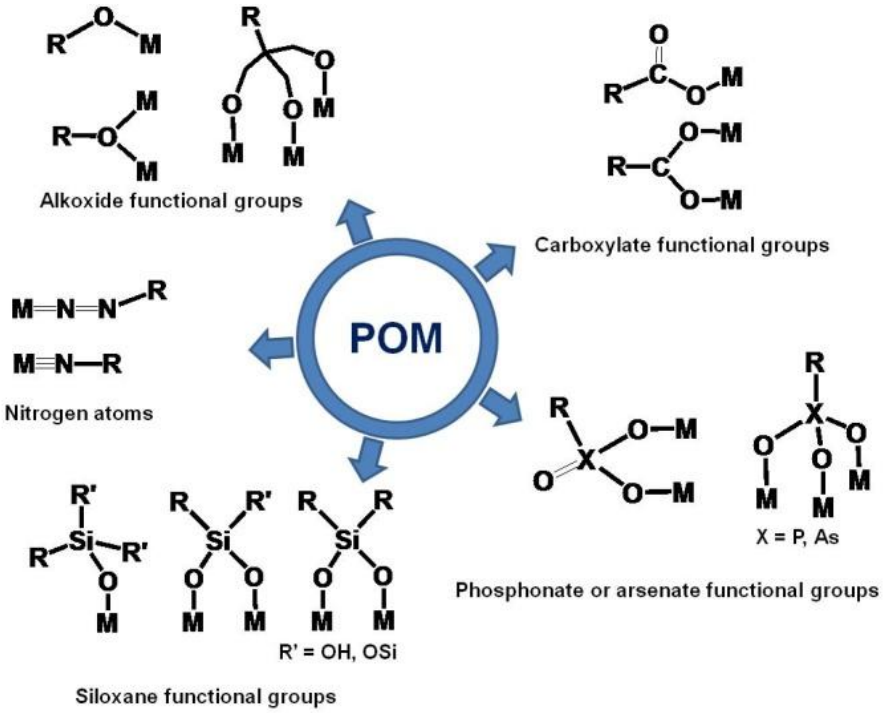


**Figure 4.1** Several commonly applied synthetic strategies to covalently link organic groups to the POM units.

### 4.2.2.1 Organoimido derivatives of POMs

Since Zubieta's group reported the first example,[16] the organoimido derivatives of POM have been extensively investigated and a number of organoimido derivatives of the Lindqvist hexamolybdate ion, $[Mo_6O_{19}]^{2-}$, have been reported.[17] The hexamolybdate ion $[Mo_6O_{19}]^{2-}$ is a chemical robust cluster with good thermal stability. The terminal oxygen atoms are reactive enough to be directly replaced by various nitrogenous species, for instance, diazenido, diazoalkyl, and imido groups. The six terminal oxo groups and some bridging –oxo groups in the hexamolybdate cluster can be partially or completely substituted with organoimido ligands, as shown in Fig. 4.2. Recently, a large number of monosubstituted, disubstituted and polysubstituted organoimido derivatives of

hexamolybdate have been synthesized and structurally characterized. Also, the synthesis of such clusters can be dramatically improved in the presence of dicyclohexylcarbodiimide (DCC). Since the $\pi$ electrons in the organic component may extend their conjugation to the inorganic framework and dramatically modify the electronic structure and redox properties of the corresponding POMs, exciting synergistic effects due to the close interaction of delocalized organic p-$\pi$ orbits with the POM cluster's d-$\pi$ orbits are expected for the POM organoimido derivatives with aromatic functional groups. The multi-stage redox properties of these POMs and the possibility of generating mixed-valence electronic structures make them attractive building blocks for the development and design of new electrical and magnetic nano-scale materials.

**4.2.2.2 Tris-Anderson hybrid POMs**

Another strategy to covalently modify POMs is through the use of a "tris" (tris(hydroxymethyl)aminomethane) linker with three pendant hydroxyl groups. It is an one-pot reaction of [$\alpha$-$Mo_8O_{26}$]$^{4-}$ precursor, $M(acac)_3$ (M = $Mn^{III}$, $Fe^{III}$) or $M(OAc)_2$ (M = $Zn^{II}$, $Ni^{II}$) and tris derivatives in acetonitrile under refluxing conditions. The trisalkoxo ligand with a secondary functional group can be further modified through an imination or amidation reaction. As the result, a variety of tripods that allow further functionalization through imine and peptide bonds are generated, as shown in Fig. 4.3.[18] Only recently, the unsymmetrical tris-Anderson hybrid POMs with two different functional groups attached to the same central POM was achieved by Cronin's group.[19,20] Not only limited to the Anderson POMs, amphiphilic hybrid Lindqvist and Dawson POMs capped with tris functional groups have also been synthesized. Zubieta *et al*. synthesized a series of hybrid polyoxovanadate $[V_6O_{13}H_x\{(OCH_2)_3CR\}_2]^{n-}$ ($x$,$n$ = 0,2; 2,0; 4,2; 6,2; R = $NO_2$, $CH_2OH$,

$CH_3$) with trisalkoxo $\mu$-bridging tripodal ligands.[21] Hill and co-workers developed a way to functionalize Dawson type POMs with tris ligand.[22] These state-of-art synthetic tools could provide numerous hybrid POMs with great potential as multi-functional materials.

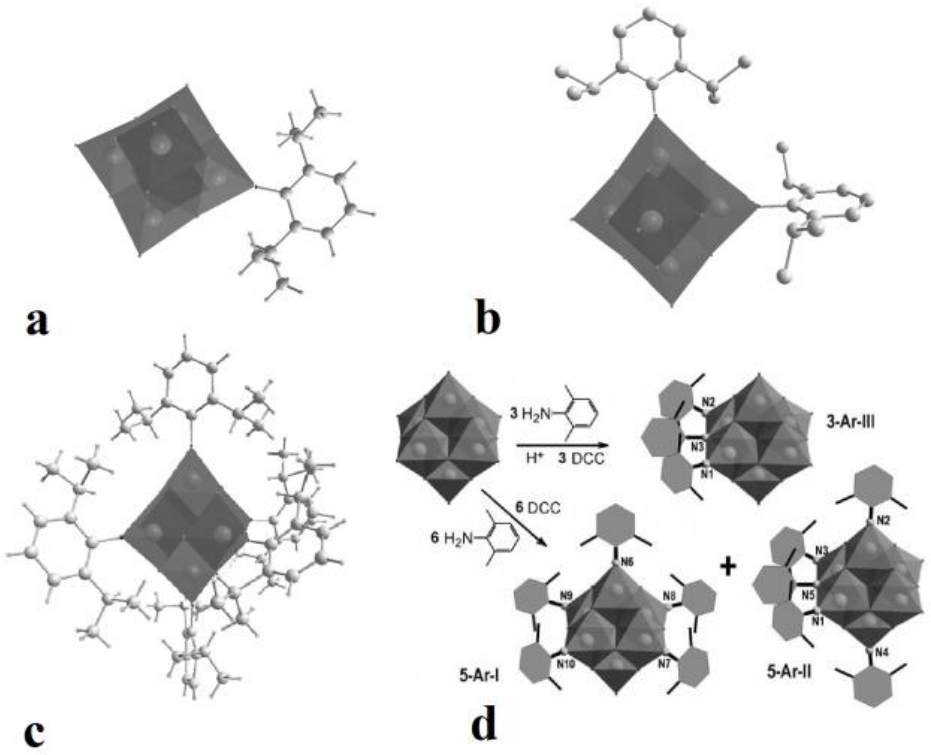


**Figure 4.2** Covalently modified Lindqvist type POMs through the formation of organoimido bond at terminal and/or bridging oxygen atoms. (a) Mono-substituted, (b) di-substituted and (c) hexa-substituted Lindqvist POMs through terminal oxygen. (d) Covalent modification of Lindqvist POMs through bridging oxygen. (Copyright 1992, 2000 American Chemical Society. 2008 John Wiley and sons)

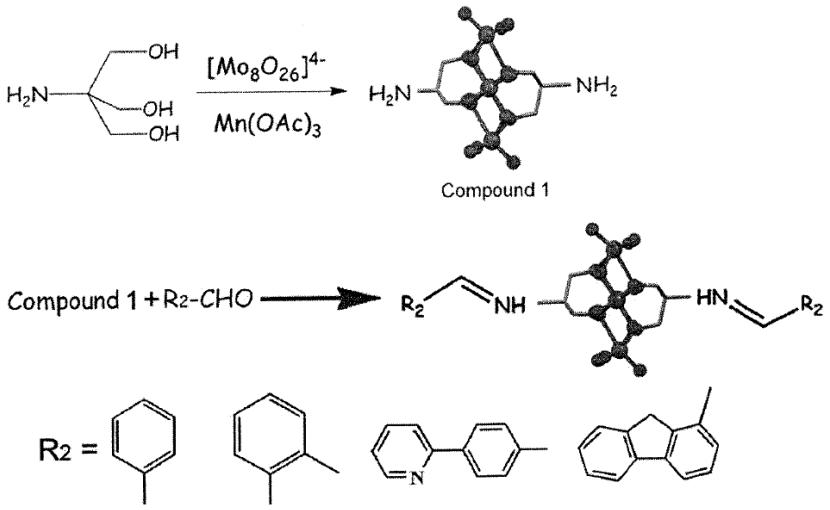


**Figure 4.3** The formation of Tris-Anderson hybrid POMs with different organic functional groups. (Copyright 2010 the Royal Society of Chemistry)

#### 4.2.2.3 POM-modified polymers

In those hybrids, the POM clusters could serve as functional groups on side-chains or directly get involved in main polymer chains. The first covalently bonded POM–polymer hybrid was reported by Judeinstein in which a lacunary Keggin cluster was linked to a polystyrene or polymethacrylate backbone through the formation of Si-O bonds.[23] Later, Maatta *et al*. reported a polymer–POM hybrid synthesized via free radical-copolymerization. Peng and co-workers have recently incorporated hexamolybdate clusters into poly(phenylene ethynylene) as side-chain pendants through the Pd-catalyzed coupling reactions.[24] Fluorescence studies demonstrated that polymers with conjugated POMs exhibited considerably higher fluorescence quenching effect than those without conjugated POMs, indicating that the photo-induced electron transfer is more effective through conjugated bridges. Using the same approach, main-chain-hexamolybdate-

containing hybrid polymers were also achieved by this group.

## 4.3 POMs based supramolecular Assemblies

### 4.3.1 One dimensional (1D) assemblies

1D nanostructures with low dimensionality and high aspect ratio possess unique optical and photoelectronic properties. These materials can be incorporated in future electronic and photonic devices such as photodetectors, light emitting diodes (LEDs), and field effect transistors (FET).

One strategy to construct 1D supramolecular assembly takes advantage of self-assembly through weak interactions (hydrogen bonding, van der Waals interactions, hydrophobic interactions, and π-π stacking interactions). A typical example is the 1D nanofibrils self-organized at the solvent-air interface, which is reported by Cronin's group (Fig. 4.4).[20] Three different Anderson POM based hybrids can self-assemble into single-layered, long nanofibrils with the length of several microns and they are stacked together through multiple weak interactions.

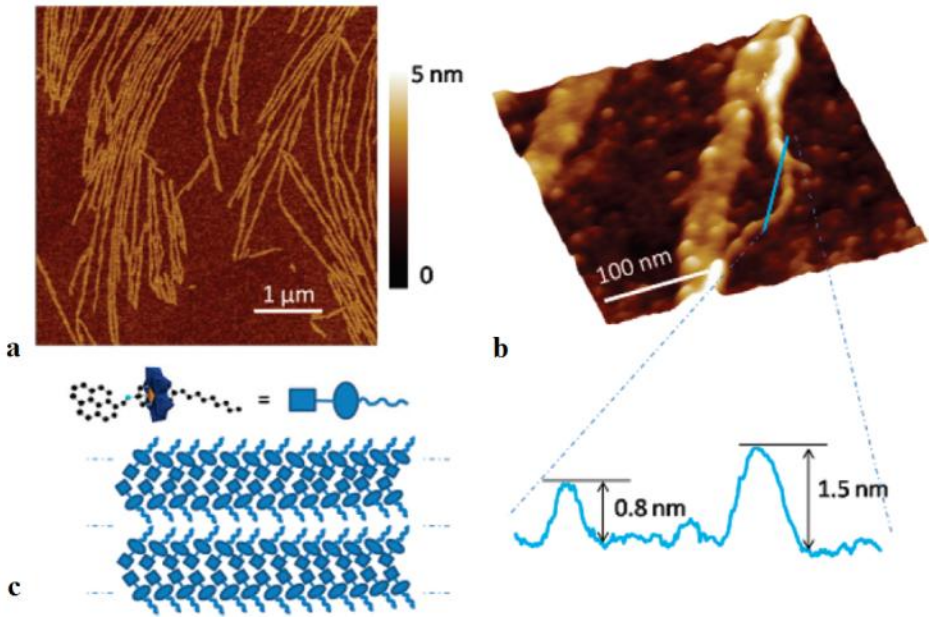


**Figure 4.4** Self-assembled monolayer of amphiphilic hybrid Anderson POMs on Si-OH. (a) and (b) SFM images; (c) a cartoon showing the proposed hierarchical arrangement of hybrid POMs in the nanofibrils through multiply weak interactions. (Copyright 2010 American Chemical Society)

### 4.3.2 Thin films formed by amphiphilic hybrid POMs

Thin films are important for photoluminescent sensors, electrochromic devices and catalysis. However, POMs alone lack the ability to form stable films; therefore a special film-forming matrix such as surfactants or polymers is needed. Chambers and co-workers reported the synthesis of the first bis(alkyl) substituted, amphiphilic, asymmetrical POM species, a bis(dodecyl) derivative $\{[CH_3(CH_2)_3]_4N\}_4\{[CH_3(CH_2)_{11}Si]_2OSiW_{11}O_{39}\}$. It reversibly forms stable Langmuir-Blodgett (LB) monolayer at the air–water interface.[25] The stability of the LB film depended largely on the organosilyl groups rather than the bulky counter-cations of tetrabutylammonium ($TBA^+$). Our recent studies on a group of

novel POM-(organic linker)-POM dumbbell type amphiphilic hybrids also show the formation of LB films at the air-water interface with $TBA^+$ as counter-cations.[26] These nano-dumbbells are hydrophilic on both ends, and the middle linker part is hydrophobic, as shown in Fig. 4.5. The air/water interfacial behaviors, obtained from the π-A isotherms, for hybrids with linear alkyl chain linkers are relatively similar. However, hybrids with bipyridine and ether linkers present a different air/water behavior. Liquid expanded and liquid condensed phases are clearly located and connected through a plateau. We believe that the hydrophobicity and composition of the organic linkers play dominant roles.

Self-assembled monolayers (SAMs) represent an attractive approach to anchor hybrid POMs to the surface, which exhibits a high degree of structural order, and can be patterned easily. Therefore, it allows a better control of the assembled structures. Cronin's group reported an interesting self-assembled monolayer of hybrid POMs on gold surface which shows cell adhesion properties.[27] As shown in Fig. 4.6, a monolayer of 16-mercaptohexadecanoic acid (MHA) moieties was stamped on gold surface, which was further covalently coupled with Mn-Anderson POMs via N3-(dimethylaminopropyl)-N′-ethylcarbodiimide hydrochloride (EDC)/N-hydroxysuccinimide (NHS). Finally, different functional groups, such as pyrene, were grafted onto the POMs. The human fibroblasts have high affinity to the pyrene platform, and the central POMs are essential to the cell adhesion performance. Similar strategies can be found in Errington's and Tour's papers.[28,29]

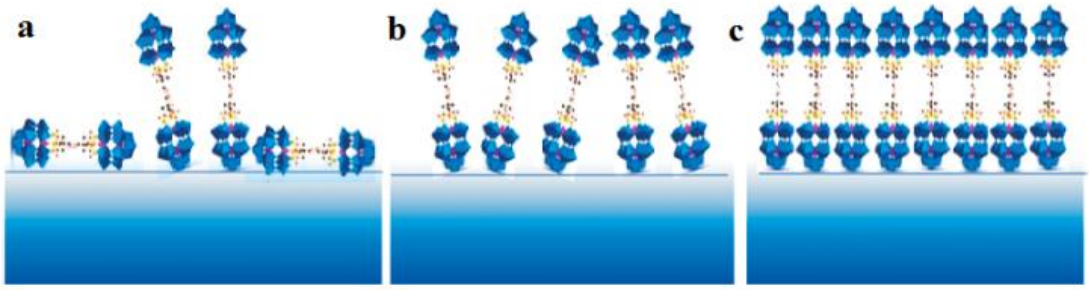


**Figure 4.5** Monolayer formation for the dumbbell-shaped hybrid surfactants at the water/vapor interface: (a) Liquid expansion (LE)/G phase, (b) LE phase, and (c) Liquid condense (LC) phase. $TBA^+$ counter-cations are not shown. (Copyright 2011 American Chemical Society)

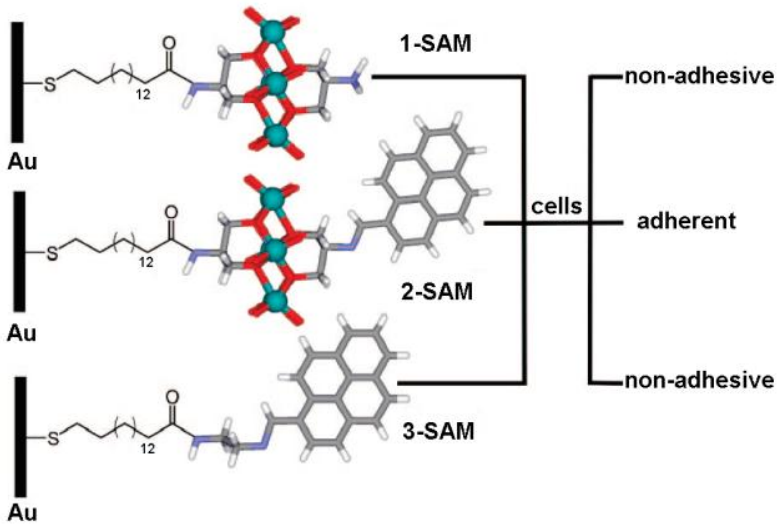


**Figure 4.6** The structures of self-assembled monolayers of Mn-Anderson POM/pyrene complexes on gold surface with selective cell adhesion properties. Self-assembled monolayers contain only POMs or pyrene has no cell adhesion properties. (Copyright 2009 American Chemical Society)

### 4.3.3 Supramolecular assemblies formed in solution

In solution the POM-organic hybrids can be treated as ionic surfactants with large polar head groups (the POMs). Amphiphilic surfactants can interact with two immiscible solvent phases and lower the interfacial tension, and self-organized into supramolecular architectures when their concentration is above the critical association concentration (CAC). Sulfate, sulfonate, phosphate, carboxylate and ammonium are common head groups for regular ionic surfactants, which are much smaller than the POMs. Consequently, POM-based surfactants could greatly change the surfactant packing parameter $N_s$, which is widely applied to explain and predict the self-assembly behavior of a surfactant through the relationship $N_s = V_c/(L_c A_0) \approx A_c/A_0$ , in which $V_c$ is the volume of the hydrocarbon tail, $L_c$ is the length of the hydrocarbon tail, and $A_0$ is the area per head group.[30] When $N_s$ is small (< 0.37), spherical micelles are expected to form in solution; when $N_s$ is close to 0.5, cylinder micelles become the favourable assemblies; when $N_s$ approaches 1, lamella phase or vesicles should be observed. If $N_s$ is larger than 1, reverse vesicles or micelles are two possible structures (as illustrated in Fig. 4.7). Therefore, fundamentally it is important to study how the giant POM affects the surfactant packing parameter. Moreover, by tethering different organic functional groups to the hydrocarbon tails, the POM-based hybrid surfactants could show better bio-compatibility, better catalytic performance and stronger sorption ability in different systems.

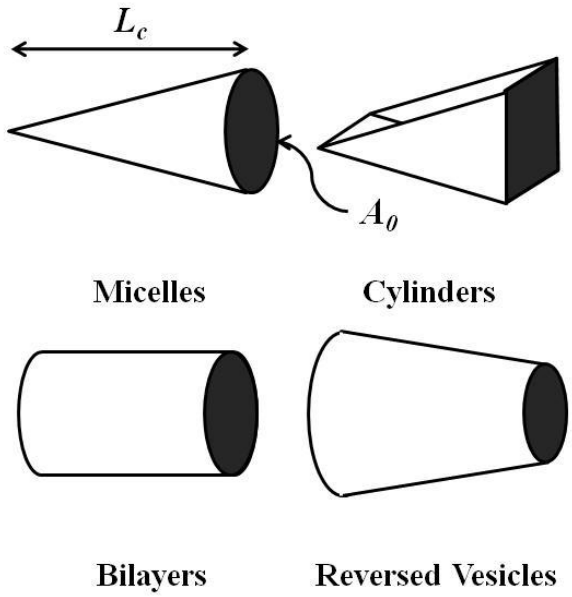


**Figure 4.7** Illustration of how different geometries of surfactant molecules will lead to various supramolecular assemblies.

## 4.4 Solution behaviors of polyoxovanadate-pyrene hybrid macroions

### 4.4.1 Methods

#### 4.4.1.1 X-ray crystallography.

X-ray quality crystals of $[V_6O_{13}\{(OCH_2)CNH_3\}]2.4DMSO(NH_3V_6)$, $[(n\text{-}C_4H_9)_4N]_2[V_6O_{13}\{(OCH_2)_3CNH_2\}_2]$ ($TBANH_2V_6$), and $(TBA^+)_2$**2** were coated with Paratone N oil and mounted on a small fiber loop for index and intensity data collection. The X-ray diffraction data were collected under a nitrogen stream at 173 K on a Bruker D8 SMART APEX CCD single-crystal diffractometer with graphite monochromated Mo KR ($\lambda$ = 0.71073 Å) radiation. Data collection, indexing, and initial cell refinements were processed using the SMART43 software while frame integration and final cell

refinements were carried out using the SAINT44 software. The final cell parameters were determined from the least-squares refinement of total reflections. The structures were determined through direct methods (SHELXS97) and difference Fourier maps (SHELXL97). The Cambridge Crystallographic Data Centre deposition number for $NH_3V_6$, $TBANH_2V_6$, and $(TBA+)_2$**2** are CCDC 821763, 821764, and 821765, respectively.

#### 4.4.1.2 Cation exchange

Counterion replacement of $TBA^+$ with $H^+$ was achieved by using a cation-exchange resin column. For a typical experiment, 5 mg of hybrid cluster **1** or **2** was dissolved in 2 mL of acetonitrile. This solution was then applied to a pre-packed, cation-exchange resin column (Amberjet 1200 hydrogen form purchased from Sigma-Aldrich) rinsed with D.I. water and acetonitrile. An additional 20 ~ 50 mL of acetonitrile was used to elute the column, and the yellow fraction was collected. The post elution was further washed with 5mL of diethyl ether to remove organic impurities. The final solution was transferred into a glass culture plate and kept in the dark for several days to fully evaporate the solvent. Yellow colored fine powders were collected and could be easily dissolved in water or DMSO for further study.

#### 4.4.1.3 Laser light scattering

Both dynamic light scattering (DLS) and static light scatting (SLS) techniques were used to characterize the self-assembly of hybrids in solution. A Brookhaven Instruments Inc. light scattering spectrometer, equipped with a diode-pumped solid-state (DPSS) laser operating at 532 nm and a BI-9000AT multichannel digital correlator was used for all

experiments. The SLS was performed over a broad range of scattering angles from 30 degree to 130 degree, with a 2 degree interval. The radius of gyration ($R_g$) and the weight-average molecular mass ($M_w$) of the large assemblies were calculated using the Rayleigh-Gans-Debye equation as shown in chapter 3 For DLS measurements, the intensity-intensity time correlation functions were analyzed by the constrained regularized (CONTIN) method in order to ascertain the average hydrodynamic radius ($R_h$) of the large assemblies. The average apparent translational diffusion coefficient, Dapp, was determined from the normalized distribution function of the characteristic line width, $\Gamma$(G). The hydrodynamic radius $R_h$ is converted from D through the Stokes-Einstein equation. The particle size distribution in solution can be obtained by plotting $\Gamma$G($\Gamma$) versus $R_h$, with $\Gamma$iGi($\Gamma$i) being proportional to the angular-dependent scattered intensity of particle i having an apparent hydrodynamic radius $R_{h,i}$. The temperature in the sample chamber was controlled to within $\pm 0.1^{\circ}$C. More details about SLS and DLS can be found in our previous publications.

**4.4.1.4 Transmission electron microscopy (TEM).**

Samples for electron microscopy characterization were prepared by pipeting 5 $\mu$L of diluted solution onto a carbon-coated TEM grid. The TEM samples were left under ambient conditions for several hours until the solvent completely evaporated. Bright-field (BF) TEM imaging was performed on a JEOL 2000FX transmission electron microscope having an accelerating voltage of 200 kV.

#### 4.4.1.5 Zeta (ζ) potential analysis.

All the ζ potential analysis measurements were performed on a Brookhaven Instrument Inc. Zeta PALS Analyzer. The instrument is equipped with a red laser operating at 660 nm wavelength and has an accuracy of (2% for filtrated samples. The sample chamber was kept at 25 ± 0.1˚C, and all sample solutions were loaded 30 min prior to measurements in order to achieve thermal equilibrium with the chamber. Nuclear

#### 4.4.1.6 Magnetic resonance spectroscopy (NMR)

All 1D and 2D 1H NMR measurements in the liquid state were performed on a Bruker Avance 500 spectrometer equipped with a 5 mm triple-axis gradient (TXI) probe. 2D nuclear Overhauser enhancement spectroscopy (2D NOESY) spectra were recorded with 256 t1 increments and 64 scans under the pulse program of noesygpph 19 provided with Topspin 1.3. The relaxation delay D1 varied from 1 to 2 s, and the mixing time D8 changed from 0.1 to 0.5 s. Baseline correction and noise reduction were performed when appropriate. All spectra were taken at room temperature, and FIDs were processed and analyzed with the NMR software provided by Bruker.

#### 4.4.1.7 Fluorescence measurements

Fluorescence spectra were recorded at room temperature on a Cary Eclipse fluorescence spectrophotometer. The excitation wavelength, $\lambda_{exc}$, used was 335 nm, and the spectrum width was from 350 to 700 nm. An emission filter of 360-1100 nm was used. Each spectrum was obtained by averaging three scans and corrected for scatter of the equivalent blank sample. In calculations of the excimer-to-monomer intensity ratio, the monomer (IM) and the excimer (IE) were determined by taking the integrals under

the fluorescence peaks from 350 to 430 nm for the pyrene monomer and from 430 to 700 nm for the pyrene excimer.

### 4.4.2 Results and discussion

Applying fluorescent probes to investigate biochemical microenvironments is a powerful technique that can often provide unique and critical information. Pyrene, a highly symmetrical polyaromatic hydrocarbon fluorophore possessing restricted modes of motion, can exhibit fine structure in its absorbance and fluorescence spectra at room temperature.[31] One important application of the pyrene fluorescence stems from its ability to probe the polarity of the local microenvironment, either in a hydrophobic or hydrophilic media, from the change of specific emission peaks in the spectrum.[32,33] Therefore, amphiphilic hybrid POM clusters with pendent pyrene fluorescent probes are of potential interest for the construction of smart supramolecular assemblies via macroion- counterion interaction.

It is an interesting question how the hybrid surfactants arrange themselves to form closely packed regions in the supramolecular structures. These hybrids differ from conventional surfactants in that they have large polar head groups making close packing of hydrophobic domains very difficult due to the spatial obstruction. We proposed, but without solid evidence, that the counterions might be important by perturbing the solvophobic layer formation.[34] The newly synthesized hybrid clusters with pyrene as fluorescent probes offer a unique opportunity to study this phenomenon.

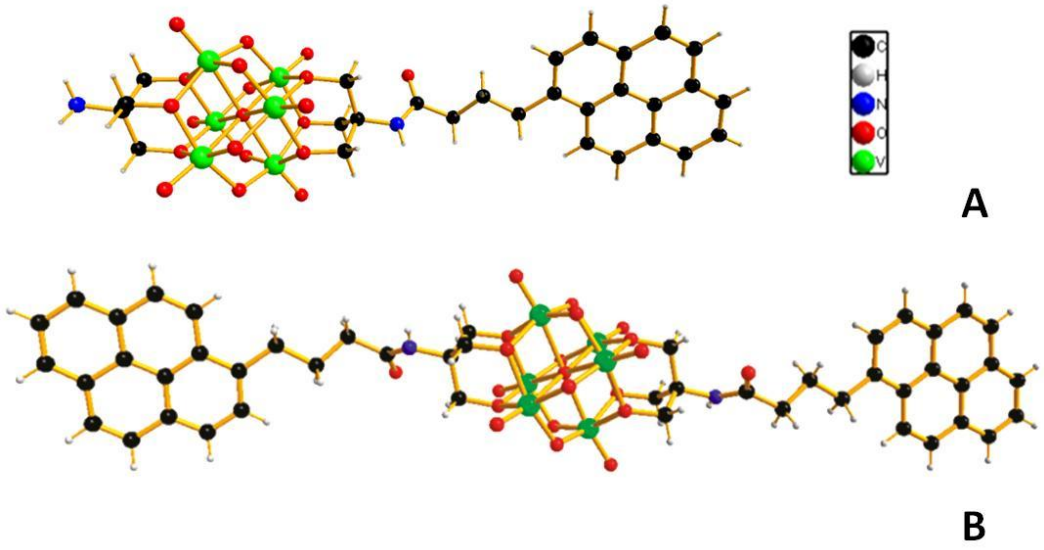


**Figure 4.8** The molecular structure of two novel polyoxometalates hybrid cluster anions **1** (A) and **2** (B) shown in combined ball-and-stick representation. Atoms are represented by: V green, N blue, O red, C black, H white.

### 4.4.2.1 Characterization of the amphiphilic properties of hybrids 1 and 2 in polar solvents.

As shown in Fig. 4.8, two novel POM based inorganic-organic hybrids are constructed by incorporating one or two pyrene functional groups onto one Lindqvist-type polyoxovanadate $[V_6O_{13}\{(OCH_2)_3CNH_2\}]^{2-}$. The linkage of flexible, hydrophobic organic tails to the inorganic POM head groups renders these new species amphiphilic. Hybrids $(TBA^+)_2$**1** and $(TBA^+)_2$**2** are insoluble in water but can be readily dissolved in dimethyl sulfoxide (DMSO), dimethyl formamide (DMF), and other polar organic solvents. For 0.1 mg/mL of hybrid $(TBA^+)_2$**1** in DMSO, a very low scattered intensity (~ 45 kcps) was collected from SLS measurements (for comparison, the scattered intensity

of pure solvent is ~ 40 kcps), indicating that the hybrid molecules prefer to remain as monomers in solution rather than large assemblies. However, when additional water was introduced to make a solvent containing up to 70 vol% water, the total scattered intensity starts to increase significantly, and supramolecular structures are observed under DLS, as shown in Fig. 4.9. The CONTIN analysis of the DLS measurement on this solution reveals a peak corresponding to assemblies with a very narrow size distribution and an average hydrodynamic radius ($R_h$) of 50 nm. The Rh value does not show angular dependence that suggests that the supramolecular structures are likely spherical. The radius of gyration ($R_g$) of the assemblies measured by SLS is 48 nm. The relation of $R_{h,0} \approx R_g$ strongly suggests that the supramolecular structures have a hollow spherical vesicular structure, which is also clearly confirmed by the TEM studies (Fig. 4.9C). The TEM image showed in Fig. 4.9D reveals several important aspects. First, the different contrast shown inside (lighter color) and around (darker color) the vesicular structures indicate they are hollow, which is quite similar to the vesicles formed by phospholipids.[35] Second, these vesicles collapsed on the carbon film due to the evaporation of internal solvent under high vacuum condition, indicating a soft and flexible nature of the vesicles' membrane. In order to form such vesicular structures in the mixed solvents as shown here, it is reasonable to assume that the hybrids use their polar POM clusters to face the hydrophilic solvent while their organic tails form a hydrophobic domain. The addition of water induces dissociation of the $TBA^+$ counterions from the POM cluster and increases the overall negative charge on the polar head groups, which in turn changes the Amphiphilicity of the hybrid molecules and leads to the vesicle formation. The above discussions focus on one set of condition (0.1 mg/mL hybrid 1 in 80:20 v/v

water/DMSO); however, similar vesicular structures are also observed in different solvents, that is, in water/ acetonitrile, or in water/methanol. When the original $TBA^+$ counterions of **1** are replaced by tetraethylammonium ($TEA^+$) or tetramethylammonium ($TMA^+$), similar vesicular structures were observed. However, compared with the case of $TBA^+$, the total scattered light intensity becomes lower, and more water is needed to trigger the vesicle formation. The $R_h$ of the large vesicular structures also changes from 50 to 30 nm and 23 nm in the same solvent system (80:20 v/v $H_2O$/DMSO) (Fig. 4.9A and B), respectively. The decrease of the vesicle size should be attributed to the shorter alkyl chains of the counterions, which decreases the size of the hydrophobic domain and consequently increases the curvature of the vesicles. These results indicate that the counterions play an important role in regulating the amphiphilic nature of the hybrid clusters and the electrostatic interactions between them. Hybrid $(TBA^+)_2$**2** in mixed solvents ($H_2O$/DMSO, $H_2O$/ acetonitrile, etc.) shows similar self-assembly behavior as hybrid $(TBA^+)_2$**1**. However, the vesicular structures formed by hybrid **2** are smaller than those formed by hybrid **1** under the same conditions. This is because an additional bending energy is needed to properly fold the two hydrophobic tails of hybrid **2** into the vesicular structure and therefore leads to a higher curvature or smaller vesicles.

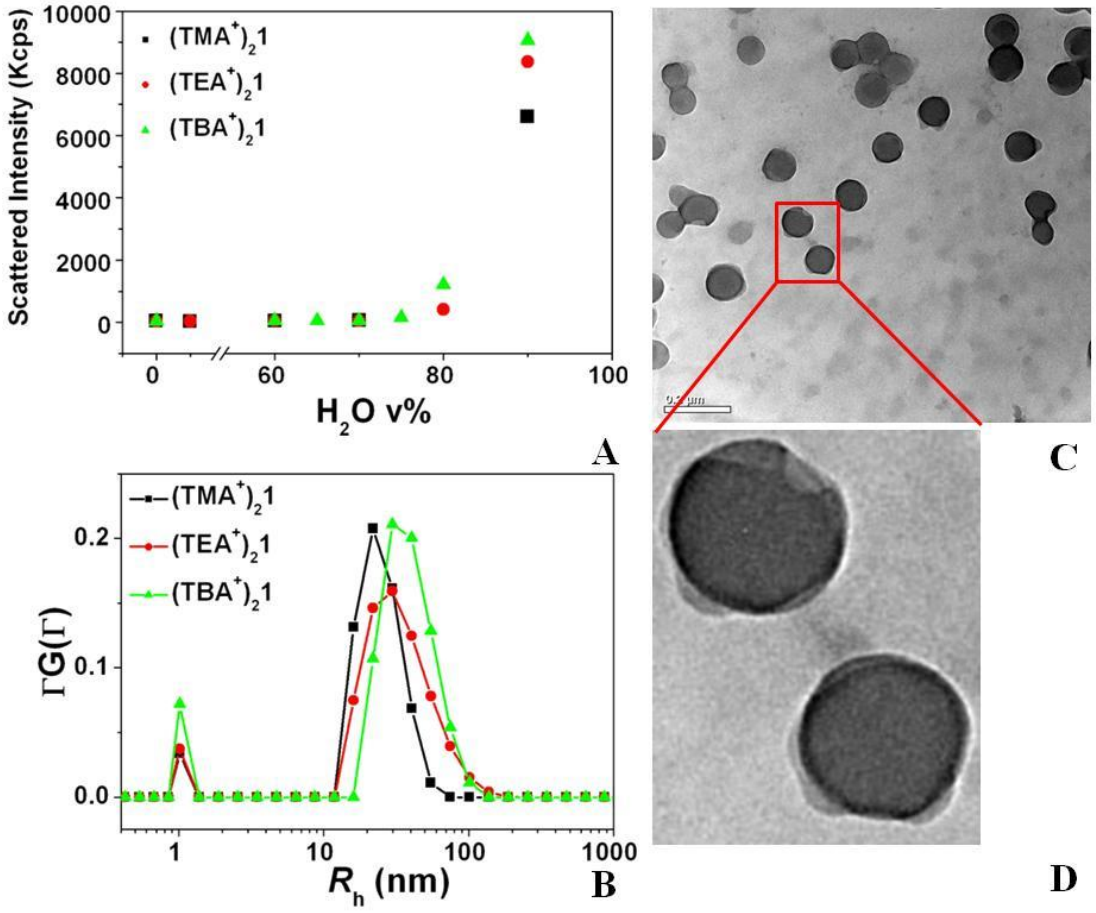


**Figure 4.9** (A) The total scattered intensity recorded by SLS for hybrid cluster **1** with different counterions in $H_2O$/DMSO mixed solvents. (B) CONTIN plot of the size distribution of vesicular structures formed by hybrid cluster **1** with different counterions in 80:20 v/v $H_2O$/DMSO mixed solvents. (C) A TEM image of the vesicular structure formed in 80:20 v/v $H_2O$/DMSO mixed solvents (bar = 0.2 $\mu$m). (D) An enlarged region of (**C**) in order to show the structural details of the hollow spherical vesicular structures.

#### 4.4.2.2 Counterions affect the packing of hybrid clusters in vesicles.

Fluorescent probes are highly useful in monitoring polarity changes of microenvironments in macromolecules and membranes. The general dependence of probe fluorescence on polarity has been attributed to the dipole-dipole interaction between the singlet excited state of the fluorophore and the solvent molecules. Specifically, the fine structural pattern in the fluorescence of the pyrene monomers is found to be independent of excitation conditions or collisional quenching but highly dependent on solvent polarity. Therefore, any changes in the pyrene fluorescence will reveal interactions between counterions and the hybrid clusters. As shown in Fig. 4.10, when counterions are $TBA^+$, $TEA^+$, or $TMA^+$, the fluorescence intensity primarily comes from the pyrene monomer, and no excimer peak is observed. Under these conditions, vesicular structures have already formed in the solution. Therefore, the fluorescence spectra indicate that the pyrene groups on the vesicle surface are not spatially close enough to form excimers. However, the fluorescence spectra are significantly different when $H^+$ counterions are present in the solution. The emission peaks of the monomer become less well-defined, and the peak of the excimer centered at 480 nm becomes the dominant one for both $H_2$**1** and $H_2$**2**. Second, it has been shown in the literature that the polarity of the microenvironment around the pyrene group is reflected by the ratio of the emission peak at 375 nm to the peak at 395 nm: the lower the ratio, the less polar the pyrene environment. Fig. 4.10B clearly shows that the pyrene groups are more solvated when large counterions (for example $TBA^+$) are present in the assemblies. In contrast, when $H^+$ ions are the counterions, the pyrene groups stay closer to each other. This data confirms

that counterions with long alkyl chains can prevent the close packing of the hybrid clusters in the vesicular structures.

More direct evidence comes from the 2D NOESY NMR measurements. In general, when a saturated or inverted proton undergoes dipolar cross-relaxation, another spatially close proton may experience an intensity enhancement; a common phenomenon termed the nuclear Overhauser effect (NOE).[36] The NOE is unique among the NMR phenomena because it does not rely on through-bond J couplings but depends only on the spatial proximity between protons.[37,38] In other words, the strength of the NOE can be used to estimate how close two protons are. In the current system, there are two possible scenarios for TBA interaction with the vesicular structure, either strongly bound to the vesicles or as free counterions in solution. Since no covalent chemical bonds are present between $TBA^+$ cations and the hybrid cluster, it is quite possible that a dynamic exchange and equilibrium exists between bound and free cations. Free $TBA^+$ cations show very weak to no NOE, while the bound TBAs are explicitly revealed through strong, negative NOE cross peaks. Moreover, the strong, negative NOE from bound $TBA^+$ cations will outweigh that from free cations and dominate the NOESY spectrum, even when the free TBAs are in considerable excess. Fig. 4.12 shows that in a 0.25 mg/mL $(TBA^+)_2$**1** solution in pure DMSO-d6, the TBA protons exhibit positive NOE cross peaks between adjacent protons indicating that the $TBA^+$ counterions exist as free ions.

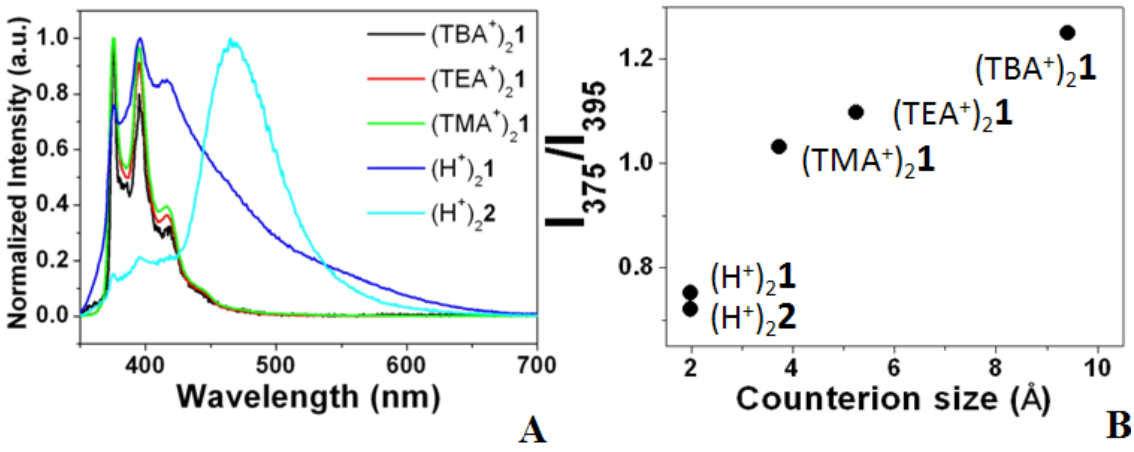


**Figure 4.10** (A) Fluorescence spectra of hybrid clusters **1** and **2** with different counterions. (For the TBA, TEA and TMA salts, the solvent is 80:20 v/v $H_2O$:DMSO; for the H salt, the solvent is $H_2O$). (B) Plot of the pyrene monomer fluorescence peak I (375nm)/I(395nm) versus the counterion size for hybrid clusters **1** and **2** with different counterions.

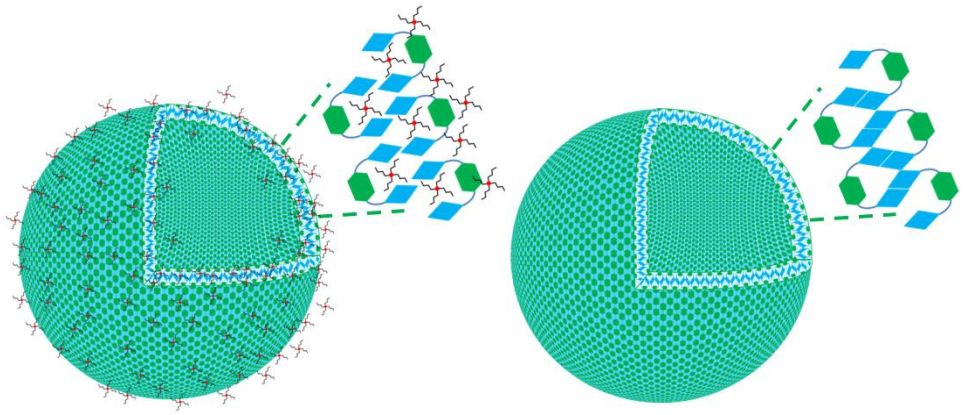

**Figure 4.11** An illustration of possible vesicular structures formed by hybrid clusters, **2**, in polar solvents, and how the $TBA^+$ counterions may be arranged in the packing of individual clusters. The hexagons, parallelograms and four-legged stars represent the POM, pyrene, and $TBA^+$ cations, respectively.

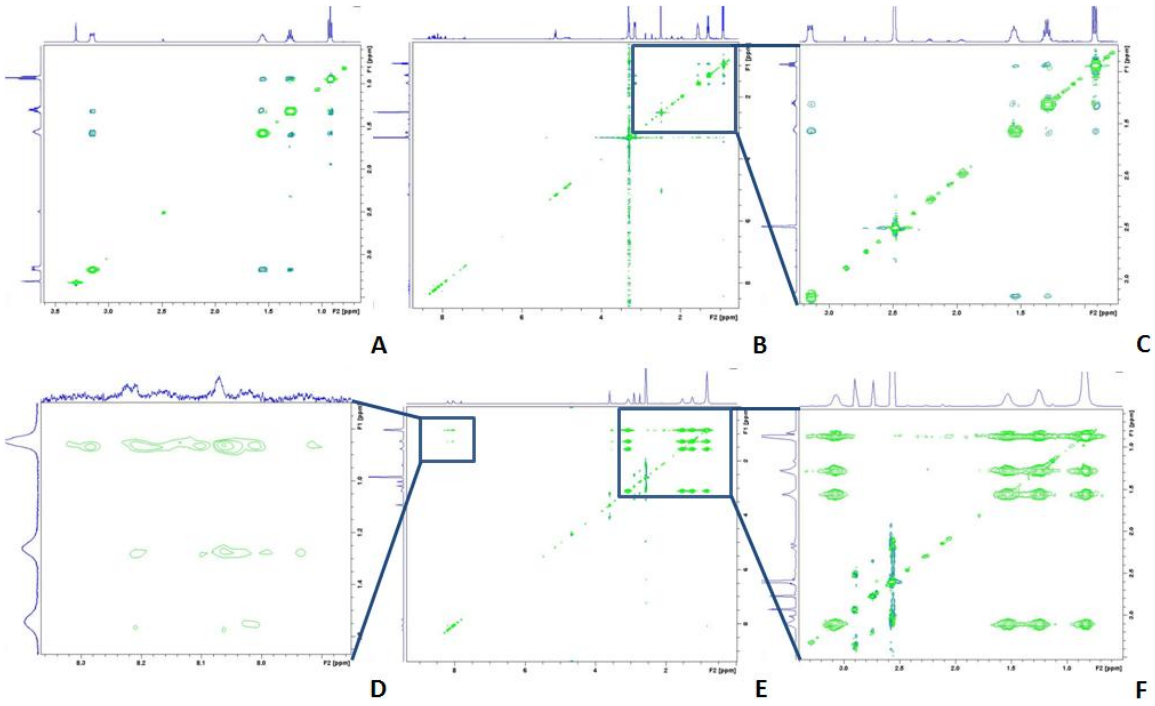


**Figure 4.12** (A) 2D NOESY spectrum of TBAI in DMSO-$d_6$. (B) 2D NOESY spectrum of $(TBA^+)_2$**1** in DMSO-$d_6$. (C) An enlarged region of **B** showing the TBA cross peaks. (D) An enlarged region of **E** showing the TBA-pyrene cross peaks. (E) 2D NOESY spectrum of $(TBA^+)_2$**1** in 90:10 v/v $D_2O$:DMSO-$d_6$ mixed solvent. (F) An enlarged region of **E** show the TBA cross peaks. (Positive NOE peaks are in dark green color while negative NOE peaks are in light green color.)

The NOE cross peak pattern is identical to that of the control compound TBAI (tetrabutylammonium iodide). This is because there is no vesicle formation in solution. The $TBA^+$ counterions interact with the $\{V_6O_{19}\}^{2-}$ POM portion through electrostatic interactions. However, when vesicular structures form in 90:10 v/v D2O/DMSO-d6 solution, the NOE spectra for $(TBA^+)_2$**1** dramatically changes. First, the previously positive NOE cross peaks become negative, indicating strong binding between the $TBA^+$ cations and the vesicles. More interestingly, a set of new negative NOE cross peaks appears between cations and the fluorescent pyrene groups on **1** (Fig. 4.12D), which do not appear in Fig. 4.12B. This clearly indicates that the amphiphilic $TBA^+$ cations interact with the hydrophobic domains in the vesicles. It is almost certain that this interaction interrupts the formation of pyrene excimers that in turn greatly affects the fluorescence pattern of the pyrene (Fig. 4.11). Previously, we noticed that the dumbbell shaped POM hybrids could form vesicles in water/acetone mixed solvents. The interesting question is how these hybrids could form closely packed hydrophobic layers in their vesicles. The giant POM head groups make the close packing of the alkyl chains very difficult due to spatial hindrance. We speculate that the alkyl chains of the $TBA^+$ cations interact with the hydrophobic domains, but there is no direct evidence for this. From the 2D NOESY NMR study, we can confirm that the amphiphilic $TBA^+$ cations are distributed partly into the hydrophobic regions of the vesicular structures. pH Sensitive Vesicles. When two pyrene groups are spatially close to each other (less than 0.5 nm) without any interruption, an excimer peak appears. We have shown earlier in the paper that replacement of the original $TBA^+$ counterions by $H^+$ through cation exchange changes the fluorescence spectra of the appended pyrene: the peaks due to pyrene excimers become dominant

relative to those from pyrene monomers, indicating a much closer packing of the hybrid clusters in the vesicular structure. This unique property gives us a great opportunity to construct a smart, pH sensitive vesicular structure and to study the effect of pH on the assembly and disassembly of vesicular structures. Fig. 4.13 shows that the initial pH for an aqueous solution of hybrid cluster **2** (*ca*. 0.44 mg/mL based on UV absorption calibration) after counterion exchange is 3.41 and the dominant fluorescence comes from the pyrene excimers. The molar ratio of hybrid **2** divided by free $H^+$ in solution is 0.87 based on solution pH, which indicates only a portion of the $H^+$ ions are released into solution and contribute to the pH, while a large amount of $H^+$ counterions are closely associated with the hybrids. (If protons are free in solution, the molar ratio should be 0.5). When dilute NaOH solution is slowly titrated into the solution of POM hybrid, a gradual decrease of the excimer peak along with a continuous increase in the pyrene monomer peaks occurs, indicating that the distance between pyrene excimers increases (larger than 0.5 nm). Because $Na^+$ has a weaker affinity for the hybrid macroanions in solution than $H^+$ does, which leads to less screening of the POM cluster from neighboring groups, the drop of proton concentration in solution will increase the repulsion between adjacent POM groups in the vesicles. When the solution pH approaches 7, the decrease in the ratio of [excimer]/[monomer] peak areas becomes much slower, indicating that the distance between hybrid clusters becomes less sensitive to pH due to the limited amount of available protons. More interestingly, in the pH range of 1-7, the whole process is reversible. In other words, the average pyrene-to-pyrene distance between adjacent clusters is reversibly tunable by changing pH. The average vesicle size recorded by DLS

at 90° scattering angle also shows pH dependence: the $R_h$ of vesicles decreases with increasing pH. Stronger electrostatic repulsion between hybrid clusters will result in a high curvature, that is, a smaller vesicle, for the assemblies; this trend shows how counterions affect the close packing of hybrid clusters. Meanwhile, the zeta potential of the vesicular structures becomes more negative with increasing pH and becomes nearly neutral at a low pH, indicating that the net charge on the vesicles increases with increasing pH.

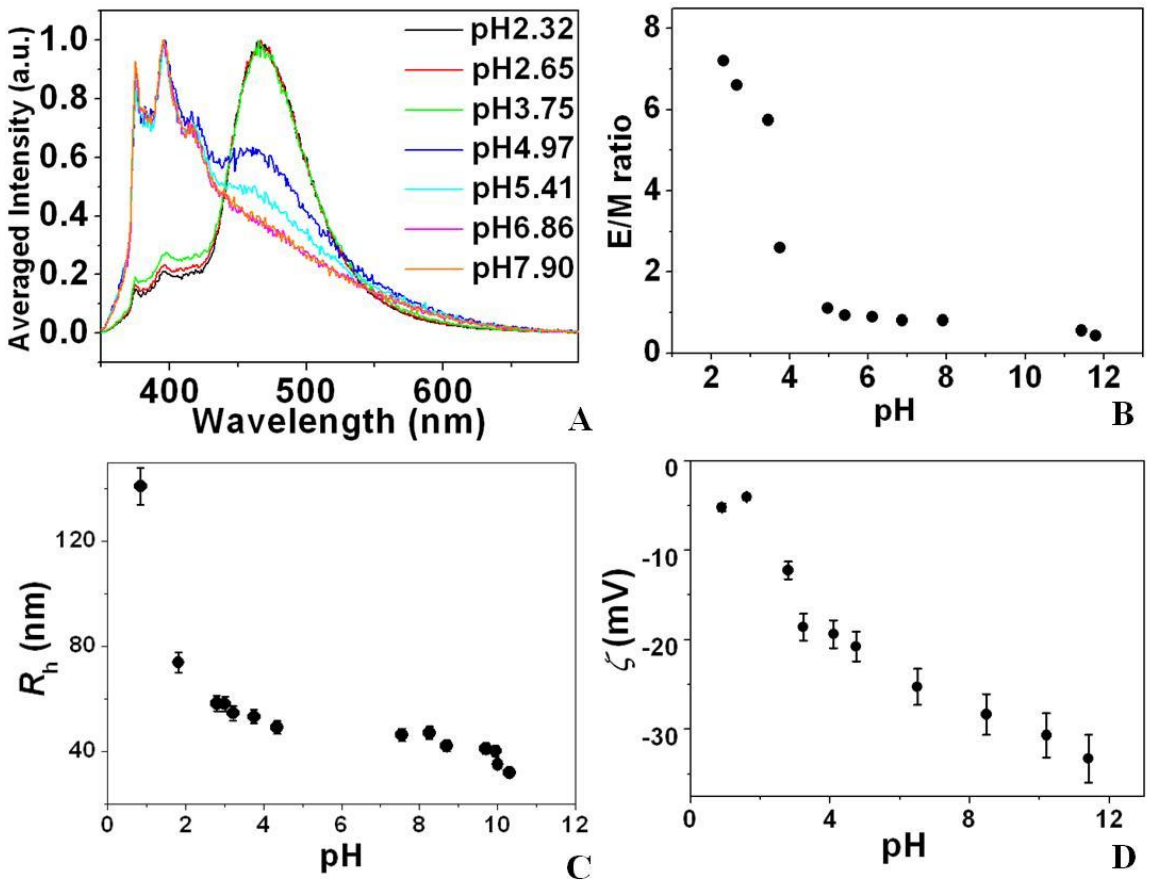


**Figure 4.13** (A) Fluorescence spectra of hybrid clusters $(H^+)_2$**2** in water at different pH values (the fluorescence intensity has been normalized). (B) Plot of pyrene excimer/monomer intensity ratio versus solution pH for hybrid clusters $(H^+)_2$**2**. (C) Change in the vesicular structure size with solution pH for $(H^+)_2$**2**. (D) Zeta potential of the vesicular structure with solution pH for $(H^+)_2$**2**.

## 4.5 Conclusions

In summary, two novel POM-based hybrid clusters were synthesized by connecting one or two organic pyrene tails with a Lindqvist type polyoxovanadate head cluster through trimester capping groups. These two hybrid clusters demonstrate noteworthy amphiphilic properties by forming spherical vesicular structures in polar solvents. Four different counterions ($TBA^+$, $TEA^+$, $TMA^+$, and $H^+$) have been used to study the counterion effect on the vesicular structures and their consequent role in the fluorescent properties of the pyrene groups on vesicle surface.

$TBA^+$ counterions not only interact with POM polar head groups but also move into the hydrophobic regions and interrupt the close packing of pyrene groups. More importantly, when $TBA^+$ counterions are replaced by protons, a dramatic change of the pyrene fluorescence pattern occurs, and the vesicle size, the fluorescence pattern, and the effective charge on the vesicles change correspondingly and reversibly with solution pH. The construction of pH sensitive vesicular structures could well have application to artificial cell studies, nanoreactors, as well as drug and gene delivery systems.

The exploration on the amphiphilic hybrid POMs and their assemblies is still in its infancy. Only a few amphiphilic hybrid POMs have been studied and their assemblies show various interesting properties. However, systematic studies of their chemical and physical properties are needed for a comprehensive understanding their fascinating features. The current achievements and remaining problems have inspired chemists to design rational synthetic strategies and synthesize novel amphiphilic hybrid POMs. There are several directions in this field deserving more attention and they may rapidly expand

during the next decade. For example, amphiphilic hybrid POMs with chiral ligands attached may demonstrate interesting self-assembly behaviors and they could find important applications for enanotioselective catalysis and separation. The incorporation of amino acids or peptides with POMs is expected to create novel hybrid materials that combine the biological functionality of biomolecules with good chemical stability of POMs. Moreover, surface modification of POMs with dendrimers, cyclodextrins, or functional polymers could be synthesized in the near future. Smart supramolecular assemblies that can response to different environmental stimuli is another important research direction for designing and synthesizing amphiphilic hybrid POMs, which may be employed as drug delivery vehicles and magnetic resonance imaging (MRI) agents.

## References


(1) Dolbecq, A.; Dumas, E.; Mayer, C. d. R.; Mialane, P. *Chem. Rev.* **2010**, *110*, 6009.

(2) Kurth, D. G.; Lehmann, P.; Volkmer, D.; Cölfen, H.; Koop, M. J.; Müller, A.; Chesne, A. D. *Chem. Eur. J* **2000**, *6*, 385.

(3) Volkmer, D.; Chesne, A. D.; Kurth, D. G.; Schnablegger, H.; Lehmann, P.; Koop, M. J.; Müller, A. *J. Am. Chem. Soc.* **2000**, *122*, 1995.

(4) Fan, D.; Jia, X.; Tang, P.; Hao, J.; Liu, T. *Angew. Chem. Int. Ed.* **2007**, *46*, 3342.

(5) Polarz, S.; Smarlsly, B.; Antonietti, M. *ChemPhysChem* **2001**, *2*, 457.

(6) Bu, W.; Wu, L.; Zhang, X.; Tang, A.-C. *J. Phys. Chem. B* **2003**, *107*, 13425.

(7) Li, H.; Yang, Y.; Wang, Y.; Wang, C.; Li, W.; Wu, L. *Soft Matter* **2011**, *7*, 2668.

(8) Qi, W.; Wu, L. *Polym. Int.* **2009**, *58*, 1217.

(9) Yu, R.; Kuang, X.-F.; Wu, X.-Y.; Lu, C.-Z.; Donahue, J. P. *Coord. Chem. Rev.* **2009**, *253*, 2872.

(10) Uchida, S.; Hashimoto, M.; Mizuno, N. *Angew. Chem. Int. Ed.* **2002**, *41*, 2814.

(11) Uchida, S.; Mizuno, N. *Chem. Eur. J* **2003**, *9*, 5850.

(12) Uchida, S.; Mizuno, N. *J. Am. Chem. Soc.* **2004**, *126*, 1602.

(13) Long, D.-L.; Kögerler, P.; Farrugia, L. J.; Cronin, L. *Angew. Chem. Int. Ed.* **2003**, *42*, 4180.

(14) Uchida, S.; Mizuno, N. *Coord. Chem. Rev.* **2007**, *251*, 2537.

(15) Song, Y.-F.; Long, D.-l.; Ritchie, C.; Cronin, L. *Chem. Rec.* **2011**, *11*, 158.

(16) Kang, H.; Zubieta, J. *J. Chem. Soc., Chem. Commun.* **1988**, 1192.

(17) Du, Y.; Rheingold, A. L.; Maatta, E. A. *J. Am. Chem. Soc.* **1992**, *114*, 345.

(18) Song, Y.-F.; Long, D.-l.; Cronin, L. *CrystEngComm* **2010**, *12*, 109.

(19) Song, Y.-F.; Long, D.-L.; Kelly, S. E.; Cronin, L. *Inorg. Chem.* **2008**, *47*, 9137.

(20) Rosnes, M. H.; Musumeci, C.; Pradeep, C. P.; Mathieson, J. S.; Long, D.-L.; Song, Y.-F.; Pignataro, B.; Cogdell, R.; Cronin, L. *J. Am. Chem. Soc.* **2010**, *132*, 15490.

(21) Chen, Q.; Goshorn, D. P.; Scholes, C. P.; Tan, X. L.; Zubieta, J. *J. Am. Chem. Soc.* **1992**, *114*, 4667.

(22) Hou, Y.; Hill, C. L. *J. Am. Chem. Soc.* **1993**, *115*, 11823.

(23) Judeinstein, P. *Chem. Mater.* **1992**, *4*, 4.

(24) Xu, B.; Lu, M.; Kang, J.; Wang, D.; Brown, J.; Peng, Z. *Chem. Mater.* **2005**, *17*, 2841.

(25) Chambers, R. C.; Atkinson, E. J. O.; McAdams, D.; Hayden, E. J.; Brown, D. J. A. *Chem. Commun.* **2003**, 2456.

(26) Misdrahi, M. F.; Wang, M.; Pradeep, C. P.; Li, F.-Y.; Lydon, C.; Xu, L.; Cronin, L.; Liu, T. *Langmuir* **2011**, *27*, 9193.

(27) Song, Y.-F.; McMillan, N.; Long, D.-L.; Kane, S.; Malm, J.; Riehle, M. O.; Pradeep, C. P.; Gadegaard, N.; Cronin, L. *J. Am. Chem. Soc.* **2009**, *131*, 1340.

(28) Errington, R. J.; Petkar, S. S.; Horrocks, B. R.; Houlton, A.; Lie, L. H.; Patole, S. N. *Angew. Chem. Int. Ed.* **2005**, *44*, 1254.

(29) Lu, M.; Nolte, W. M.; He, T.; Corley, D. A.; Tour, J. M. *Chem. Mater.* **2009**, *21*, 442.

(30) Israelachvili, J. N.; Mitchell, D. J.; Ninham, B. W. *J. Chem. Soc., Faraday Trans. 2* **1976**, *72*, 1525.

(31) Winnik, F. M. *Chem. Rev.* **1993**, *93*, 587.

(32) Kalyanasundaram, K.; Thomas, J. K. *J. Am. Chem. Soc.* **1977**, *99*, 2039.

(33) Glushko, V.; Thaler, M. S. R.; Karp, C. D. *Arch. Biochem. Biophys.* **1981**, *210*, 33.

(34) Pradeep, C. P.; Misdrahi, M. F.; Li, F.-Y.; Zhang, J.; Xu, L.; Long, D.-L.; Liu, T.; Cronin, L. *Angew. Chem. Int. Ed.* **2009**, *48*, 8309.

(35) Beck, P.; Liebi, M.; Kohlbrecher, J.; Ishikawa, T.; Rüegger, H.; Zepik, H.; Fischer, P.; Walde, P.; Windhab, E. *J. Phys. Chem. B* **2009**, *114*, 174.

(36) Ernst, R. R.; Bodenhausen, G.; Wokaun, A. *Principles of Nuclear Magnetic Resonance in One and Two Dimensions*; Oxford University Press, 1992.

(37) Hassinen, A.; Moreels, I.; de Mello Donegá, C.; Martins, J. C.; Hens, Z. *J. Phys. Chem. Lett.* **2010**, *1*, 2577.

(38) Denkova, P. S.; Van Lokeren, L.; Willem, R. *J. Phys. Chem. B* **2009**, *113*, 6703.

# Chapter 5: Nucleation and Molecular Recognition in Macroionic Solutions

## 5.1 Introduction

In previous chapters, we have shown that macro-anions and macro-cations could self-assemble into spherical, hollow, single-layered, vesicular blackberry type structures in solution when their size is between 2 to 6 nm, and with moderate charge density. To better understand this unique phenomenon, it would be helpful to study the thermodynamic and kinetic behaviors of macroions during the self-assembly process. Therefore, in this chapter, we will examine the nucleation and molecular recognition process in macroionic solutions.

## 5.2 Materials and methods

### 5.2.1 Sample preparation

Single crystals of $\{Mo_{72}Fe_{30}\}$[*], $\{Mo_{72}Cr_{30}\}$[†], and $\{U_{28}\}$[‡] were synthesized according to well-established methods.[1-3] Solution samples were prepared by dissolving certain amount of crystals in water or other specified polar solvents. For $\{U_{28}\}$, samples were prepared by dissolving crystals in basic solvents. We first prepared the basic solvent of MOH (M = Li, Na, K, Cs, TMA (tetramethylammonium), TEA (tetraethylammonium), TPA (tetrapropylammonium), and TBA (tetrabutylammonium)) with different

[*] $[Mo_{72}Fe_{30}O_{252}(CH_3COO)_{12}\{Mo_2O_7(H_2O)\}_2\{H_2Mo_2O_8(H_2O)\}(H_2O)_{91}]$ ca.$150H_2O$)
[†] $[\{Na(H_2O)_{12}\}\subset\{Mo_{72}Cr_{30}O_{252}(CH_3COO)_{19}(H_2O)_{94}\}]$ ca.$120H_2O$)
[‡] $Cs_{15}[(Ta(O_2)_4)Cs_4K_{12}(UO_2(O_2)_{1.5})_{28}]$ $20H_2O$)

concentrations and then dissolve certain amount of $\{U_{28}\}$ crystals in the solvent to make a final $\{U_{28}\}$ concentration of 0.5 mg/mL. $\{U_{28}\}$ was also dissolved in $NH_4Cl$ bulk solvents in order to study the effect of $NH_4^+$. All solutions were filtered with Millipore 0.1 $\mu$m membranes to remove any dust particles prior of light scattering measurements.

### 5.2.2 DLS and SLS

Both Dynamic Light Scattering (DLS) and Static Light Scatting (SLS) were used to characterize the sample solutions. A Brookhaven Instruments *Inc*. light scattering spectrometer, equipped with a diode-pumped solid-state (DPSS) laser operating at 532 nm and a BI-9000AT multi-channel digital correlator were used for this purpose.

The SLS was performed over a broad range of scattering angles from 30 ° to 130 °, with a 2 ° interval. The raw data was analyzed to give the radius of gyration ($R_g$) and the weight-average molecular mass ($M_w$) of the large assemblies, using the Rayleigh-Gans-Debye equation: $Hc/R_{90} = 1/M_w + 2A_2*c$, where H is an optical parameter; $M_w$ is the weight-average molecular mass of the solutes; $A_2$ is the second virial coefficient and $c$ is the solute concentration. The sample solutions examined in this study had very low concentrations; therefore, the $2A_2*c$ term can be neglected during calculations. For $\{Mo_{72}Fe_{30}\}$ or other POM solutions, the continuous increase of scattered intensity is mainly due to the increase of the number of blackberries while the mass of the blackberries only slightly increases. Discrete $\{Mo_{72}Fe_{30}\}$ macro-anions have only negligible contribution to the total scattered intensity.

For DLS measurements, the intensity-intensity time correlation functions were analyzed by the constrained regularized (CONTIN) method in order to ascertain the average hydrodynamic radius ($R_h$) of the large assemblies. Specifically, an average

apparent translational diffusion coefficient, $D_{app}$ was determined from the normalized distribution function of the characteristic line width, $\Gamma$(G); and the hydrodynamic radius $R_h$ is related to $D$ through the Stokes–Einstein equation: $R_h = k_B T/6\pi\eta D$ where $k_B$ is the Boltzmann constant and $\eta$ the viscosity of the solvent at temperature T. The particle size distribution in solution can be obtained by plotting $\Gamma$G ($\Gamma$) versus $R_h$, with $\Gamma_i G_i$ ($\Gamma_i$) being proportional to the angular-dependent scattered intensity of particle $i$ having an apparent hydrodynamic radius $R_{h,i}$. The temperature in the sample chamber was controlled to within $\pm 0.1$ ℃.

**5.2.3 Partial specific volume ($\bar{v}$) measurements.**

The partial specific volume of $\{Mo_{72}Fe_{30}\}$ in water was determined by using DA-210 Density/Specific gravity meters (KYOTO Electronics) to measure the densities of macroanion solutions at different concentrations. As shown in Fig. 5.1, the value of $\{Mo_{72}Fe_{30}\}$ was determined as 0.37004 mL/g.[4]

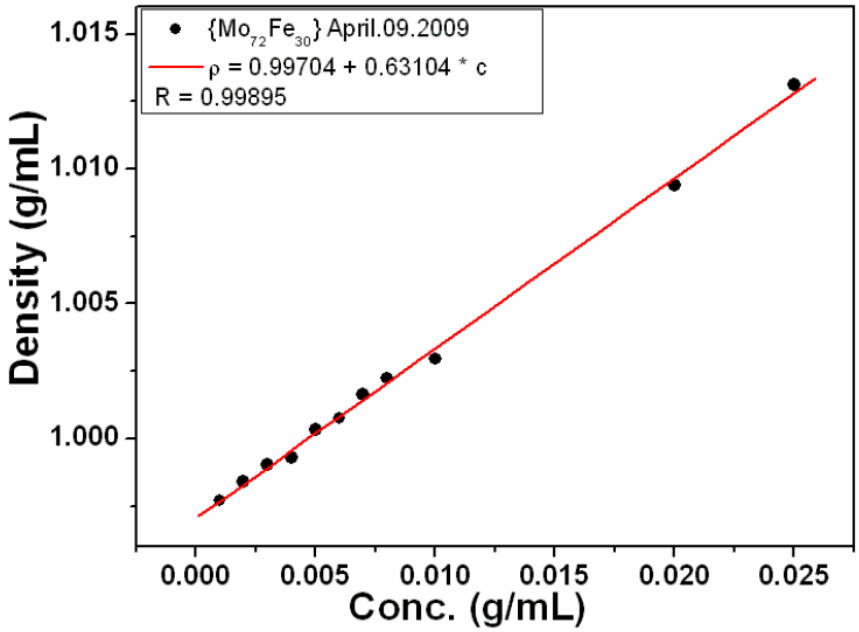


**Figure 5.1** Change of densities of $\{Mo_{72}Fe_{30}\}$ solutions with solute concentrations.

### 5.2.4 Sedimentation velocity (SV) experiments

SV experiments were performed using a Beckman model XL-A analytic ultracentrifuge equipped with a photoelectric absorbance optical detection system. Samples (440 $\mu$L) and reference solutions (450 $\mu$L) were loaded into a conventional double-sector quartz cell and mounted in a Beckman An-60 Ti rotor. Experiments were carried out at 20 ℃ and a rotor speed of 30 000 rpm. Data were collected in continuous mode at a single wavelength of 450 nm and a step size of 0.005 cm. Multiple scans at different time points (~230 scans within 3 h) were fit to a continuous size distribution using the program SEDFIT.[5]

The theoretical sedimentation coefficients for the monomer and different types of oligomers of $\{Mo_{72}Fe_{30}\}$ can be calculated by using equation:

$$s = \frac{M(1-\bar{\upsilon}\rho)}{N_A f} \tag{46}$$

where M is the molecular weight (accounting for the loss of 150 water molecules) of $\{Mo_{72}Fe_{30}\}$ as 15944 g/mol, $\bar{\upsilon}$ is the partial specific volume as 0.37004 mL/g, $\rho$ is the density of the solvent as 1.0052 g/mL at 20 °C, NA is Avogadro's number, and $f$ is the frictional coefficient. The Stokes equation can be used to determine the $f$ value for smooth, compact spherical particles:

$$f_0 = 6\pi\eta R_0 \tag{47}$$

where $f_0$ is the frictional coefficient of the spherical particles, $\eta$ is the viscosity of the solution as 1.0162 mPa·S, and $R_0$ is the radius of the sphere, which can be expressed as follows:

$$R_0 = \left(\frac{3M\bar{\upsilon}}{4\pi N_A}\right)^{1/3} \tag{48}$$

The s value for a sphere can be obtained by combining eqn. (46) to (48):

$$S_{sphere} = \frac{M^{2/3}(1-\bar{\upsilon}\rho)}{\eta\left(162\pi^2 N_A^2 \bar{\upsilon}\right)^{1/3}} \tag{49}$$

By using Eqn. (49), the sedimentation velocity coefficients for smooth, compact spherical particles can be predicted. This $s_{sphere}$ value is the maximum s value that can be obtained for a particle with a given molecular weight, because a compact sphere has the minimum surface area in contact with the solvent and consequently the particle would have a minimum frictional coefficient, $f_0$. For nonspherical particles, $f/f_0 > 1$.

## 5.3 Identify oligomer states during blackberry formation

### 5.3.1 High activation energy barrier of blackberry formation

Typically, the blackberry formation is a very slow process. For example, it requires several months for the blackberry formation process of a 0.5 mg/mL $\{Mo_{72}Fe_{30}\}$ solution to achieve equilibrium at room temperature.[6] The slowness of the blackberry formation is attributed to the high energy barrier for the transition from single macroions to blackberries. Time-resolved SLS studies are used to determine the initial "reaction" rates in $\{Mo_{72}Fe_{30}\}$ aqueous solutions at different temperatures. By using the Arrhenius equation

$$\ln(k) = -{}^{E_a}/_{RT} + B \tag{50}$$

the activation energy of the oligomer formation can be calculated as ~115 ± 8 kJ/mol, which is indeed high.[7]

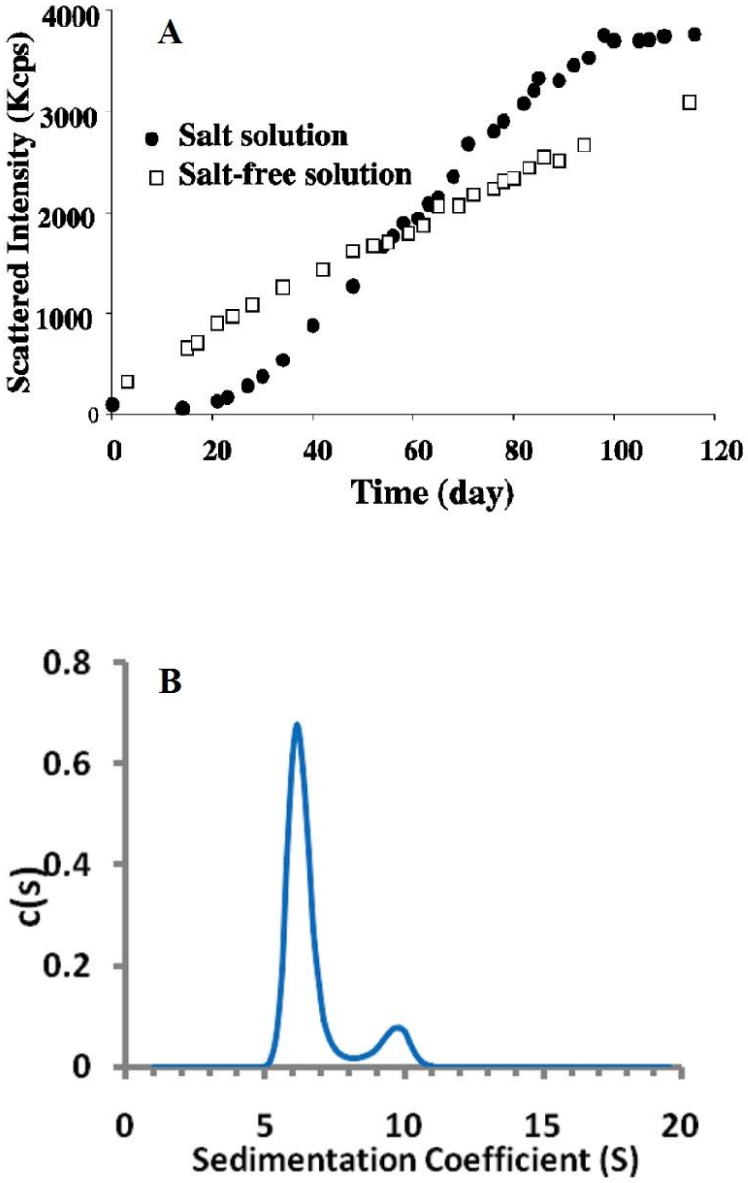


**Figure 5.2** (A) The increment of scattered intensity of two $\{Mo_{72}Fe_{30}\}$ samples in 0.9 wt% NaCl salt solution and salt-free solution. (B) Continuous size distribution c(s) analysis of $\{Mo_{72}Fe_{30}\}$ solution versus sedimentation coefficient, s. Experiments were performed at a $\{Mo_{72}Fe_{30}\}$ concentration of 10 mg/mL in 170 mM NaCl solution at 20 ℃.

### 5.3.2 Slow nucleation and fast aggregation

A close look at the time-resolved SLS studies on $\{Mo_{72}Fe_{30}\}$ aqueous solutions and other POMs solutions reveals that there is a short lag period at the beginning of blackberry formation (in minutes or days). In a 10.0 mg/mL $\{Mo_{72}Fe_{30}\}$ solution with NaCl (0.9 wt% or 0.17 mol/L) added, this lag phase extended to about 20 days, as shown in Fig. 5.2A. After filtering out the minor precipitates due to the addition of salts, the remaining solution is a stable, saturated $\{Mo_{72}Fe_{30}\}$/NaCl solution (~ 7 mg/mL) at room temperature. The initial scattered intensity from this solution is very low, suggesting that almost all the $\{Mo_{72}Fe_{30}\}$ macroanions exist as discrete ions. However, after a lag period of almost 20 days, the scattered intensity jumped up and continued to increase until it is finally stabilized after several months, indicating a slow formation of large structures. The overall kinetic picture is a sigmoidal shaped curve with a long lag phase. Normally, a sigmoidal curve is considered as a typical feature of a two-step process: slow nucleation and fast aggregation. In the initial lag period, because of the high activation energy barrier between macroions, oligomer nucleus slowly form in the solutions, and once a critical value of the rate limiting nucleus has reached, subsequent oligomers or monomers are quickly added to the growing assembly structures at a time until it is completed. Sedimentation velocity (SV) experiments performed on the $18^{th}$ day after the sample solution was prepared show direct proof of the existence of oligomers in the lag phase. As illustrated in Fig. 5.2B, the sedimentation coefficients (s) of sedimentating species and their corresponding sedimentation coefficient distributions c(s) show the coexistence of two species: s ~ 6.6 S with the dominant abundance (56%) and s ~ 9.5 S (10%). The experimental results are fairly close to the theoretical sedimentation coefficients for

{$Mo_{72}Fe_{30}$} monomers (6.9 S), dimers (11.0 S) and timers (14.5 S) by solving the Lamm equations. The experimental values are slightly lower than the theoretical ones, possibly due to the fact that the dimers are not spherical. Besides the concentration of additional salts, the length of the lag period also depends on temperature, the valent state of the cations and the anions, as well as the solvent content.

Combining the above information, we conclude that the formation mechanism of the blackberry formation should follow such a process: at the beginning, the monomers slowly associate into dimers (or oligomers). This is the rate-determining step. Once enough oligomers are available, they quickly assemble into large blackberries. This step is fast so that no "small" blackberries are observed during the whole process.

## 5.4 Molecular recognition of POMs

Molecular level recognition is an important factor that influence the self-assembly of macroions in solution. It is also a critical regulation mechanism in many biological systems.[8] Even a small change in molecule's size, shape, or polarity could largely affect the final assembled supramolecular structures. Therefore, it is an interesting question we want to ask: What would happen if two similar macroions (for instance, POM type macro-anions) are mixed together in solution? Will they form two different types of blackberries or just one type of blackberries containing the two different macroions? We use two POM type macro-anions {$Mo_{72}Fe_{30}$} and {$Mo_{72}Cr_{30}$} as model systems whose surface structures are identical to test this idea.

The aqueous solutions of {$Mo_{72}Fe_{30}$} and {$Mo_{72}Cr_{30}$} were mixed to determine whether they form homogeneous or heterogeneous blackberry structures. At 30 or 40 ℃,

the self-assembly process takes about several weeks to achieve equilibrium. The resulting solutions contain two different large species (indicated as two separated peaks in the size distribution plot) are strong evidence that these two POM macro-anions can recognize each other and form homogeneous blackberries. Further studies of centrifugation of the mixed solutions by using differently sized membranes followed by atomic absorption analysis proved that the two peaks observed from DLS are indeed homogeneous blackberries. Therefore, the current studies provide a new example of molecular level self-recognition in solution, even though it is not easy or straight forward to explain the mechanism behind this self-recognition phenomenon. Based on our previous studies, it is reasonable to say that the nucleation process or the formation of the energetic unfavorable oligomer state is the critical step for the self-recognition and the overall blackberry formation. The surface charge density of individual POM macro-anions, the surface water ligand liability, and the solvent polarity are the essential factors that influence the self-recognition.

However, one possibility of the self-recognition needs to be excluded: the kinetic effects (*i.e.*, one type of POMs assembles faster than the other). Therefore, we monitored the kinetics of the blackberry formation process by using static light scattering. Our results showed that the two assembly processes occur at almost the same speed (Fig. 5.3), especially in the initial stages (Fig. 5.4). The kinetic curves obtained can approximately be explained by a two-step nucleation-growth process: (i) the macroanions slowly associate into thermodynamically unfavorable intermediate oligomers and dimers; (ii) when enough oligomers of appropriate shape and metal content are present, formation of the two different blackberries is accelerated.

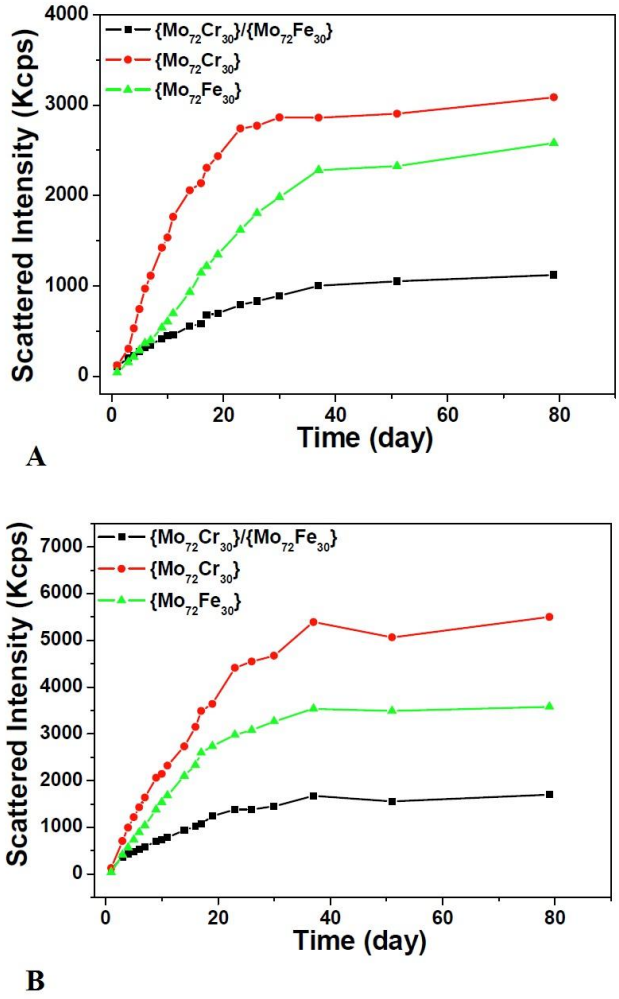


**Figure 5.3** (A) Increment of the total scattered intensity as function of time at 30 ℃ for three different solutions (0.5 mg/mL for the $\{Mo_{72}Cr_{30}\}$ and $\{Mo_{72}Fe_{30}\}$ scenarios while the "mixture" contains 0.25 mg/mL of each). The curve for the $\{Mo_{72}Cr_{30}\}$ case shows stronger scattered intensity because of the larger blackberries. The scattered intensity from the mixed solution is lower due to the lower individual macroionic concentrations. (B). Increment of total scattered intensity as function of time at 40 ℃ (same macroionic concentrations as above). The self-assembly process is accelerated at a higher temperature.

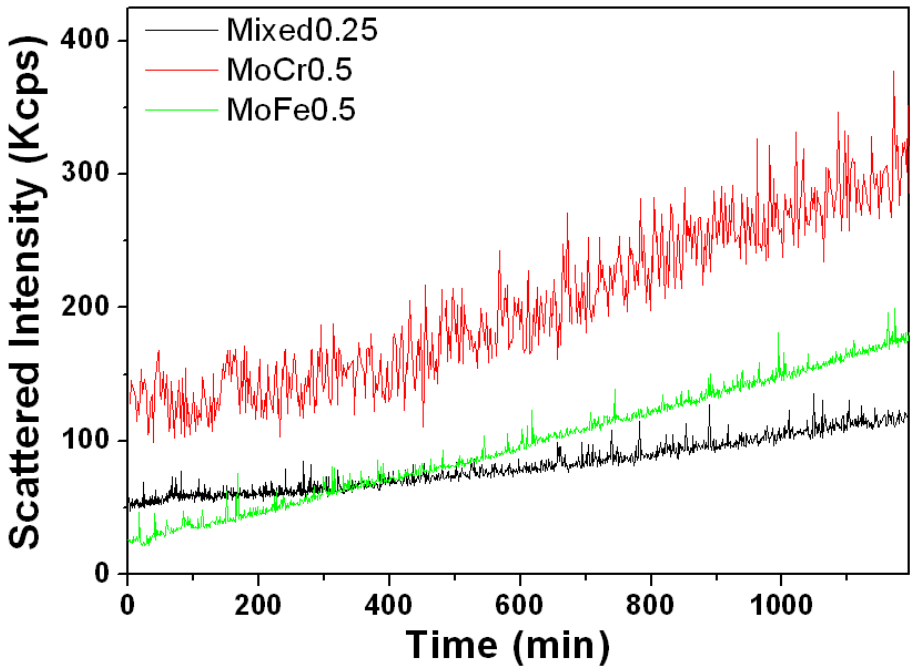


**Figure 5.4** Increment of the total scattered intensity (from time-resolved SLS studies) as function of time at 40 ℃ and at the early stage. The curves for the freshly prepared solutions of $\{Mo_{72}Cr_{30}\}$ and $\{Mo_{72}Fe_{30}\}$ are almost identical in slope and both show minor lag periods, suggesting that the dimer/oligomer formation processes in the solutions are kinetically similar.

## 5.5 Critical size of POMs to form blackberries

As we discussed in chapter 2, a large group of POM type macro-anions with different size and shape can self-assemble to form blackberry type supramolecular structures in polar solvents. The size disparity between large macroions and small counterions is critical (~ 10 to 1), which is much smaller compare with that of colloidal particles and counterions (~ 1000 to 1). In this range, counterions could no longer be treated as point-like charge, *i.e.* the effect of counterion size needs to be considered when calculating the macroion-counterion interactions. Ion-pairing and/or like charge attraction may be enhanced under this circumstance.

Now, we want to explore further this unique phenomenon by asking: What is the difference between small POM versus large POM when they form blackberries? Is there a size limitation of POMs to be able to form blackberries? Answer these questions would greatly help us to better understand the fundamental driving forces associated with self-assembly and provide valuable insight to many other colloidal or biological phenomena. At present, the smallest macro-anion that was shown to be able to form blackberries is $\{Cu_{20}P_8W_{48}\}$, a nanowheel with size being 2.2 × 1.1 nm. We want to push this limit to even smaller POMs, and in the following sections, we will discuss the self-assembly process of one smaller POM of $\{U_{28}\}$.

### 5.5.1 Self-assembly of $\{U_{28}\}$ macro-anions in basic aqueous solutions

$\{U_{28}\}$ represents an unprecedented family of actinyl peroxide nanoclusters which were recently discovered and described by Burns *et al.*.[3] It has an overall spherical geometry with a diameter of 1.77 nm, and is assembled from 28 identical uranyl peroxide

polyhedra within the clusters, as shown in Fig. 5.5 $\{U_{28}\}$ and other similar actinyl peroxide nanoclusters were obtained from alkaline solutions containing peroxide under ambient conditions. As indicated from its formula, $Cs_{15}[(Ta(O_2)_4)Cs_4K_{12}(UO_2(O_2)_{1.5})_{28}]\cdot 20H_2O$, each $\{U_{28}\}$ anionic cluster is balanced by 15 $Cs^+$ outside the cluster and 4 $Cs^+$, 12 $K^+$ inside the cluster. In solution, those small counterions could dissociate from $\{U_{28}\}$ cluster and the inside $Cs^+$ counterions may exchange with outside counterions or they may be released into solution. Therefore, consider the small size of this cluster; its surface charge density may be higher than previous mentioned giant POMs. Because of the peroxide ligands that link the uranyl peroxide polyhedral, $\{U_{28}\}$ is more stable in basic conditions. In our experiments, most of the samples were prepared by dissolving $\{U_{28}\}$ crystals in basic solvents.

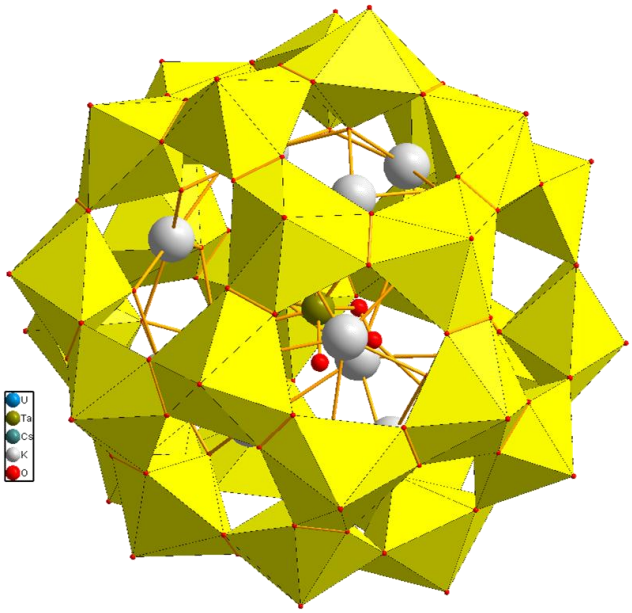


**Figure 5.5** Molecular structure of $\{U_{28}\}$ POM.

As shown in Fig. 5.6, for a typical $\{U_{28}\}$ sample of 0.5 mg/mL in 0.05 mol/L KOH solution at 30 ˚C, the scattered intensity recorded by SLS shows a sigmoidal shaped curve with a long lag period of 41 ±2 days. The scattered intensity reaches a plateau after 120 days, representing the end of the self-assembly process. Interestingly, the $R_h$ value of the assembled structures increases with time during this process, as shown in Fig. 5.6, and is finally stabilized at ~ 70 nm. Similar trend was observed in solutions with different counterions. From TEM studies, we identified spherical, hollow vesicle-like structures, which indicate $\{U_{28}\}$ indeed form blackberry structures (Fig. 5.7).

There are two interesting and important phenomena in the self-assembly of $\{U_{28}\}$, which quite different from previously mentioned large POMs. The first one is the elongated lag phase during the self-assembly process and the second one is the increment of $R_h$ with time. As summarized in Table 5.1, we noticed that the length of the lag period is sensitive to the counterion hydration size, the counterion concentration, and temperature. For instance, $Li^+$ ion cannot trigger the self-assembly of $\{U_{28}\}$ even at a high concentration of 1.0 mol/L, probably due to its large hydration shell. Meanwhile, $Na^+$ and $K^+$ can effectively decrease the length of the lag period, with $K^+$ has a stronger effect than $Na^+$ under the same concentration. $Cs^+$ will immediately precipitate $\{U_{28}\}$ even with a concentration below 0.01 mol/L, implying it has an even stronger effect than $K^+$. Ammonium type counterions can also affect the lag period of $\{U_{28}\}$, especially for small $NH_4^+$ and $TMA^+$. However, $TEA^+$, $TPA^+$, and $TBA^+$ may interact with $\{U_{28}\}$ in a different way so that there is no clear lag phase during the self-assembly process (the overall scattered intensity is also lower than alkaline counterions at the same concentration when system reached equilibrium), probably due to the hydrocarbon chains

which prevents the formation of tight ion-pairing between the $\{U_{28}\}$ cluster and counterions.

Temperature also plays an important role in regulating the lag period. For instance, at room temperature, the lag period of $\{U_{28}\}$ in 0.05 mol/L KOH is about 67 days, which decreases to 41 ± 2 days at 30 ˚C and further reduces to 36 ± 2 days at 40 ˚C. The decrease of lag period is an indication that the energy barrier is lowered at higher temperature.

There are several other interesting points need to be mentioned for the lag period. First, as shown in Fig. 5.8, in a wide concentration range, the change of the lag period does not have a simple linear relationship with the alkaline concentration. Instead, the lag period follows a roughly exponential decay manner with the alkaline concentration. At low counterion concentration range, there is one critical concentration above which the lag period is measurable and the self-assembly process will proceed. For example, the critical concentration for $Na^+$ is 0.08 mol/L; for $K^+$ is 0.05 mol/L; for $NH_4^+$ is 0.05 mol/L; and for $TMA^+$ is 0.1 mol/L. Second, the lag period is more sensitive to different counterions in lower concentration range. As shown in Fig. 5.8, at 0.1 mol/L counterion concentration the lag period difference between $K^+$, $NH_4^+$, and $TMA^+$ is much larger compared with that of 0.5 mol/L. Meanwhile, at high counterion concentration, the lag period is eliminated for most of the counterions around 1.0 mol/L. Counterions have duel effects on the lag phase: one is the specific ion-pairing formation and the other is the increment of total ionic strength. Therefore, the current plot indicates at lower concentration, the specific ion-pairing effect of different counterions is more critical; while at higher

concentrations, the effect of total ionic strength increment takes over and the difference between lag periods shrinks.

The second phenomenon that the self-assembly of $\{U_{28}\}$ is different from large POMs is the continuous increment of $R_h$ with time before it reaches equilibrium. Our previous blackberry formation model for large POMs indicates that once the blackberries are formed in solution, their size normally remain the same throughout the overall self-assembly process and only the number of blackberries increases. However, it is not the case for $\{U_{28}\}$, as shown in Fig. 5.8. Instead of directly forming the final blackberry structures, individual $\{U_{28}\}$ clusters may form intermediate states with different $R_h$ which continuously grow until reach the final, thermodynamically stable blackberries in solution.

The above mentioned phenomena could be explained by the high surface charge density of $\{U_{28}\}$, and its small size. From our previous studies we know that the blackberry formation is a spontaneous, free energy favorable process with a huge activation energy barrier between single POMs and blackberries. In other words, the oligomers state in the early nucleation step is unstable and only when the oligomers' concentration reaches a critical value the whole self-assembly process can move forward quickly, which is evidenced by the fact of the sigmoidal curve. Therefore, the elongated lag period (much longer than normal large POMs) indicates there is an even higher activation energy barrier between the single macroion state and the blackberry state. Another possibility is because of the small size of the $\{U_{28}\}$ POM, thermal fluctuation may have a stronger influence on the stability of the POM-counterion-POM ion-pairings in solution, so the $\Delta G$ between the single POM state and the blackberry state becomes

smaller. Under extreme conditions when the activation energy barrier is large enough or the $\Delta G$ is small enough, it is reasonable to assume that POMs can no longer form blackberries in solution.

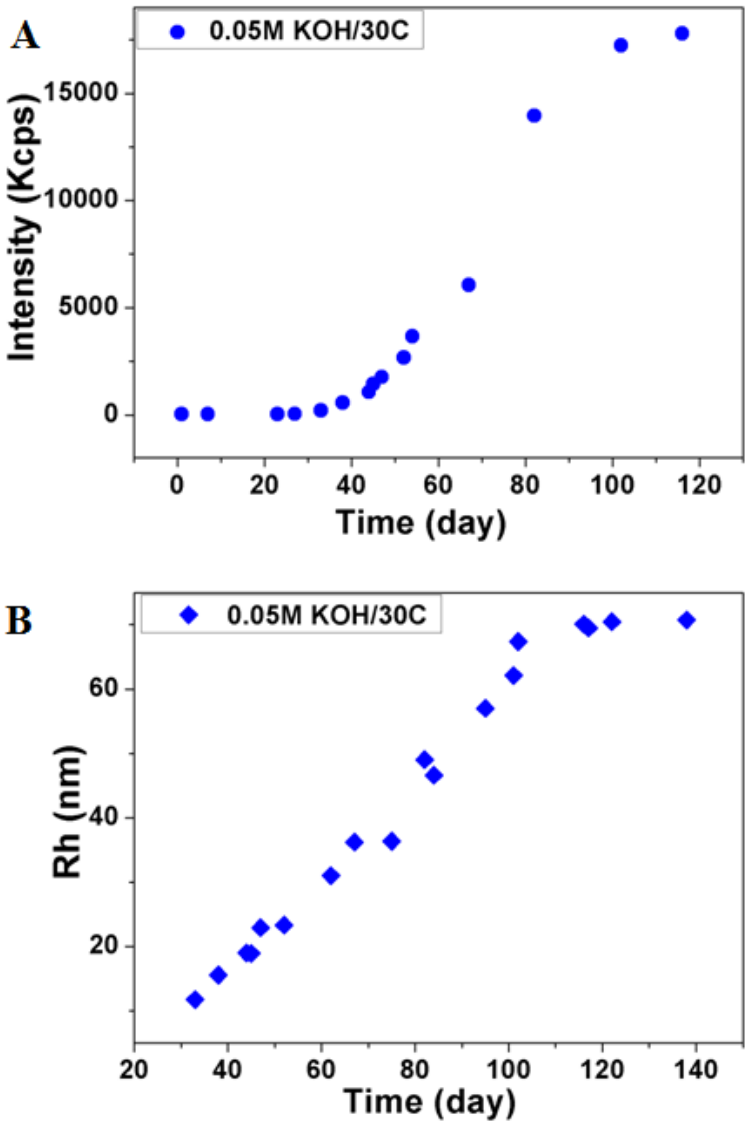


**Figure 5.6** (A) Total scattered intensity change with time for a 0.5 mg/mL $\{U_{28}\}$ sample in the 0.05 mol/L KOH bulk solution. (B) $R_h$ change of the same sample at different days.

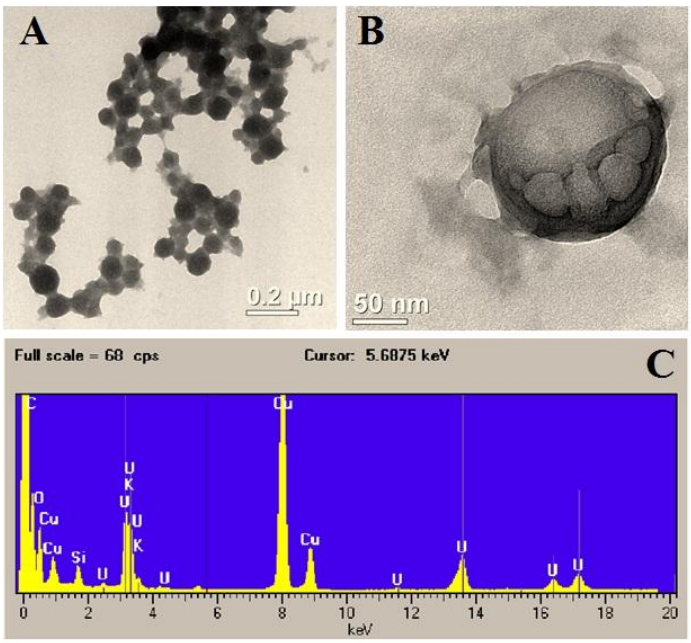


**Figure 5.7** (A) and (B) TEM images of blackberry structures formed by $\{U_{28}\}$ in solutions. (C) EDS analysis of the individual blackberry structure.

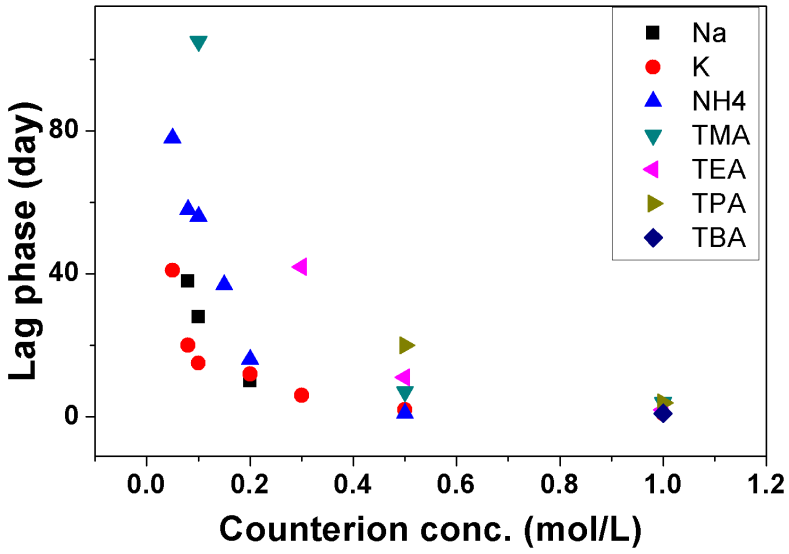


**Figure 5.8** The lag period of blackberry structure formation in different alkaline solutions.

**Table 5.1** The lag period of blackberry structure formation in different alkaline solutions.

| | counter ion conc.(mol/L) | lag phase (day) | temperature (°C) |
|---|---|---|---|
| $Li^+$ | 0.1 | ∞ | 30 |
| | 0.3 | ∞ | 30 |
| | 0.5 | ∞ | 30 |
| | 1 | ∞ | 30 |
| $Na^+$ | 0.08 | 38 ± 2 | 30 |
| | 0.1 | 28 ± 2 | 30 |
| | 0.2 | 10 ± 1 | 30 |
| $K^+$ | 0.01 | ∞ | 30 |
| | 0.02 | ∞ | 30 |
| | 0.05 | 41 ± 2 | 30 |
| | 0.08 | 20 ± 2 | 30 |
| | 0.1 | 15 ± 1 | 30 |
| | 0.2 | 12 ± 1 | 30 |
| | 0.3 | 6 ± 0.5 | 30 |
| | 0.5 | 2 ± 0.2 | 30 |
| | 1 | 1 ± 0.1 | 30 |
| | 0.05 | 67 ± 3 | 25 |
| | 0.05 | 36 ± 2 | 40 |
| $NH_4^+$ | 0.05 | 78 ± 4 | 30 |
| | 0.08 | 60 ± 3 | 30 |
| | 0.1 | 56 ± 3 | 30 |
| | 0.15 | 37 ± 2 | 30 |
| | 0.2 | 16 ± 1 | 30 |
| | 0.5 | 1 ± 0.1 | 30 |
| $TMA^+$ | 0.1 | 105 ± 5 | 30 |
| | 0.5 | 7 ± 0.5 | 30 |
| | 1 | 4 ± 0.2 | 30 |
| $TEA^+$ | 0.1 | 350 ± 18 | 30 |
| | 0.3 | 42 ± 2 | 30 |
| | 0.5 | 11 ± 1 | 30 |
| | 1 | 2 ± 0.2 | 30 |
| $TPA^+$ | 0.1 | ∞ | 30 |
| | 0.3 | ∞ | 30 |
| | 0.5 | 20 ± 1 | 30 |
| | 1 | 4 ± 0.2 | 30 |
| $TBA^+$ | 0.1 | ∞ | 30 |
| | 0.3 | ∞ | 30 |
| | 0.5 | ∞ | 30 |
| | 1 | 1 ± 0.1 | 30 |

## 5.6 Conclusions

In summary, kinetic studies show that the self-assembly of POMs into blackberries in solution is a free energy favorable process with a high activation energy barrier. The total scattered intensity recorded by SLS during the self-assembly shows a sigmoidal curve, indicating a two-step formation process which includes a slow nucleation step followed by a fast aggregation step. The slow nucleation step is critical to the molecular level self-recognition of two almost identical POMs $\{Mo_{72}Fe_{30}\}$ and $\{Mo_{72}Cr_{30}\}$ in water. The similar increment speed of the scattered intensity of the two POMs in the initial couple of hours indicates that the molecular recognition is not because of different association rate.

More interestingly, small POMs such as $\{U_{28}\}$ has shown different self-assembly behaviors than large POMs in solution. Besides the fact of an extended lag phase which is sensitive to counterion type, counterion concentration, and temperature, the $\{U_{28}\}$ macroions do not directly from blackberry structures but maybe through some intermediate states, as shown from the continuous increment of $R_h$. These unique behaviors may stem from the high surface charge density and the small size of the $\{U_{28}\}$, which would affect the activation energy barrier height and the stability of macroion-counterion ion pairing.

## References


(1) Müller, A.; Sarkar, S.; Shah, S. Q. N.; Bögge, H.; Schmidtmann, M.; Sarkar, S.; Kögerler, P.; Hauptfleisch, B.; Trautwein, A. X.; Schünemann, V. *Angew. Chem. Int. Ed.* **1999**, *38*, 3238.

(2) Todea, A. M.; Merca, A.; Bögge, H.; van Slageren, J.; Dressel, M.; Engelhardt, L.; Luban, M.; Glaser, T.; Henry, M.; Müller, A. *Angew. Chem. Int. Ed.* **2007**, *46*, 6106.

(3) Burns, P. C.; Kubatko, K.-A.; Sigmon, G.; Fryer, B. J.; Gagnon, J. E.; Antonio, M. R.; Soderholm, L. *Angew. Chem. Int. Ed.* **2005**, *44*, 2135.

(4) Zhang, J.; Li, D.; Liu, G.; Glover, K. J.; Liu, T. *J. Am. Chem. Soc.* **2009**, *131*, 15152.

(5) Schuck, P. *Biophys J.* **2000**, *78*, 1606.

(6) Liu, T. B. *J. Am. Chem. Soc.* **2003**, *125*, 312.

(7) Liu, G.; Liu, T. *Langmuir* **2005**, *21*, 2713.

(8) *Cellular and Biomolecular Recognition: Synthetic and Non-Biological Molecules*; Jelinek, R., Ed.; Wiley-VCH: Weinheim, Germany, 2009.

# Chapter 6: Counterion distribution around Hepatitis B viral capsid and dimer protein probed by SAXS

## 6.1 Introduction

Highly charged bio-macromolecules with sizes on the nanometer scale can also be treated as macroions. In these bio-macroionic systems, electrostatic interactions are fundamental to various phenomena, especially in regulating nucleic acid (DNA and RNA) condensation and folding, maintaining protein tertiary structure, and directing the assembly of viral capsids. For example, recent studies of a short DNA oligonucleotide (25 base pairs, about 8 nm) in solution have shown a short-range attraction between like-charged DNAs, and the magnitude is quite sensitive to the valence and the concentration of small counterions.[1] In this case, DLVO theory fails to predict the biologically important attraction of like-charged bio-macroions.

The Hepatitis B virus (HBV) belongs to the hepadnavirus family and is one of five different viruses that cause liver disease in humans.[2] Despite the development of antiviral drugs, it remains as a public health issue worldwide. The HBV capsid plays an important role in the virus' replication cycle, which provides a vehicle for protecting and transferring genetic materials. The core antigen (cAg) of the HBV capsid protein is a polypeptide of 183 residues, which can be divided into two functional domains: One is the "core" domain of residues 1-140 and the other is a "protamine" domain (residues 150-183). The two domains are connected by a linker peptide (residues 141-149). The

protamine domain strongly binds nucleic acids to the inner surface of the capsid due to its highly basic nature.[2] It is believed that the electrostatic interactions between the negatively charged nucleic acids and the positively charged protamine domain stabilize the overall capsid structure.[3] However, a recent study on a Cp149 protein (a truncated capsid protein without the protamine domain) has shown that it can also form stable capsid like structures in the presence of 0.15- 0.70 M NaCl.[4] The capsids assembled from the Cp149 protein have an average size of 36 nm with 240 copies of the Cp149 subunits, which are nearly identical to the native T = 4 (triangulation number) type HBV capsids.[5] Cryo-EM reconstruction studies also revealed the well-defined structure of the capsids assembled from Cp147 proteins, which formed the same type capsids as Cp149.[6] These studies show that the interactions between HBV capsid proteins, especially the assembly domain, not the interactions between capsid proteins and nucleic acids play the major role for the capsid structure formation.

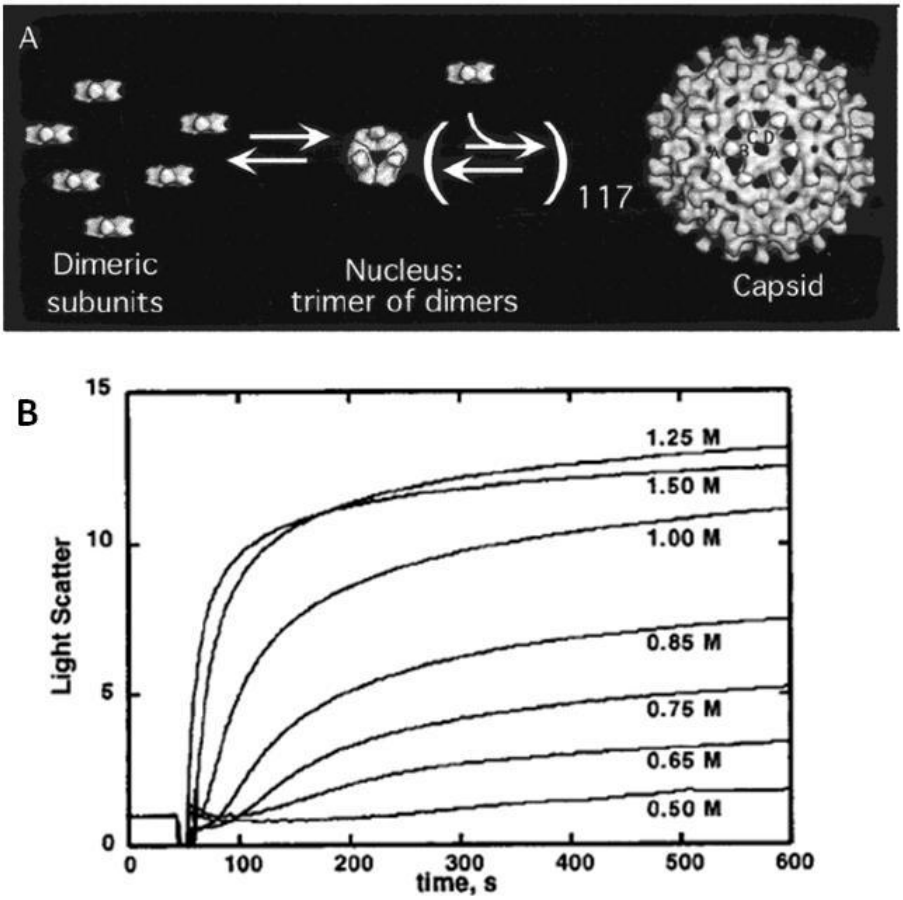


**Figure 6.1** (A) An illustration of the self-assembly of HBV dimer proteins into a complete capsid in solution (B) Addition of NaCl into buffered Cp149 dimer solutions triggers the formation of HBV capsids, as evidenced from the increment of scattered intensity. The light scattering was recorded by a fluorometer at 320 nm, and at 20℃ for about 600 s. The dimer protein concentration was 5 $\mu$M, and the buffer was 0.1 M sodium bicarbonate (pH 9.5). Different salt concentrations were used to induce the assembly of by the addition of buffered NaCl at 50 s. (Copyright: American Chemical Society, 1999)

Hydrophobic interactions, Coulomb interactions, hydrogen bonding, and salt bridges are the possible driving forces for the assembly of HBV capsids.[7,8] Ceres and Zlotnick studied the self-assembly process of HBV capsids in detail and they found that the formation of capsids is largely affected by the protein concentration, solution pH, and the ionic strength.[4] Fig. 6.1A shows the general formation process of HBV capsids in solution: The homodimeric Cp149 proteins first form a trimer of dimers during the nucleation step, after which individual dimers are quickly added to the trimer until the complete capsid is formed. At neutral pH, the strength of the attractive interaction between the Cp149 dimer proteins is about -4.4 kcal/mol of each subunit contact at 37˚C. The attractive interaction increases with temperature and ionic strength, and 75% of the surface areas buried between adjacent dimers are hydrophobic, suggesting at neutral pH hydrophobic interactions are the major attractive forces.[4]

Further studies also demonstrated the importance of ionic strength and solution pH in regulating the capsid formation. As shown in Fig. 6.1B, the assembly rate and the percentage of capsids dramatically increase with NaCl concentration, as evidenced from the total scattered intensity recorded by light scattering. The kinetic curves are sigmoidal, indicating a slow nucleation and fast aggregation process. With the addition of NaCl, not only does the lag phase become shorter but also the slope of the aggregation phase gets steeper, and the maximum scattered intensity also increases, indicating more capsids are formed at higher ionic strength. The size of the capsids assembled by Cp149 dimers is the same as the native HBV capsid protein, and they have the same mobility in the native agarose gel and density in the sucrose gradient, indicating that these assemblies are nearly

identical to native HBV capsids.[5] The stability of the Cp149 capsids is lower than the native ones, but they are stable in high pH condition because of the hysteresis effect, which prevents the dissociation of HBV capsids.

The purified Cp149 dimer proteins are stable in 0.1 M bicarbonate buffer (pH 9.5), and they do not self-assemble until the NaCl concentration is higher than 0.6 M (Fig. 6.1B). Kegel *et al.*[8] calculated the surface charge density of the Cp149 dimer proteins based upon experimental results and argued that the surface charge density of Cp149 dimer should decrease with solution pH, because the surface charges come from the ionic residues on the protein surface that exposed to solution. In other words, under high pH conditions, the Cp149 dimers are highly charged while at neutral pH, their surface charges are largely diminished. The addition of large amount of NaCl dramatically screens the Coulombic repulsion between dimers and facilities the formation of capsids.

Not only limited to NaCl, Zlotnick *et al.* also found that other cations, including $K^+$, $Mg^{2+}$, $Ca^{2+}$, $Zn^{2+}$, and $Ni^{2+}$ can induce the formation of HBV capsid, although probably through different mechanisms.[9] Fig. 6.2 summarized the critical concentration of mono- and di-valent counterions that induces the formation of HBV capsids by 5 $\mu$M of Cp149 dimer proteins in 50 mM HEPES buffer (pH 7.5) at room temperature. For example, it requires more than 0.2 M of $Na^+$ or $K^+$ ions to induce the assembly, judging from the large increment of scattered intensity. Divalent cations of $Mg^{2+}$ and $Ca^{2+}$ require lower concentrations (~ 50 mM) to induce a significant assembly. $Zn^{2+}$ and $Ni^{2+}$, on the other hand, only need ~ 200 $\mu$M to induce the assembly, indicating a selective and specific binding to Cp149, probably through the formation of coordination bonds. However, in

the current study, changes in scattered light intensity could not provide detailed information on the possible formation of oligomers, as the oligomers may have a low concentration. But the presence of oligomers is critical to understanding the role of counterions in the formation of HBV capsids. A more sensitive and more accurate technique, such as small angle X-ray scattering, may provide more valuable information to resolve this problem.[1,10,11]

Meanwhile, to some extent, the formation of HBV capsids is similar to the formation of blackberry-type structures in solution.[12] Both systems form highly symmetrical, hollow, shell structures self-assembled from well-defined monomers through weak interactions (no chemical bond formation). The monomers (proteins versus POMs) are equivalently distributed on the surface of the shell (capsids versus blackberries). Both types of self-assembly process have similar kinetic properties: a two-step process of slow nucleation and fast aggregation formation. There is a lag phase due to the nucleation step which is sensitive to ionic strength and temperature in both systems. Since Cp149 proteins can also be treated as nano-scaled macroions, the study of the counterion distribution around HBV capsid and Cp149 dimer proteins would be of great help in understanding the effect of counterion mediated interactions during the formation of HBV capsids.

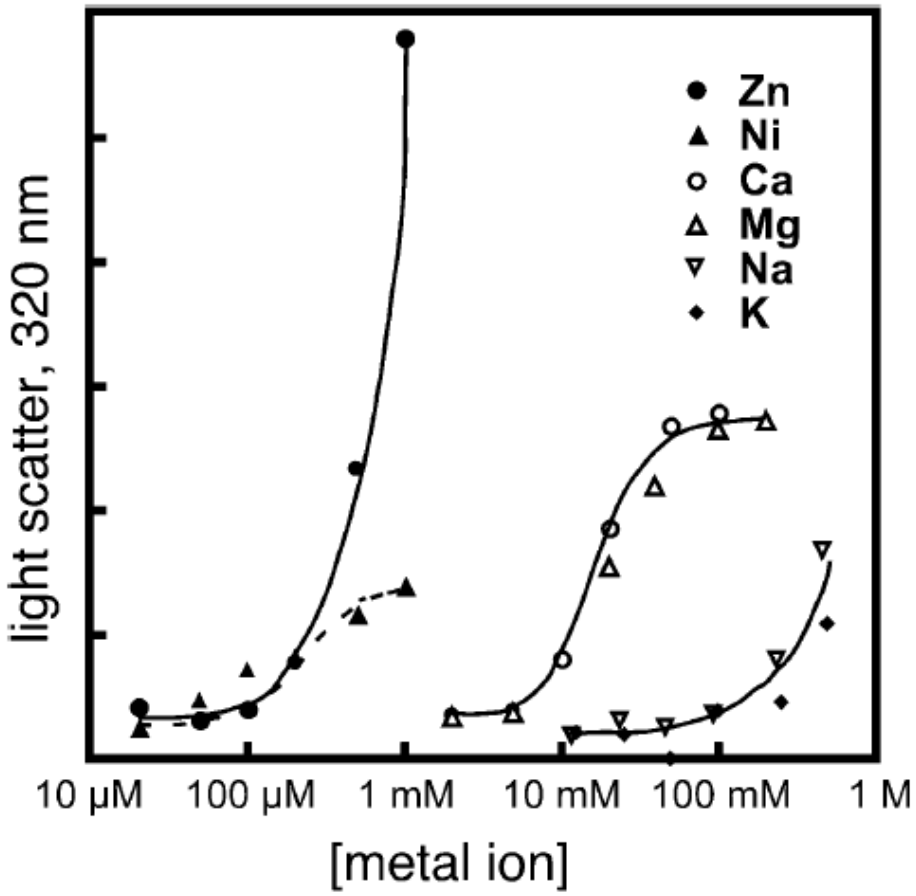


**Figure 6.2** Mono- and divalent cations can induce the assembly of 5 $\mu$M HBV Cp149 proteins into capsids in 50 mM HEPES pH 7.5 at room temperature, as monitored by static light scattering at 90˚. All of the samples were incubated for 24 hours before assessing the sample by light scattering. All metal ions tested here were in the form of chloride salts. (Copyright: American Chemical Society, 2004)

## 6.2 Instrumentation

### 6.2.1 Small angle X-ray scattering (SAXS)

Small angle X-ray scattering (SAXS) is a powerful technique that provides valuable information on macromolecules in solution. It normally uses elastic scattering of X-rays and is performed at small angels (0.1 – 10 degrees). The scattering of the incident X-ray leads to interference effects which results in a specific scattering pattern. Critical parameters of the macromolecules such as the radius of gyration $R_g$, molecular shape, persistence length, molecular weight, and intermolecular interactions can be extracted from the scattering data.[10] Although it is a relatively low resolution (~ 1 nm) probe for illustrating structural information compared with X-ray crystallography, the power of SAXS actually lies in its ability to work with dynamic or unconstrained systems.

The excess scattered intensity of solutes (macromolecules and small ions) is generated from the electron density difference as compared with the solvent background. If target molecules have the same electron density as the solvent, they become invisible and do not give any useful information. For molecules that have different electron density as the solvent, the scattered intensity $I$(q) can be expressed as:

$$I(q) = F(q)S(q) \tag{51}$$

where $F$(q) is the form factor and $S$(q) is the structure factor of the molecules. The form factor represents the size and shape of the molecules and the structure factor is determined by interparticle interactions which can be assumed as 1 in the absence of interparticle interactions in dilute solutions. The scattering vector, $q$, is defined as:

$$q = \frac{4\pi}{\lambda} sin\Theta \tag{52}$$

in which $\lambda$ is the wavelength of the incident X-ray and $\Theta$ is one half of the scattered angle.

In diluted system where there is no interparticle interaction, the scattered intensity for isolated particles can be described by Guinier's law:

$$I(q) = I_0 exp - \frac{1}{3} R_g^2 q^2 \tag{53}$$

where $I_0$ is the forward scattered intensity and $R_g$ is the radius of gyration of the molecules in solution. The Guinier plot, ln($I$(q)) versus $q^2$, should be fitted with a linear function whose intercept gives $I$(0) and the slope yields $R_g$. Guinier's law is only valid for small angles, i.e. $qR_g < 1.3$; therefore, this method is only suitable for analyzing scattering data in the low $q$ range. The linearity of the Guinier plot represents the sample homogeneity and deviations indicate either attractive or repulsive inter-particle interactions.

A useful tool for visibly detecting conformational changes within the target molecule is the pair-density distribution function P(r) plot, which is used to describe the paired-set of distances between all of the electrons within the molecular structure:

$$P(r) = \int_0^\infty \frac{I(q) r q}{2\pi^2} \sin(rq) \mathrm{d}q \tag{54}$$

$I$(0) and $R_g$ can be derived from $P$(r):

$$I(0) = 4\pi \left( \int_0^{D_{max}} P(r) \mathrm{d}r \right) \tag{55}$$

$$R_g^2 = \int_0^{D_{max}} r^2 P(r) \mathrm{d}r \Big/ \int_0^{D_{max}} P(r) \mathrm{d}r \tag{56}$$

where r is the distance between the paired scattering elements in the molecules and $D_{max}$ is the maximum diameter of a given molecule.

For proteins or nucleic acids which may contain non-regular tertiary structures, the knowledge of $R_g$ is apparently not enough. More structural information can be extracted from the scattering data by using Kratky plots of $I(q)q^2$ versus $q$, which emphasize the shape of $I(q)$ for $q$ beyond the Guinier region.

All SAXS experiments were performed at the 12-ID-B/C beamline, Advanced Photon Source (APS), Argonne National Laboratory. The incident photon energy was 12 KeV at 12-ID-B beamline and 15 KeV at 12-ID-C beamline. To minimize the X-ray exposure damage and to get better averaged scattering signal, a stop-flow device was used. The flow rate was programmed as $\pm 20$ $\mu$L/step. 10 camera shots were taken for one typical measurement with an exposure time of 1 second. Raw data were averaged and the background scattered intensity from solvent was subtracted.

**Characterization of the counterion distribution around HBV capsids**. The HBV capsids were dialyzed against HEPES buffer (50 mM HEPES, 10 mM BME, pH 7.5) for 12 hours before the SAXS experiments. The counterion (KCl, RbCl, CsCl, $MgCl_2$, and $CaCl_2$) solutions of ~ 0.50 M were prepared by using the same HEPES buffer. A 200 $\mu$L of HBV capsid solution was used for one typical SAXS experiment. For example, after collecting the initial scattered curve for capsids in HEPES buffer, $K^+$ was added into the capsid sample by pipeting 2 $\mu$L of KCl solution each time. A total of 20 $\mu$L of KCl solution was used. A similar procedure was done for other counterion solutions.

**Counterion induced self-assembly of HBV dimer**. The HBV dimers were dialyzed against buffer N (50 mM $NaHCO_3$, 10 mM BME, pH 9.6) for 12 hours before the SAXS experiments. The counterion (KBr, RbCl, CsCl, and $MgCl_2$) solutions of ~ 0.50 M were prepared by using the same buffer N. A 300 $\mu$L of HBV dimer solution was used for one

typical SAXS experiment. For example, after collecting the initial scattered curve for dimers in buffer N, $Rb^+$ was added into the dimer sample by pipeting 3 $\mu$L of RbCl solution each time. A total of 54 $\mu$L of RbCl solution was used. A similar procedure was done for other counterion solutions.

## 6.3 Synthesis of HBV capsid protein

### 6.3.1 Cp149 gene optimization, transfer, and expression

The Cp149 gene was ordered from GenScript and optimized for expression in *E. coli.*with an N-terminal NdeI restriction site and a C-terminal XhoI restriction site. The whole gene sequence is shown below:

```
5′CATATGGACATCGACCCGTACAAAGAATTCGGTGCG
  ACCGTTGAACTGCTGTCTTTCCTGCCGTCTGACTTC
  TTCCCGTCTGTTCGTGACCTGCTGGACACCGCGGCG
  GCGCTGTACCGTGACGCGCTGGAATCTCCGGAACAC
  TGCTCTCCGCACCACACCGCGCTGCGTCAGGCGATC
  CTGTGCTGGGGTGACCTGATGACCCTGGCGACCTGG
  GTTGGTACCAACCTGGAAGACCCGGCGTCTCGTGAC
  CTGGTTGTTTCTTACGTTAACACCAACGTTGGTCTG
  AAATTCCGTCAGCTGCTGTGGTTCCACATCTCTTGC
  CTGACCTTCGGTCGTGAAACCGTTCTGGAATACCTG
  GTTTCTTTCGGTGTTTGGATCCGTACCCCGCCGGCG
  TACCGTCCGCCGAACGCGCCGATCCTGTCTACCCTG
  CCGGAAACCACCGTTGTTCTCGAG-3′
```

Insertion of Cp149 genes from the original pUC57 vector into the pET24a vector was done by routine DNA insertion and ligation procedure. DNA and vector quantitation was done by gel electrophoresis on a 1% agarose gel. Ligation of the DNA with the pET vector was carried out using a 1: 4 ratio of pET vector to insert and 1 $\mu$L of T4 DNA

ligase. The reaction was incubated at 16˚C overnight. Next, 1 μL of the ligation reaction was used to transform DH5α cells. Since the pET vector is kanamycin resistant and contains the T7lac promoter, the DH5α cells were grown on LB plates containing kanamycin. Clones containing the accurate DNA sequence were then transformed into *E. coli* BL21(DE3) cells for large scale expression.

### 6.3.2 Cell growth

#### 6.3.2.1 Starter preparation

4.46 mL of D.I. water was added into each of two 10 mL plastic culture tubes. After autoclaving for 20 minutes, 10 μL of 1M $MgSO_4$, 1 μL of 1000× trace metals, 50 μL of 25% aspartate, 100 μL 50×M, 62.5 μL of 40% glucose, 100 μL of 17 amino acids, and 40 μL of methionine were added to each of the two tubes. Then, about 1 mg of *E. coli*. cells carrying pET vector with Cp149 DNA was added to the two tubes. The two starter tubes were kept in warm room at 37˚C overnight, shaking at 225 rpm.

#### 6.3.2.2 Cell growth media preparation

We used ZYM-5052 media as the cell growth media. In a 4 L Erlenmeyer flask, 20 g of NZ-amine AS, 10 g of yeast extract, and 1916 mL of D.I. water were added. The solution was autoclaved for 20 min and cooled down to room temperature. Next, 4 mL of 1M $MgSO_4$, 400 μL of 1000× trace metals, 40 mL of 50× 5052, and 40 mL of 50×M buffer were added into the flask.

#### 6.3.2.3 Cell growth

For a cell growth test, we monitored the UV absorption change at 600 nm of the solution each hour until the absorption reached equilibrium. Specifically, 10 mL of starter was first transferred into the flask with 2 L growth media. After shaking the solution for several minutes, we took 0.2 mL of the solution and diluted it to 1 mL with D. I. water. We recorded its UV absorption as the starting point. Then we loaded the flask into a shaker in the warm room at 37˚C. For each hour, we took 0.2 mL of the solution and diluted it to 1 mL and recorded the UV absorption value. After 8 hours, the UV absorption reached a plateau and we removed the flask from the warm room. For future cell growths, we always grew the cells for 8 hours.

After the solution cooled down to room temperature, we transferred all of the solution into two plastic 1 L sized centrifuge bottles. The two bottles were then loaded into a Beckman J6-MC Centrifuge and spun at 5000×g for 30 min at 4˚C. Later, all the supernatant solution was dumped, and 80 mL of 0.9 wt% cold NaCl salt solution was added to dissolve the cell pellet at the bottom of the centrifuge bottles. A total of ~100 mL of homogeneous cell solution was transferred to a 250 mL centrifuge bottle and spun in JA-14 rotor at 5000×g for 30 min at 4˚C. After that, the supernatant was removed and the cell pellet was stored at -80˚C for future use.

### 6.3.3 Protein purification

#### 6.3.3.1 Cell lysis

One cell pellet was taken out from -80˚C freezer and thawed on ice for 1 hour. The pellet was transferred into a glass beaker and 40 mL of lysis buffer (100 mM $Na_2HPO_4$, 300 mM NaCl, and 10 mM imidazole at pH 8.0) was added. The mixture was sonicated for 15 minutes at 4˚C to lyse cells and transferred into a 250 mL plastic centrifuge bottle. The mixture was spun at 27500×g for 30 minutes at 4˚C. The resulting pellet was discarded and the supernatant was collected for the next step.

#### 6.3.3.2 Ni-NTA agarose column

The supernatant was mixed with 25 mL of Ni-NTA agarose gel (purchased from QIAGEN) and the mixture was stirred for 1 hour before being loaded into a plastic column at 4˚C. About 50 mL of washing buffer (100 mM $Na_2HPO_4$, 300 mM NaCl, and 70 mM imidazole at pH 8.0) was used to wash out any non-binding proteins. About 60 mL of elution buffer (100 mM $Na_2HPO_4$, 300 mM NaCl, and 250 mM imidazole at pH 8.0) was slowly added to the column and protein fractions (in total about 40 1.5 mL fractions) were collected. After checking the fractions for purity using SDS-PAGE gel analysis, we combined the fractions that containing pure Cp149 protein and dialyzed against buffer N (50 mM $NaHCO_3$, 10 mM BME, pH 9.6) overnight at 4˚C.

#### 6.3.3.3 Gel filtration column

The dialyzed protein solution was first concentrated by using an Amicon 15 mL ultrafiltration concentrator (30K MWCO) to about 8 mL, followed by adding solid urea

into the solution to a concentration of 3 M. The mixture was incubated on ice for 2-3 hours to break capsids into capsid protein dimers. 5 mL of the dimer sample was injected onto a Hiprep 16/60 Sephacryl S-300 column at 4˚C equilibrated with buffer N. The flow rate was 0.5 mL/min. The void peak normally came out at 70 minutes, and the dimer peak normally came out at 130 minutes. The dimer faction was checked by SDS-PAGE and then concentrated to ~ 5 mL by using Amicon 15 mL ultrafiltration concentrator (10K MWCO). This concentrated protein solution was dialyzed against a 50 mM HEPES buffer (pH 7.5 with 10 mM BME) for overnight at 4˚C. NaCl was added into this dimer solution to a final concentration of 0.5 M NaCl to induce the formation of HBV capsids. The mixture was incubated on ice for at least 2 hours (HBV dimer protein is reassembled and redissociated to ensure protein activity) and then injected onto a Hiprep 16/60 Sephacryl S-300 column at 4˚C equilibrated with buffer N. The flow rate was 0.5 mL/min. The capsid peak normally came out at 70 minutes. The capsids were redissociated by adding solid urea to 3M and rechromatagraphed by gel filtration in buffer N. The same procedure was followed to collect the dimer protein. The final dimer solution was filtered and stored at -80 ˚C.

## 6.4 Counterion distribution around HBV capsids

Small angle X-ray scattering (SAXS) is used to study the counterion distribution around HBV capsids in solution. SAXS is a powerful probe for macromolecules which provides information about the size, shape, compactness, and molecular weight of the target molecules in solution.[10] To one sample of 200 $\mu$L HBV capsids (1.2 mg/mL) in 50 mM HEPES buffer at pH 7.5, different metal chloride salts were added to change the

counterion concentration. Then the radius of gyration ($R_g$) of the capsids was calculated based on the scattered curves in Guinier region (Eqn. 53). As shown in Fig. 6.3, we found that $R_g$ of the capsids increased with all five counterions introduced to the system, and for all different counterions, the increment of $R_g$ approaches to a plateau at higher salt concentration. Di-valent counterions ($Ca^{2+}$, $Mg^{2+}$) showed more pronounced effect of increasing $R_g$ than mono-valent counterions ($K^+$, $Rb^+$ and $Cs^+$) did. Since there is no aggregation of capsids under these conditions monitored by SAXS, and it has been shown that the size of the capsids does not change with different counterions,[5] the most reasonable explanation would be the increment of $R_g$ is attributed to the counterions that closely surrounding the capsids. Studies on counterion distribution around biological macroionic molecules, such as DNA, have shown that counterions with higher valent state tend to bind macroions more strongly than mono-valent counterions.[13] Since SAXS is sensitive to the change of electron density of the target particles, strongly adsorbed di-valent counterions should contribute more in changing $R_g$ of the capsids than loosely adsorbed mono-valent counterions. As mentioned before, it requires more than 200 mM of $Na^+$ or $K^+$ ions to induce the assembly but only 50 mM of divalent cations of $Mg^{2+}$ or $Ca^{2+}$. In other words, mono-valent counterions only weakly interact with HBV capsids; at least in the current concentration range (0 – 100 mM). Moreover, as listed in Table 6.1,[14] the hydrodynamic radii of di-valent counterions are larger than that of mono-valent counterions. This could also be another reason why the $R_g$ of the capsids is larger for di-valent counterions than mono-valent counterions under the same counterion concentration.

**Table 6.1** Ionic radii of unhydrated and hydrated cations.

| Cation | Unhydrated Radii (pm) | Hydrated Radii (pm) |
|---|---|---|
| $Li^+$ | 94 | 382 |
| $Na^+$ | 117 | 358 |
| $K^+$ | 149 | 331 |
| $Rb^+$ | 163 | 329 |
| $Cs^+$ | 186 | 329 |
| $Mg^{2+}$ | 72 | 428 |
| $Ca^{2+}$ | 100 | 412 |
| $Zn^{2+}$ | 74 | 430 |

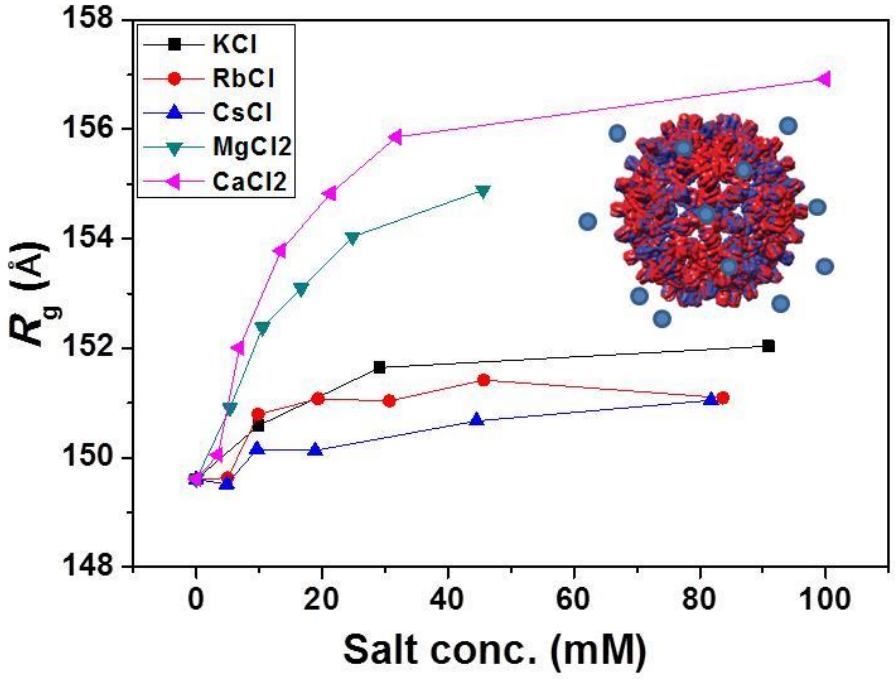


**Figure 6.3** The change of $R_g$ of HBV capsids as a function of different salt concentrations. Inset is a model of how counterions may distribute around HBV capsids.

## 6.5 Counterion induced self-assembly of Cp149 dimers

To further test the role of counterions in the self-assembly process of HBV capsids, we studied the counterion induced self-assembly of the Cp149 dimers. Unlike previous results, we found under high pH (9.6) and low ionic strength (50 mM $NaHCO_3$) conditions, the highly charged Cp149 dimers could self-assembly into larger structures, as shown in Fig. 6.4. For example, in the initial place where no $K^+$ was around, the scattered curve of pure Cp149 dimers had only one broad, structureless peak, with the maximum locating around 0.075 $Å^{-1}$. When $K^+$ ions were added into the dimer solution and the $K^+$ concentration is higher than 40 mM, several new peaks gradually emerged, which were nearly identical to the characteristic scattered peaks of HBV capsids (the red curve on the bottom of each plot in Fig. 6.4), indicating that the Cp149 dimers started to self-assemble into oligomers a with well-defined structure, but not irregular aggregates. Those new peaks became clearer with increasing $K^+$ concentration, indicating the formation of nearly complete capsids. Divalent counterions, for example, $Mg^{2+}$, only required ~ 1 mM to induce the self-assembly process.

These results indicate the critical counterion concentration of inducing the formation of HBV capsids should be lower than previous reported.[9] Further studies of finding the binding affinity between counterions and HBV dimers by isothermal titration calorimetry (ITC) may help us understand the role of counterions in regulating the formation of capsids.

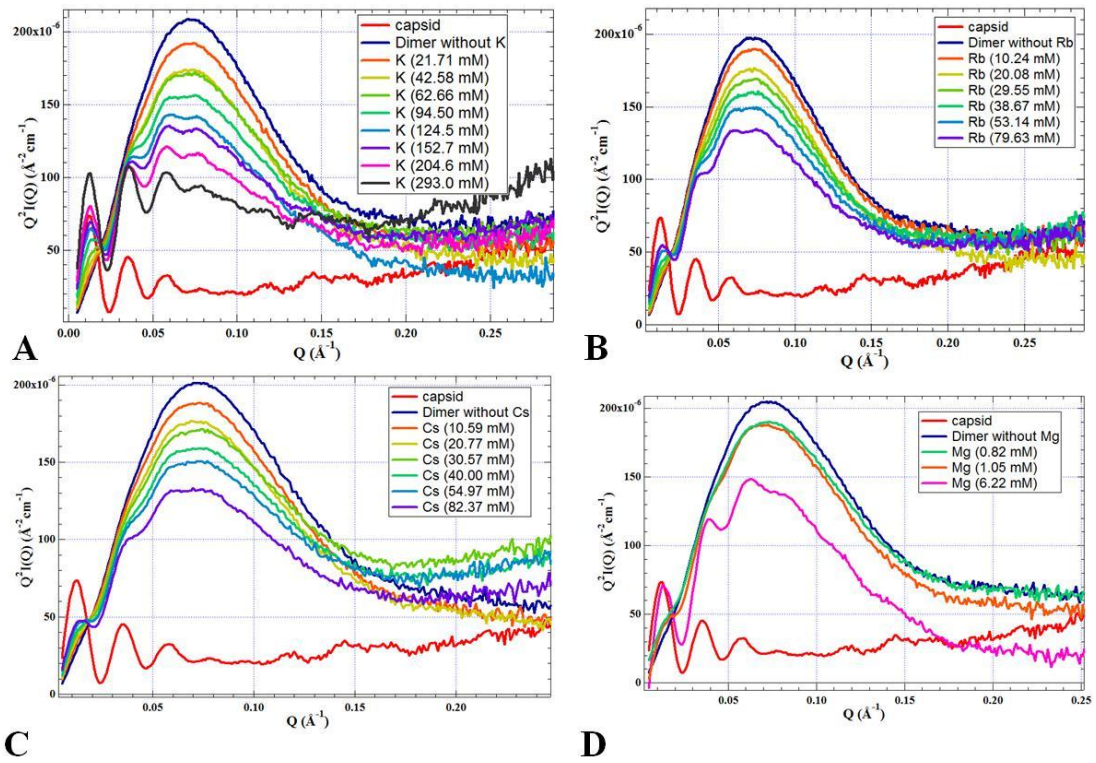


**Figure 6.4** Kratky plots of SAXS intensity $Q^2I(Q)$ versus $q$ for HBV dimers in 50 mM sodium bicarbonate buffer (pH 9.6) with different counterions. (A) $K^+$, (B) $Rb^+$, (C) $Cs^+$, and (D) $Mg^{2+}$. The blue curve is the initial scattering curve for dimer solution without any additional salt and the red curve represents the fully assembled capsids. Other color curves in between represent the scattering curves with different counterion concentrations.

## 6.6 Conclusions

The current SAXS studies on the counterion distribution around HBV capsids have shown that the $R_g$ of the capsids increases with the addition of counterions. The increment is more sensitive for di-valent counterions compared to mono-valent counterions. At relatively high salt concentrations, the increment approaches to a plateau, indicating the saturation of counterions around HBV capsids. These results imply that the HBV capsids are still highly charged in solution and have a strong effect on condensing di-valent counterions.

Another interesting finding is that the formation of HBV capsids from the dimer proteins is sensitive to counterion type and concentration. It is possible that under this condition, the counterion condensed on the Cp149 dimer surface may provide attractions and leads to the self-association of HBV dimers. This result supports our previous findings that counterion mediated attraction exists among macroions in solution and is critical to understand their solution behaviors. Future studies of mapping counterion distribution around HBV dimers by anomalous SAXS (ASAXS) and finding the binding affinity between counterions and HBV dimers by isothermal titration calorimetry (ITC) will be conducted to better understand the role of counterions during the formation of HBV capsids.

## References


(1) Das, R.; Mills, T. T.; Kwok, L. W.; Maskel, G. S.; Millett, I. S.; Doniach, S.; Finkelstein, K. D.; Herschlag, D.; Pollack, L. *Phys. Rev. Lett.* **2003**, *90*, 188103.

(2) Steven, A. C.; Conway, J. F.; Cheng, N.; Watts, N. R.; Belnap, D. M.; Harris, A.; Stahl, S. J.; Wingfield, P. T. *Adv Virus Res* **2005**, *64*, 125.

(3) Wingfield, P. T.; Stahl, S. J.; Williams, R. W.; Steven, A. C. *Biochemistry* **1995**, *34*, 4919.

(4) Ceres, P.; Zlotnick, A. *Biochemistry* **2002**, *41*, 11525.

(5) Choi, Y.; Park, S. G.; Yoo, J.-h.; Jung, G. *Virology* **2005**, *332*, 454.

(6) Conway, J. F.; Cheng, N.; Zlotnick, A.; Stahl, S. J.; Wingfield, P. T.; Steven, A. C. *PNAS* **1998**, *95*, 14622.

(7) Zlotnick, A.; Johnson, J. M.; Wingfield, P. W.; Stahl, S. J.; Endres, D. *Biochemistry* **1999**, *38*, 14644.

(8) Kegel, W. K.; Schoot, P. v. d. *Biophys. J.* **2004**, *86*, 3905.

(9) Stray, S. J.; Ceres, P.; Zlotnick, A. *Biochemistry* **2004**, *43*, 9989.

(10) Lipfert, J.; Doniach, S. *Annu. Rev. Biophys. Biomol. Struct.* **2007**, *36*, 307.

(11) Pollack, L. *Annu. Rev. Biophys.* **2011**, *40*, 225.

(12) Zhang, J.; Li, D.; Liu, G.; Glover, K. J.; Liu, T. *J. Am. Chem. Soc.* **2009**, *131*, 15152.

(13) Andresen, K.; Das, R.; Park, H. Y.; Smith, H.; Kwok, L. W.; Lamb, J. S.; Kirkland, E. J.; Herschlag, D.; Finkelstein, K. D.; Pollack, L. *Phys. Rev. Lett.* **2004**, *93*, 248103.

(14) Conway, B. E. *Ionic hydration in chemistry and biophysics*; Elsevier Scientific Pub. Co., 1981.

# Chapter 7: Conclusions

The solution behaviors of macroions are intriguing and complicated. Our studies have shown that instead of homogeneously distributing in solution, nanometer-sized POMs with moderate amount of charges tend to slowly self-assemble into spherical, hollow, vesicular "blackberry" type structures. Counterion mediated attraction and hydrogen bonds are identified as the major driving forces responsible for the unique structure formation. Kinetic studies show that the self-assembly of POMs into blackberries in solution is a free energy favorable process with a high activation energy barrier. The total scattered intensity recorded by SLS during the self-assembly shows a sigmoidal curve, indicating a two-step formation process which includes a slow nucleation step followed by a fast aggregation step. The slow nucleation step is critical to the molecular level self-recognition of two almost identical POMs $\{Mo_{72}Fe_{30}\}$ and $\{Mo_{72}Cr_{30}\}$ in water.

More interestingly, small POMs such as $\{U_{28}\}$ has shown different self-assembly behaviors than large POMs in solution. Besides the fact of an extended lag phase which is sensitive to counterion type, counterion concentration, and temperature, the $\{U_{28}\}$ macroions do not directly from blackberry structures but maybe through some intermediate states, as shown from the continuous increment of $R_h$. These unique behaviors may stem from the high surface charge density and the small size of the $\{U_{28}\}$, which would affect the activation energy barrier height and the stability of macroion-counterion ion pairing.

POM-based hybrid clusters demonstrate interesting self-assembly properties in solution due to their amphiphilic nature. Two of these hybrids were synthesized by connecting one or two organic pyrene tails with a Lindqvist type polyoxovanadate head cluster through trimester capping groups. These two hybrids form spherical vesicles in polar solvents. Four different counterions ($TBA^+$, $TEA^+$, $TMA^+$, and $H^+$) have been used to study the counterion effect on the vesicular structures and their consequent role in the fluorescent properties of the pyrene groups on vesicle surface. TBA counterions not only interact with POM polar head groups but also move into the hydrophobic regions and interrupt the close packing of pyrene groups. More importantly, when TBA counterions are replaced by protons, a dramatic change of the pyrene fluorescence pattern occurs, and the vesicle size, the fluorescence pattern, and the effective charge on the vesicles change correspondingly and reversibly with solution pH. The construction of pH sensitive vesicular structures could find applications in artificial cell studies, nanoreactors, as well as drug and gene delivery systems.

Furthermore, we have shown that the blackberry formation is a universal phenomenon for both macro-anions and macro-cations, through studies of nanocage typed macro-cations. Two different nanocages in different solvent conditions all confirmed the formation of blackberries and we estimated the inter-particle distance between adjacent nanocages in the blackberries is about $0.7 \pm 0.3$ nm, which is similar to the distance observed in blackberries formed by POMs. The vesicle size can be accurately adjusted by varying the solution polarity and/or counterion concentration. The counter-ion mediated interactions between nanocages are likely the major driving force for the assembly, while

hydrophobic interactions and/or π-π stacking interactions of the organic-ligand entities may also contribute to the supramolecular structure.

Our studies on POMs and nanocages not only show an interesting formation of blackberries but also could help people better understand the formation of viral capsids. SAXS studies on the counterion distribution around HBV capsids have shown that the $R_g$ of the capsids increases with the addition of counterions. More importantly, the increment is more obvious and quicker for divalent counterions compared to monovalent counterions. At relatively high salt concentrations, the increment approaches to a plateau, indicating the saturation of counterions around HBV capsids. These results imply that the HBV capsids are still highly charged in solution and have a strong effect on condensing small counterions. The formation of HBV capsids from the dimer proteins is sensitive to counterion type and concentration, even under high pH condition where the protein surface residues are highly charged. We believe under this condition, the counterion mediated attractions are enhanced and leads to the self-association of HBV dimers. This result supports our previous findings that counterion mediated attraction exists among macroions in solution and is critical to understand their solution behaviors.

In summary, macroions is a unique class of structurally well-defined polyelectrolytes whose solution behaviors are fascinating and attractive. They could serve as an excellent model to link simple ionic systems with colloidal systems and important knowledge of some fundamental questions (such as viral capsid formation) could be answered or better understood by illustrating their self-assembly process.

# Author Vita

## Dong Li

6 E Packer Ave, Bethlehem, PA, 18015
E-mail: dol207@lehigh.edu

**EDUCATION:**

**Lehigh University**, Bethlehem, PA, USA
Ph.D. candidate in Physical Chemistry Sep. 2012
**Advisor:** Prof. Tianbo Liu
Master of Science in Physical Chemistry Jan. 2009

**Shandong University**, Shandong, China
Bachelor of Science in Chemistry June 2006

**RESEARCH EXPERIENCE:**

**Research Assistant, Lehigh University** (Advisor: Prof. Tianbo Liu) *Fall 2007 – present*

- Investigated the self-assembly behavior of metal-organic nanocages in aqueous solutions by using Dynamic and Static Laser light scattering, NMR and TEM.
- Designed and investigated a "smart" supramolecular vesicular structure assembled from inorganic-organic hybrid clusters, which could be used as potential drug delivery systems.
- Synthesized and purified the Hepatitis B Virus (HBV) capsid protein and studied the self-assembly and disassembly mechanism of HBV capsids by using multiple techniques such as gel filtration, SAXS.
- Investigated the electrostatic interactions and pi-cation interactions of one inorganic-organic hybrid cluster by using DFT calculations (Spartan10' and Gaussian03').

## TEACHING EXPERIENCE:

**Teaching Assistant**, **Lehigh University** (Prof. Rebecca Miller) *2007, 2011*

- Physical chemistry lab,
- General chemistry lab.

## SKILLS:

***Technical Skills*:**

- Expert in Laser Light Scattering with extensive hands on experience of Small Angle X-ray Scattering (SAXS), Transmission Electron Microscopy (TEM), Scanning Electron Microscopy (SEM).
- Expert in performing chemical analysis such as Nuclear Magnetic Resonance (NMR) spectroscopy.
- Extensive hands on experience of cell growth, protein purification, gel filtration and ultracentrifugation.
- Proficient in IR, Raman and UV-vis spectroscopy; working knowledge of AFM, TGA, DSC *etc*

***Computer Skills*:**

- Proficient in simulation software suites such as Spartan10' and Gaussian03'.
- Master of general scientific computing packages such as OriginLab as well as Igor.

***Martial Arts:***

- AIKIDO (Orange belt)

## SCHOLARSHIPS AND HONORS:

- The Newton W. and Constance N. Busch Graduate School Fellowship, Lehigh University,
- Research Assistant. Department of Chemistry, Lehigh University,

## RESEARCH INTERESTS:

- **Supramolecular assembly** in solution and at interfaces (For instance, self-assembly of bio-macromolecules, dendrimers; viral capsids formation; super-lattice formation *etc*.),
- **Inorganic-organic hybrid materials** as multifunctional molecular devices,
- **Protocells**

## PUBLICATIONS:

- **Dong Li**, Panchao Yin, Tianbo Liu*, "Supramolecular Architectures Assembled from Amphiphilic Hybrid Polyoxometalates", *Dalton Trans*. **2012**, 41, 2853 - 2861.
- **Dong Li**, Jie Song, Panchao Yin, Silas Simotwo, Andrew J. Bassler, Yuyu Aung, James Roberts, Kenneth I. Hardcastle, Craig L. Hill* and Tianbo Liu*, "Inorganic-Organic Hybrid Vesicles with Counterion- and pH-Controlled Fluorescent Properties", *J. Am. Chem. Soc*. **2011**, 133, 14010 – 14016.
- **Dong Li**, Wu Zhou, Kai Landskron, Sota Sato, Christopher J. Kiely, Makoto Fujita* and Tianbo Liu*, "A Viral Capsid Type Vesicle Self-assembled from $M_{12}L_{24}$ Metal-Organic Hybrid Nanocages", *Angew Chem. Int. Ed.* **2011**, 50, 5182-5187.
- Tianbo Liu*, Melissa Langston, **Dong Li**, Joseph M. Pigga, Cel ńe Pichon, Ana Maria Todea, and Achim Müller*, "Self-recognition among Different Polyprotic Macroions During Assembly Process in Dilute Solutions", ***Science,* 2011**, 331, 1590-1592.
- **Dong Li**, Panchao Yin and Tianbo Liu*, "When Giants Meet Dwarves in the Same Pond – Unique Solution Physical Chemistry Opportunities Offered by Polyoxometalate Macroions." *Book Chapter in press*
- Panchao Yin, Pingfan Wu, **Dong Li**, Zicheng Xiao, Emily Bitterlich, Peng Cheng, Tianbo Liu,* and Yongge Wei*, "A Double-tailed, Fluorescently Active Surfactant with Hexavanadate as Giant Polar Head Group", *Angew. Chem. Int. Ed.* **2011**, 50, 2521 – 2525.
- Panchao Yin, **Dong Li**, and Tianbo Liu*, "Electrostatic Interactions between Metal-oxide Cluster Anions and Their Counterions", *Israel J. Chem*. **2011**, 51, 191 – 204.
- Jie Zhang, **Dong Li**, Guang Liu, Kerney Jebrell Glover and Tianbo Liu, "Lag Periods During the Self-Assembly of {Mo72Fe30} Macroions: Connection to the Virus Capsid Formation Process", J. Am. Chem. Soc., **2009**, 131 (42), pp 15152–15159
- Paritosh Mohanty, **Dong Li**, Tianbo Liu, Yingwei Fei and Kai Landskron*, "Synthesis of Stishovite Nanocrystals from Periodic Mesoporous Silica", J. Am. Chem. Soc. **2009**, 131, 2764 – 2765.
- **Dong Li**, Jie Zhang, Kai Landskron, and Tianbo Liu, "Spontaneous Self-Assembly of Metal-Organic Cationic Nanocages to Form Monodisperse Hollow Vesicles in Dilute Solutions", J. Am. Chem. Soc., **2008**, 130, 4226-4227
- **Dong Li**, and et.al, Multi-phase equilibrium microemulsions-based routes to synthesize nanoscale $BaWO_4$ spheres, cylinders and rods, Colloids and Surfaces A: Physicochemical and Engineering Aspects, 2006, 274, 18-23

## CONFERENCE PRESENTATIONS AND EXTENDED ABSTRACTS:

- Dong Li and *et al*. (2010) Novel Hierarchical Self-assembly of $M_{12}L_{24}$ Type Metal-organic Hybrid Macrocations in Polar Solvents. Poster presented at the *Colloidal, Macromolecular & Polyelectrolyte Solutions Gordon Research Conferences. California*.
- Dong Li and *et al*. (2010). Counterion effect on the self-assembly of functionalized polyoxometalate-surfactants. Poster presented at the *Pacifichem 2010 Conference at Honolulu, Hawaii*.

- Dong Li and *et al*. (2012) The effect of counterions in regulating the self-assembly of Hepatitis B viral capsids in solution. Poster presented at *MARM 2012, ACS Middle Atlantic Regional Meeting. Maryland*.
- Dong Li and *et al*. (2012) Unique self-assembly behaviors of macroions in dilute solutions. Oral presentation at the *244th ACS National Meeting. Philadelphia*.